

# POLITECNICO DI TORINO

Corso di Laurea Magistrale in Ingegneria Biomedica

Tesi di Laurea Magistrale

“Manufacturing of multifunctional nanocarriers  
and their influence on Osteosarcoma spheroids”



**Politecnico  
di Torino**

**Relatori**

Chiara Tonda Turo  
Piergiorgio Gentile  
Annachiara Scalzone

**Candidato**

Eugenia Crisafulli

Dicembre 2022



## Abstract

Osteosarcoma is one of the most common primary malignant bone tumor in children and adolescents, occurring commonly from the mesenchymal tissue in the distal femur. It is one of the most aggressive tumor, metastasizing mainly to the lung. Current treatment, that are surgery combined with neoadjuvant chemotherapy and radiotherapy, are often not satisfactory because surgery is not able to successfully control metastasis and chemotherapy leads to drug resistance and side effects, such as nephrotoxicity and cardiotoxicity. For these reasons it is imminently important to look for new treatment technologies. In this project, the use of nanoparticles for gene and drugs delivery was explored for applications in the treatment of osteosarcoma. The nanoparticles were composed of biodegradable and biocompatible polymers, chitosan and PLGA and were loaded with miRNA-34a - a short RNA structure that has a proven ability of act as tumor suppressor gene, inducing cell cycle arrest and apoptosis in OS cells. Considering the aspect that the co-delivery of multiple drugs maximized the effectiveness of treating OS, reducing systemic toxicity and drug resistance, three other classes of manufactured NPs were realized adding Doxorubicin and Resveratrol (as anti-OS drugs) to the previous CH-PLGA-miR34a core and exploring Layer-by-Layer technique, creating a bilayer-nanocoating, by means of pectin and chitosan polyelectrolyte. The pectin used in this work was successfully extracted from cocoa biowaste, via an effective pectin extraction process, helpful in overcoming food waste problem, in which cocoa industry is one of the key players. Manufactured NPs were tested on U2OS and SaoS-2 cells, analyzing cell viability, metabolic activity and morphology before and after the treatment with any of the manufactured NPs. Cells were treated in both two- and three-dimensional culture: 3D osteosarcoma spheroids were indeed realized, thus creating a cellular model that was as biomimetic and reliable as possible. Increased apoptotic activity and interference in cellular activity was mainly found by manufactured nanoparticles including the codelivery of miR-34a and drugs and functionalized by LbL nanocoating.

## Declaration

This report is submitted as part of the requirements for the Master Degree of Ingegneria Biomedica at the Politecnico di Torino and has not been submitted for any other degree at this or any other University. It is solely the work of Eugenia Crisafulli except where acknowledged in the text or the acknowledgements below. It describes work carried out at the University of Newcastle upon Tyne which is entirely recorded in a Project Logbook which has been made available for examination. I am aware of the penalties for plagiarism, fabrication and unacknowledged syndication and declare that this report is free of these.

A handwritten signature in black ink that reads "Eugenia Crisafulli". The signature is written in a cursive, flowing style with a large initial 'E'.

## Acknowledgements

I would like to thank my supervisor, Piergiorgio Gentile, for his support during the entirety of this project. His guidance in the laboratory and his resourceful and expert character were particularly valuable and I am very grateful for this.

# Content

Abstract .....	1
Declaration .....	2
Acknowledgements .....	2
1. Introduction.....	5
1.1 Bone Tissue.....	5
1.2 Osteosarcoma.....	6
1.3 Conventional treatments and their limits.....	7
2. Literature Research .....	8
2.1 Nanomedicine: nanocarrier as new advanced therapeutics technologies .....	8
2.2 Polymeric nanoparticles for Osteosarcoma treatment.....	9
2.3 miRNAs .....	11
2.3.1 miRNAs in cancer.....	11
2.3.2 miRNA-34s family in OS .....	12
2.4 Chitosan-PLGA-miRNA34a NPs.....	13
2.5 Combinatory therapy: Doxorubicin and Resveratrol .....	16
2.6 Layer-by-Layer coating technique .....	17
2.7 Polyelectrolyte materials.....	17
3. Aim and Objectives.....	19
3.1 Manufactured nanoparticles .....	19
3.1 Cell models .....	20
3.2 Sarcosphere.....	21
4. Materials and Methods .....	22
4.1 Materials.....	22
4.2 Pectin extraction.....	23
4.3 Pectin Characterization.....	25
4.4 Preparation of the nanoparticles.....	27
4.5 Layer-by-Layer Nanoparticles preparation .....	30
4.6 Characterization of Nanoparticles .....	31
4.7 miRNA 140 Evaluation of Entrapment Efficiency.....	32
4.8 Evaluation of miRNA-34a, Doxorubicin and Resveratrol Encapsulation .....	33
4.8.1 miRNA-34a Encapsulation .....	33
4.8.2 Doxorubicin and Resveratrol Encapsulation .....	34
4.8.3 Layer by layer NPs Encapsulation .....	34
4.9 Evaluation of miRNA-34a, Doxorubicin and Resveratrol Release .....	35
4.10 Statistical analysis .....	35

4.11 Cell Culture .....	36
4.12 Sarcospheres preparation .....	36
4.13 Sarcospheres characterization .....	37
4.13.1 Sarcospheres size over time .....	37
4.13.2 Scanning electron microscopy (SEM) analysis .....	37
4.14 Cellular Test.....	38
4.14.1 PrestoBlue assay.....	38
4.14.2 Live/Dead assay .....	39
4.14.3 Immunostaining assay .....	39
5. Results and discussions.....	40
5.1 Physico-chemical characterization of the extracted pectin .....	40
5.1.1 Extraction yield .....	40
5.1.2 Fourier-transform infrared spectroscopy - FTIR .....	41
5.1.3 Dynamic Light Scattering - DLS .....	42
5.1.4 Galacturonic acid measurement.....	43
5.1.5 Statistical results.....	45
5.2 Characterization of manufactured NPs.....	48
5.2.1 Characterisation and Morphology .....	48
5.2.2 Entrapment Efficiency of miR-140.....	57
5.2.3 Entrapment Efficiency of miR-34a, Doxorubicin and Resveratrol.....	59
5.2.4 Release of miR-34a, Doxorubicin and Resveratrol.....	62
5.3 NPs Statistical Results .....	65
5.3.1 Chitosan-PLGA miRNA34a NPs .....	65
5.3.2 ANOVA – The four manufactured NPs .....	66
5.4 Morphological characterization of in vitro manufactured Sarcospheres.....	73
5.5 Cell Tests.....	75
5.5.1 Cell-interacting drugs amount .....	75
5.5.2 Live and Dead essay.....	76
5.5.3 PrestoBlue essay.....	86
5.5.4 Immunostaining.....	89
6. Conclusions.....	93
7. Future insights .....	95
8. References .....	96
9. Appendix.....	101
9.1 Full Statistical Results.....	101
9.2 Supplementary images .....	106

# 1. Introduction

## 1.1 Bone Tissue

Bone is a type of hard connective tissue composed by an honeycomb-like inner matrix that gives to the bone its proper rigidity<sup>[1]</sup>. Bone tissue is made up of different types of bone cells: osteoblasts and osteocytes that are involved in the formation and mineralization of the tissues and osteoclasts that are responsible for the tissue resorption<sup>[2-6]</sup>. As shown in Figure 1, the mineralized tissue is distinguished in two types, based on the structure arrangement: compact (cortical) bone and spongy bone. In compact bone there is an organic component of collagen fibers (ossein) and an inorganic component of minerals, containing calcium, magnesium, and phosphate ions, which combined together make the mineral hydroxyapatite<sup>[7][8]</sup>. The mineralized phase combine with flexible collagen phase make the bone harder without being brittle, thus forming the lamellae, which are arranged concentrically to each other and are in turn organized into osteons, which are the structural units of compact bone. Collagen fibers are oriented in the same direction within each layer and in different directions between neighboring lamellae. Bones contains also other types of tissue, such as bone marrow, endosteum, periosteum, nerves, blood vessels and cartilage<sup>[1]</sup>.

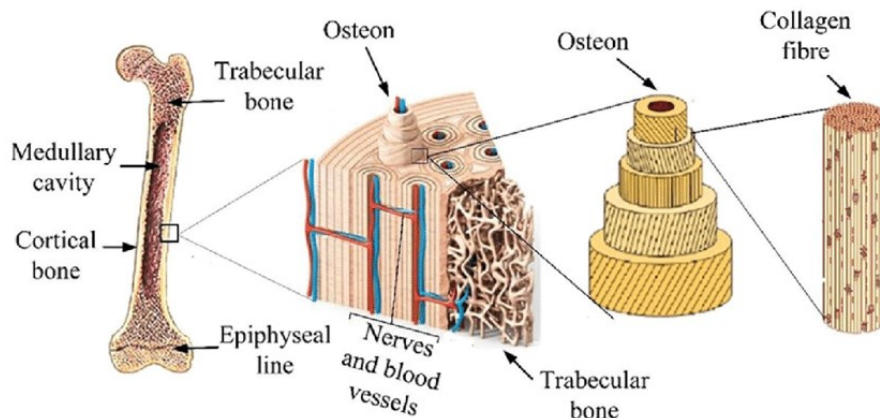


**Figure 1:** Bone anatomy from the macro to the micro bone structure. Image extracted from “Comprehensive Analysis of Orthopedic Drilling: A State-of-Art Review”

## 1.2 Osteosarcoma

Bone tumor is an alteration of the bone tissue and it is classified, based on histological findings, architecture and type of matrix produced, as benign or malignant. Even if benign tumors are noncancerous for the human body, they could become malignant if they are left untreated<sup>[9]</sup>. Benign bone tumors are osteoma, osteochondroma, osteoblastoma, fibrous dysplasia and enchondroma. On the other hand, among the different types of malignant bone tumor, osteosarcoma is the most common and important primary bone tumor (31.5%), followed by chondrosarcoma (25.8%), Ewing's sarcoma (16%), chondroma (8.4%), malignant fibrous histiocytoma (5.7%) and angiosarcoma (1.4%)<sup>[10]</sup>. Osteosarcoma is the most frequent primary malignant bone tumor affecting the youngest people in their first and second decades of life. Osteosarcoma has an annual incidence of 3.4 per million individuals worldwide<sup>[9]</sup> and the reason why it affects young people could be explained with the substantial association between hormonal changes during puberty and osteosarcoma pathogenesis during physiological bone growth. It is a type of tumor highly aggressive that generally metastasizes to the lung and it typically develops in the metaphyseal regions of the distal femur, proximal tibia, and proximal humerus. Although the cause of osteosarcoma is not fully known, mounting evidence suggests that CSCs and genetic abnormalities may play a crucial role<sup>[11]</sup>.

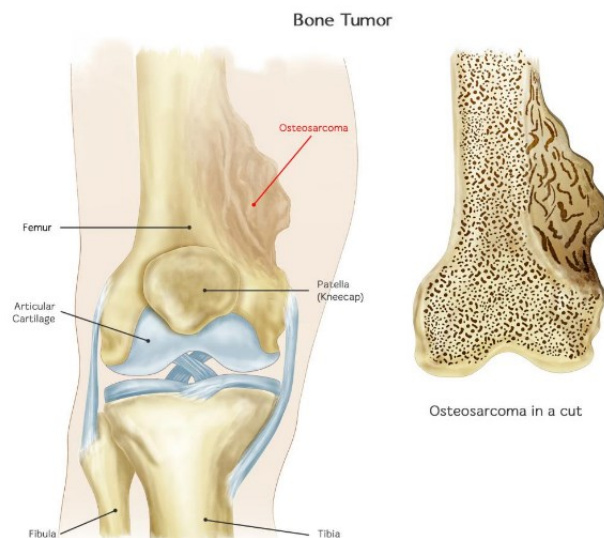


*Figure 2: Osteosarcoma bone femur tumor. Image from web source: [www.rehabmypatient.com/knee/bone-tumor](http://www.rehabmypatient.com/knee/bone-tumor).*

### 1.3 Conventional treatments and their limits

Cancer-related fatalities were predicted to account for 8.2 million deaths in 2012 that is about the 13% of all deaths.<sup>[13]</sup> During the last decades, the progress in diagnostic technology with the MRI (magnetic resonance imaging), PET (positron emission tomography), x-rays, CT (computed tomography) and the new experimental methodologies have enabled more effective treatments and diagnosis<sup>[9][10]</sup>. The current treatment is mainly surgery combined with neoadjuvant chemotherapy and radiotherapy and thanks to these, over the past decades, the five-year survival rate of OS patients has significantly improved to approximately 60–70%. However, the effectiveness of these traditional therapeutic approaches has plateaued, and chemotherapy could lead to drug resistance with potentially fatal adverse effects such as cardiotoxicity and nephrotoxicity.<sup>[11]</sup> One of the main causes of this tendency is that current medicines cannot be delivered selectively due to systemic toxicity.<sup>[6]</sup> Additionally, radiotherapy and surgery are the most effective treatments for local and non-metastatic tumors while tumor metastasis is difficult to control with surgery and some patients are still resistant to chemotherapy. Low selectivity, unfavorable side effects, and dose-limiting toxicity have now become significant obstacles in treating OS. Therefore, new novel treatment methods must be improved urgently to increase OS treatment effectiveness and prevent the negative effects of chemotherapy.<sup>[11]</sup>

## 2. Literature Research

### 2.1 Nanomedicine: nanocarrier as new advanced therapeutics technologies

Recent developments in nanomedicine could help to overcome the current drawbacks of Osteosarcoma treatments and drugs. One of the main aspect of the nanomedicine is the development of nanosized delivery systems<sup>[14]</sup> such as nanoparticles (NPs) that are solid colloidal particles with a nano-diameter<sup>[15]</sup>. Due to their exceptional biocompatibility and advantages in improved drug penetration and in vivo effective circulation time, nanoparticle drug delivery systems have attracted a lot of interest as tumor alternative treatment strategies. These nano systems are distinguished by high drug loading and governable drug release, they increase the bioavailability of the drugs by prolonging their release, allowing then lower frequency of administration and requiring lower dosages<sup>[18]</sup>. Because of their improved permeability and retention effect (EPR), their nanometric size allows their accumulation preferentially at the tumor sites, limiting the distribution of chemotherapeutic drugs in non-tumoral tissues and reducing systemic side effects<sup>[15]</sup>. Recently, nanoparticles (NPs) have been widely tested as drug delivery systems for a variety of malignancies, enabling increases in drugs efficacy and targeted administration (Pathak and Pathak, 2019). Metals like iron (Singh et al., 2018), silver (Chaloupka et al., 2010), or gold (Patra et al., 2010) have been used to make NPs, together with biodegradable polymers like lipid polymer base (Dehaini et al., 2016; Yalcin et al., 2020), and poly(D,L-lactide-co-glycolide) (PLGA); the latter enable a quick release of the drug carrier in cancer treatment<sup>[121]</sup>. Nanoparticles drug delivery systems can be principally classified into organic and inorganic carriers<sup>[14]</sup>. Liposomes, polymers, micelles, and dendrimers are the most common organic nanocarriers used to transport drugs to treat osteosarcoma while metallic nanoparticles, mesoporous silica nanomaterials, carbon-based nanomaterials and calcium phosphate carriers are the main types of inorganic nanocarriers. However, producing intelligent and versatile nanocarriers from a single nanomaterial is challenging, so that currently used drug delivery nanosystems are typically composed of several materials<sup>[16]</sup>.

## 2.2 Polymeric nanoparticles for Osteosarcoma treatment

One problematic feature in the manufacturing of NPs for genetic and drug delivery is the rate of biodegradation. Nanoparticles resistant to nuclease action will accumulate in the body and may reach problematic concentrations, however, on the other end, if not resistant enough, the particles could be destroyed before reaching the target site. Synthetic polymers like poly lactide-co-glycolic acid (PLGA) and PEG as well as natural polymers like hyaluronan and chitosan, that are frequently utilized, exhibit strong biocompatibility and biodegradability. Clinical trials have been conducted on a variety of biodegradable polymeric drug delivery systems that are intended for localized or systemic administration of therapeutic drugs for Osteosarcoma treatment<sup>[17][21]</sup>. Through ligands and proteins surface modification, polymeric nanoparticles can be directed to specific areas<sup>[22]</sup>. For both single and dual chemotherapeutic drug delivery, polymeric nanoparticles have been successfully used in numerous investigations<sup>[23-29]</sup>. In two separate therapeutically relevant animal models of osteosarcoma, DNA enzyme-loaded chitosan NPs showed encouraging outcomes, inhibiting the growth of the tumor while causing no damage to the surrounding bone<sup>[25]</sup>. In order to treat bone cancer metastases, Salerno et al.<sup>[27]</sup> created DOX-loaded bioconjugate NPs consisting of PLGA-alendronate (ALN). Studies conducted in vitro and in vivo revealed that bioconjugate NPs laden with DOX prevented osteolytic bone metastases better than free DOX<sup>[27]</sup>. Another successful study was about the delivery of docetaxel (DTX) and ALN simultaneously for the treatment of osteosarcoma, Liu et al.<sup>[30]</sup> created chitosan-decorated PLGA NPs. Dual drug-loaded NPs demonstrated prolonged release and better antitumor efficacy in osteosarcoma MG 63 cells, according to in vitro investigations<sup>[19]</sup>.

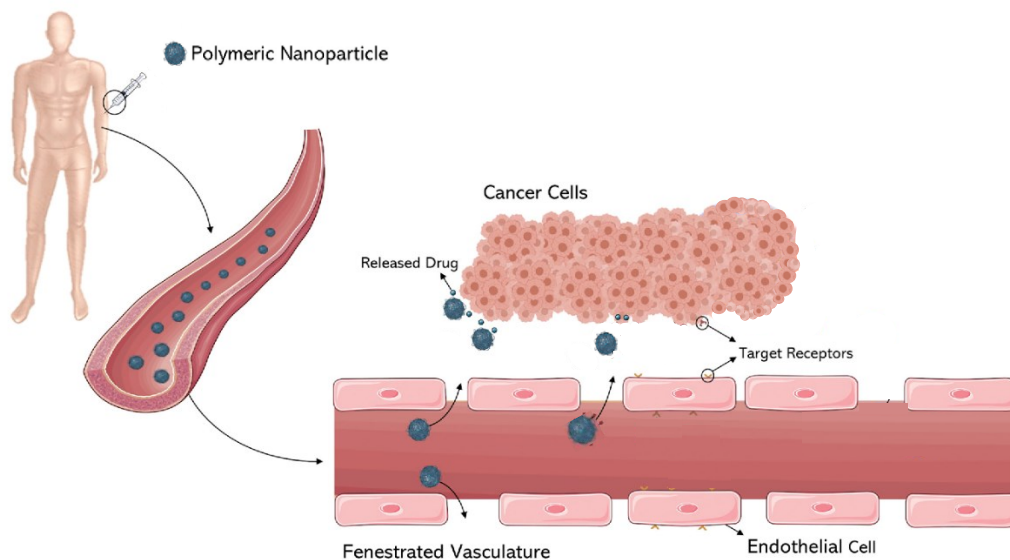


*Figure 3: Intravenous delivery and targeting of polymeric nanoparticles to cancer cells*

PLGA is considered one of the most important materials investigated for the use of nanoparticles. With its first development in 1981 with the aim of using it for drug delivery, there were indications of its potential for controlled, prolonged drug release and biocompatibility.<sup>[31]</sup> Using PLGA as a carrier is a way of reducing troubles of biodegradability, as it is fully degradable in an aqueous medium. By adjusting the ratio of glycolic acid to lactic acid in PLGA it is possible to vary the longevity of the polymer *in vivo*, with life cycles as long as 2 years<sup>[32][34]</sup>. Unfortunately, using PLGA as a drug delivery system in its native form, produces a NP with an overall negative charge, which leads to a low transfection efficiency<sup>[35]</sup>. It is preferable to use a combination of materials to produce an effective 'vehicle'. This is because it is possible to pair up different materials to have the positive attributes of both and suppress some of their features that may not be useful. This is performed in chitosan-PLGA nanospheres. PLGA is a polyanion so it can be coupled with chitosan (polycation) which resides on the surface of the carrier, giving a positive surface charge. Chitosan has a robust, semi-permeable and microstructurally well-organized structure. It has become an effective drug delivery system for chemotherapy drugs thanks to its low production and toxicity and to its exceptional properties of biocompatibility, slow-releasing potential, biodegradability and optime mechanical stability. Additionally, it possesses remarkable physiological characteristics to create films<sup>[36]</sup>. Chitosan has excellent potential as a gene delivery system on its own, displaying high transfection rates and excellent biocompatibility, also demonstrated by *F. Tekie et al.*<sup>[37]</sup> However, the formation of Chitosan nanospheres, combined with PLGA has also proved to be highly effective within oncology<sup>[33]</sup>.

## 2.3 miRNAs

### 2.3.1 miRNAs in cancer

MicroRNAs (miRNAs) are endogenous expressed small noncoding RNAs<sup>[54]</sup>, which are involved in post-transcriptional regulation of genes<sup>[55]</sup>, capable of inhibiting gene expression by targeting mRNAs, thus affecting biological development and behavior. These are essential for many biological processes, such as controlling cell differentiation, proliferation and apoptosis as well as embryogenesis and lineage determination<sup>[54]</sup>. Each miRNA has a specific target mRNA and changes in mRNA expression can directly affect the development of malignant tumors because the mRNA encoded by tumor suppressor or tumor-promoting genes can influence the synthesis of some crucial cancer-associated functional proteins<sup>[58]</sup>. Indeed, growing data suggests that miRNAs can act as tumor suppressors or oncogenes depending on the genes they target. Sayles et al.<sup>[58]</sup> discovered that the effects of a mutated miRNA site affected the function of specific miRNAs. The expression profiles of miRNAs are significantly altered in a wide range of human benign and malignant disorders and aberrant miRNA expression is strongly correlated with the diagnosis and progression of disease<sup>[59][60]</sup>. Multiple cancers, including Osteosarcoma, have been linked to dysregulation of miRNAs<sup>[61][62]</sup>, in fact numerous studies have demonstrated that OS patients have significant alterations in their miRNA expression profile and that miRNAs have a role in the occurrence, progression, and invasion of OS through a variety of mechanisms<sup>[63]</sup>. Multiple studies have then explored the value of miRNA for the treatment of OS patients<sup>[55]</sup> and these miRNA targeted treatment approach has shown enormous potential in controlling aggressive biological behavior of OS<sup>[64]</sup>. Besides the important of miRNA in regulating the OS growth microenvironment, many studies have shown that they can also be used to prepare nanoparticles for treating OS<sup>[55]</sup>.

### 2.3.2 miRNA-34s family in OS

MiRNA-34s play significant roles in the OS tumor suppressor signaling cascade that is activated by p53 in response to DNA damage or oncogenic stress in many malignancies<sup>[54]</sup>. Osteosarcoma is one among the several cancers for which the tumor suppressor gene TP53 is known to be involved<sup>[66]</sup>. In fact, in response to DNA damage and oncogene activation, TP53-encoded p53 significantly increases and it is subsequently phosphorylated, enabling it to separate from Murine double minute (MDM) 2; as a result, the cell cycle is arrested and apoptosis is induced, which leads to p53-mediated tumor prevention. More than 20% of OS patients have mutations in the TP53 gene, and research has demonstrated that these mutations play a role in both the development and progression of OS<sup>[11][67]</sup>. A rare TP53 mutation associated with Li-Fraumeni syndrome can also lead to OS<sup>[68]</sup>. According to Novello et al.<sup>[65]</sup>, the expression of miRNA-34 family is lower in OS tissues than it is in healthy skeletal tissues and miRNA-34s family have been discovered to be p53's downstream effectors. In fact miRNA-34a are induced by p53 in response to DNA damage and oncogenic stress in OS. The relationship between p53-induced miRNAs and OS has recently been the subject of some investigations. It was demonstrated that 117 primary OS samples had considerably lower levels of miR-34s expression and that miR-34a mimics transfected into MG-63 cells dramatically reduce cell growth and increase cell apoptosis through their targets such as mammalian target of rapamycin (mTOR), c-Met, and MDM4 (a TP53 gene inhibitory factor) in a p53-dependent manner<sup>[72][73]</sup>. Another study found that overexpression of miR-34a inhibits OS growth both in vivo and in vitro and this was attributed to the downregulation of Ether à go-go 1 (Eag1), a channel that is located in the central nervous system (CNS) and promotes cancerogenesis<sup>[74]</sup>.

#### miRNA-34a in Osteosarcoma

Several studies have shown downregulation of miR-34a in osteosarcoma and demonstrated that miRNA-34a acts as a OS tumor suppressor together with p53. It was discovered that ectopic expression of miR-34a induces cell cycle arrest in OS primary and lines cells and, moreover, several genes involved in cell cycle progression were downregulated by miR-34a, acting then as tumor suppressor. MiR-34a transactivation by p53 is also regulated by a positive feedback loop mediated by p53 target sites in the miR-34a promoter<sup>[69][70]</sup>. Loss of miR-34a expression in cancers is correlated with TP53 mutations, functional p53 suppression, and promoter hypermethylation. DNA damage-induced miR-34a expression in an OS cell line that expresses p53 was dependent on p53, and this resulted in the induction of cell-cycle arrest, encouragement of apoptosis, and DNA repair<sup>[71]</sup>. The P53 gene and the c-MET gene are directly impacted by miRNA-34a; c-MET is an important promoter to angiogenesis and tumorigenesis, so downregulating the c-MET gene, miRNA-34a prevents OS cells from proliferating and metastasizing. Therefore, the onset and progression of OS may be promoted by the reduction in miRNA-34a expression<sup>[81]</sup>.

#### 2.4 Chitosan-PLGA-miRNA34a NPs

MiR-34a promotes cell cycle arrest in primary tumor cells and cell lines when it is expressed ectopically. In line with this, a set of genes linked to the stimulation of cell cycle progression are downregulated by miR34. Collectively, these results suggested that the miR-34 family works in conjunction with p53 to limit tumor growth<sup>[75]</sup>. A study provides an insight on the nanostructures are assembled, the PLGA-chitosan encapsulating the miRNA. The nanoplexes are shown to be suitably stable for this application whilst loading and unloading genetic material at target sites was successful, with an undetectable amount of miR-34a present within the polyplex at the end of the study<sup>[76]</sup>. The article was able to offer insight into how the addition of miRNA influences the zeta potential and size due to the packing by electrostatic interaction. The encapsulation efficiency remained above 85% when  $\leq 300\mu\text{g}$  of miRNA was used. Once it was encapsulated, the sizes ranged from 150.7 to 178.0nm and the zeta potential from +25.1mV to +40.3mV for decreasing amounts of miRNA-34a. Additionally, when loaded, the polydispersity index (PDI) remained below a value of 0.2 demonstrating a small amount of mass distribution. The resulting particles were described as stable since neither great nor rapid increases in their diameters were found when incubated in synovial fluid for 24 hours. They were also found to be effective in penetration and intracellular delivery, with other articles using the same material reporting a more prolonged release over long periods, rather than burst, with increasing chitosan content.<sup>[77]</sup> An issue highlighted was that they became cytotoxic at high loading levels of miRNA-34a. However, empty nanoparticles of this composition do not reveal any cytotoxicity,<sup>[78]</sup> suggesting this was due to the contents; other articles focused on chitosan PLGA nanocarriers suggested cell viability increases with chitosan content when compared to just PLGA, further dismissing the idea that the particle is cytotoxic.<sup>[77]</sup>

The specifications that the project is hoping to meet are summarized in Table 1.

**Table 1:** Engineering specification for the manufacturing of chitosan PLGA nanoparticles.

Property	Value	Rationale	Ref.
Materials	Chitosan, PLGA	The materials used need to exhibit properties that allow the particle to be used effectively for gene and drug delivery. PLGA and chitosan are both biocompatible and biodegradable.	128
Size	100nm to 300nm diameter	Smaller particles generally lead to better penetration, but they must be large enough to be able to carry a substantial amount of miRNA. The size should not exceed 500nm as particles with values below this have been shown to escape the reticuloendothelial system which would otherwise lead to a big reduction in biological half-life, as well as a several times lower intracellular uptake. This is to be measured via DLS.	107, 130
Shape	Spherical	The particle to be manufactured is spherical in shape, therefore any difference in this may lead to a difference in the properties of the particle. It may affect the surface charge and penetrative ability. Being spherical has advantages such as having a good 'enhanced permeability and retention' value compared to other shapes. This is to be analyzed via a Transmission Electron Microscope (TEM).	131
Charge	>+25mV	Positively charged particles are more effective in penetrating the ECM due to it being negatively charged, therefore using electrostatic interaction to increase the depth. Additionally, larger charges are more desired as this increases stability due to the individual particles having a larger repulsive force between themselves, decreasing the chance of aggregation. Cationic nanoparticles also experience the proton sponge effect which can help decrease the chance of digestion/clearance by endosomes. This is to be measured via DLS.	132
Release time	24 hours with minimal burst	The nanoparticle must be stable enough to not experience an immediate burst release so that the contents can reach deep into the bone tumor. It should not have a burst release in the first 24 hours and if it does, preferably not all the	131

		contents should be released, so a sustained release is still possible. This will help ensure particle has the best chance of interacting with the target cells. If the particle gets trapped in the articular surface, a prolonged release means the cargo still has a chance of penetrating deeper into the Osteosarcoma.	
Manufacturing	Must be reproducible	A reproducible manufacturing method allows for the nanoparticle to be produced at the same standard, with the possibility to be scaled. It would mean that its properties would not fluctuate from batch to batch.	133
Polydispersity	Polydispersity index $\leq 0.2$	The size distribution of the nanoparticles when manufactured should be within a range so that the properties do not vary. A value of 0.2 for the PDI has been stated to be an acceptable level. This is to be measured via DLS.	134
Encapsulation	Efficiency $\geq 70\%$	The encapsulation efficiency should remain high as this could otherwise lead to drug wastage (in this case miRNA) which is a major flaw in some gene delivery systems, potentially affecting manufacturing factors such as cost and time to ensure the particles are loaded with sufficient cargo. In most sources the efficiency is extremely high, therefore a value of 70% is reasonable.	135

## 2.5 Combinatory therapy: Doxorubicin and Resveratrol

The co-delivery of drugs leads to significantly better results than a single-drug delivery. The most popular combination therapeutic modality for successful cancer treatment in clinical practice is the co-delivery of multiple chemotherapeutic drugs<sup>[38]</sup>, with the purpose of maximizing the effectiveness of treating cancer while reducing systemic toxicity and drug resistance<sup>[39][40]</sup>. Therefore, the treatment must act synergistically on various carcinogenic signal transduction pathways, targeting oncogenic pathways.

Doxorubicin Hydrochloride (DOXO) is an anthracycline antibiotic that stimulate cell apoptosis, thus it is used as a drug to treat different cancers such as endothelium cells, leukemia and lymphoma<sup>[41][42]</sup>. In solid tumors, depending on the concentrations used, it can potentially induce senescence<sup>[43]</sup>. DOXO is provided intravenously in the course of OS treatment together with other chemotherapeutic medications like methotrexate (MAP) and cisplatinum<sup>[44]</sup>. Studies conducted in vitro to determine the impact of DOXO on human OS cell lines revealed that endocytosis, which occurs 24 hours after DOXO treatment, reduces cellular metabolic activity and development of U2OS<sup>[45]</sup>. However, when exposed to high amount of DOXO, U2OS cells can develop resistance to it<sup>[46]</sup>. The use of NPs has shown promise in attempts to get around the drawbacks of free intravenous DOXO in the treatment of cancers like breast cancer<sup>[47]</sup> and hepatic cancers<sup>[48]</sup>, suggesting DOXO loaded NPs could be a practical way of promoting leftover osteosarcoma cell apoptosis.

Trans-3, 4', 5 trihydroxystilbene, known as resveratrol, is a naturally occurring tiny polyphenolic molecule that is extracted from a variety of plant species, including grapes, mulberries, and peanuts. Over the past ten years, extensive research has been conducted on it and it was discovered that Leukemia<sup>[49]</sup>, prostate cancer<sup>[50]</sup>, and stomach cancer<sup>[51]</sup> are just a few of the cancers that resveratrol has been shown to help prevent from progressing. Resveratrol was found to be a power antioxidant but, in recent years, resveratrol has been also suggested as a possible anti-cancer agent<sup>[52]</sup>. The effects of resveratrol on osteosarcoma cells were explored and it was discovered to be an efficient inhibitor for osteosarcoma stem cells in vitro and in vivo, that gives the basis its clinical application in osteosarcoma ad a promising agent for OS treatment<sup>[53]</sup>.

## 2.6 Layer-by-Layer coating technique

Layer-by-Layer (LbL) polymeric based nanoparticles are promising new systems for use as drug delivery vehicles. The layer-by-layer technique is one functionalization techniques that allow to achieve performance properties of our system. It is a multi-material nanofabrication technique for surface coatings whose advantages are definitely the greater controlled release of drugs, as well as the slower biodegradability so that the drug delivery system can reach the target without having been completely biodegraded. It also enables to encapsulate drugs within the coating so as to deliver to the target site greater therapeutic effect. Layer-by-layer (LbL) assembly refers to the method of depositing alternately charged materials, followed by washing, in order to removes excess non-absorbed polyelectrolyte, and filtering between each deposit<sup>[87]</sup>. Using this assembly method, a variety of shapes, sizes, and compositions of building materials may be created with precisely tuned and controlled physicochemical properties<sup>[88]</sup>.

## 2.7 Polyelectrolyte materials

### Pectin

Pectin is a natural polysaccharide and it consists of methyl esterified D-galacturonic acid<sup>[79]</sup>. Residing in the cell walls of plants, pectin has various potential biomedical applications because of its antimicrobial, antioxidant and anti-inflammatory effects, as well as its biocompatibility<sup>[80]</sup>. It's also widely used in the food industry due to its ability to increase viscosity and bind water. Industrial pectin is generally high methyl pectin, which can easily form gels in the presence of other sugars, acids, or certain metal ions. The degree of esterification (DE) of pectin is the primary factor affecting the mechanical properties, including the solubility of the pectin and its gelling and film-forming properties<sup>[79]</sup>. In high methyl pectin, the DE is higher than 50%. Low methyl pectin can more easily form a gel in the presence of a divalent ion such as calcium ( $\text{Ca}^{2+}$ ) and does not need sugar or acid to gel, whereas high methyl pectin does<sup>[79]</sup>. Gel formation in pectin is caused by hydrogen bonds between hydroxyl groups around molecules and between carboxyl groups on molecules<sup>[81]</sup>. One advantage of employing pectin as a drug carrier is its capacity to boost bioavailability, which enables a reduction in dosage and application frequency for a chosen treatment. This is due to the fact that it can enhance the mucosal membrane's bio adhesive function, extending release and boosting bioavailability<sup>[82][83]</sup>. Reduced dosage and application frequency will also result in a decrease in the amount of drug that needs to be produced, conserving resources.

### Biowaste resource

It was chosen to use a non-commercial pectin and particularly to extract it from cocoa biowaste. Food waste is indeed one of the biggest problems worldwide since there are food processing factories everywhere, which cause a lot of inedible and unwanted parts of the plants to end up in landfills. Most are rich in organic material and functional compounds, like pectins and polyphenols. The result is severe environmental impact, including uncontrolled emission of greenhouse gases, foul odours, and the proliferation of pests around the waste<sup>[84]</sup>. The food waste can be turned into marketable products and help countries financially. Additionally, it would boost income by creating jobs and might improve food security in poorer countries<sup>[83]</sup>. As one of the world's largest food industries, cocoa bean processing produces a large amount of waste. Biowaste is generated at each processing step and the resulting biomass is cheap, renewable, and abundant. This makes it ideal for use in many industries, including food and pharmaceutical<sup>[85]</sup>. A cocoa by-product produced in the field processing chain is cocoa pod husks, which contain high levels of useful compounds, such as pectins and polyphenols.

### Process extraction

Pectin has been extracted through several methods from various sources over the years. Methods of conventional pectin extraction include using mineral or organic acids at relatively high temperatures (80-120°C)<sup>[86]</sup>. Non-traditional techniques include Ultrasound, microwave, and enzyme assisted extraction. During ultrasound-assisted extraction, mechanical vibrations are applied to solids, liquids, or gases, combined with an extraction solvent, at frequencies greater than 20kHz, to isolate targeted compounds. The mixtures of solvent and extraction materials are placed in a water bath to ensure uniform heating. Although ultrasound-assisted extraction uses less energy than conventional methods, an increase in temperature (still lower than conventional techniques) will enhance the extraction process. Extractions of useful compounds, drying, emulsification and homogenization of food products can all be achieved using this method<sup>[86]</sup>. In comparison with conventional heating acid methods, ultrasound-assisted extraction has many advantages. First of all the extraction of pectin is more efficient, in both cost and time. It possesses lower energy consumption, shorter treatment time, lower solvent usage, increased safety, and an increase in yield<sup>[86]</sup>. In addition to causing molecules to move more rapidly, cavitation bubbles near the cell walls collapse, allowing the solvent to penetrate the cells more deeply and effectively, reducing then the required concentration of the solvent. All these properties result in a more environmentally friendly and sustainable process<sup>[84]</sup>. In addition to the properties listed above, we will see later in the extraction that another important advantage is to possess an highly negative charge. This is very important for our work because the pectin will be the first coating layer of the nanoparticle and, in order to interact electrostatically with the positive core and the second positive layer, it must precisely possess a powerful negative charge.

### 3. Aim and Objectives

#### 3.1 Manufactured nanoparticles

Among the types of nanoparticles used in the field of research against osteosarcoma, polymeric nanoparticles were chosen for this work for their excellent mechanical properties, versatility of preparation and outstanding biodegradability. The chosen biomaterials were PLGA and Chitosan, which made the core structure of the nanoparticles, combining together their positive features such as biodegradability and mechanical structure and avoiding the negative aspect such as the negative nature of the PLGA. Beyond the most suitable materials, however, we wanted to investigate those drugs effective in the treatment of osteosarcoma and those emerging advanced techniques that promise great future and perspective for the treatment of osteosarcoma. Among these, miRNAs were analyzed in order to understand their mechanism and behavior toward Osteosarcoma cells. For this reason, combined together with PLGA and Chitosan, miRNA, in particular miRNA-34a, was chosen as the third main component for the formation of the nanoparticulate complexes. Starting from the optimization of the nanoparticles consisting in Chitosan, PLGA, Pluronic and miRNA, four types of nanoparticles were manufactured, adding drugs and exploring Layer-by-Layer technique to do a superficial nanocoating, in order to obtain a more stable nanoparticle and encapsulate higher amount of drugs. First of all, process parameters were optimized using miRNA-140, which was different from miRNA-34a that is the subject of our study but it was useful in order to optimize the procedure without wasting miRNA-34a. Once the protocol was optimized with miRNA-140, the fabrication of the nanoparticles was repeated with miRNA-34a, making minor changes because miRNA-34a turned out being slightly more negative than miRNA-140. Analyzing the results obtained from nanoparticles with miRNA-34a, it was decided to make the system more complex and effective by adding anti-cancer drugs as Doxorubicin and Resveratrol to the miRNA-34a core. Finally, it was decided to add a further optimization by making a bilayer nanocoating of the surface of the nanoparticles, obtaining them by the interaction of two polyelectrolyte solutions of opposite charge: first layer of pectin (negative charge) and second layer of chitosan (positive charge). In the forming layers it was also inserted additional amounts of the two drugs previously interjected in the core. For the needs previously discussed, the pectin used in this work was extracted from Cocoa biowaste before starting with the manufacturing NPs process. Figure 4 shows a schematical representation of the different types of manufactured nanoparticles and, for simplicity, how they have been named during the entire work. The manufactured NPs were tested on U2OS and SaoS-2 cells on both bidimensional culture and on vitro Osteosarcoma spheroids, created in order to have a more mimetic tumoral tissue. Cell viability, metabolic activity and morphology were analyzed before and after the treatment with any of the manufactured NPs.

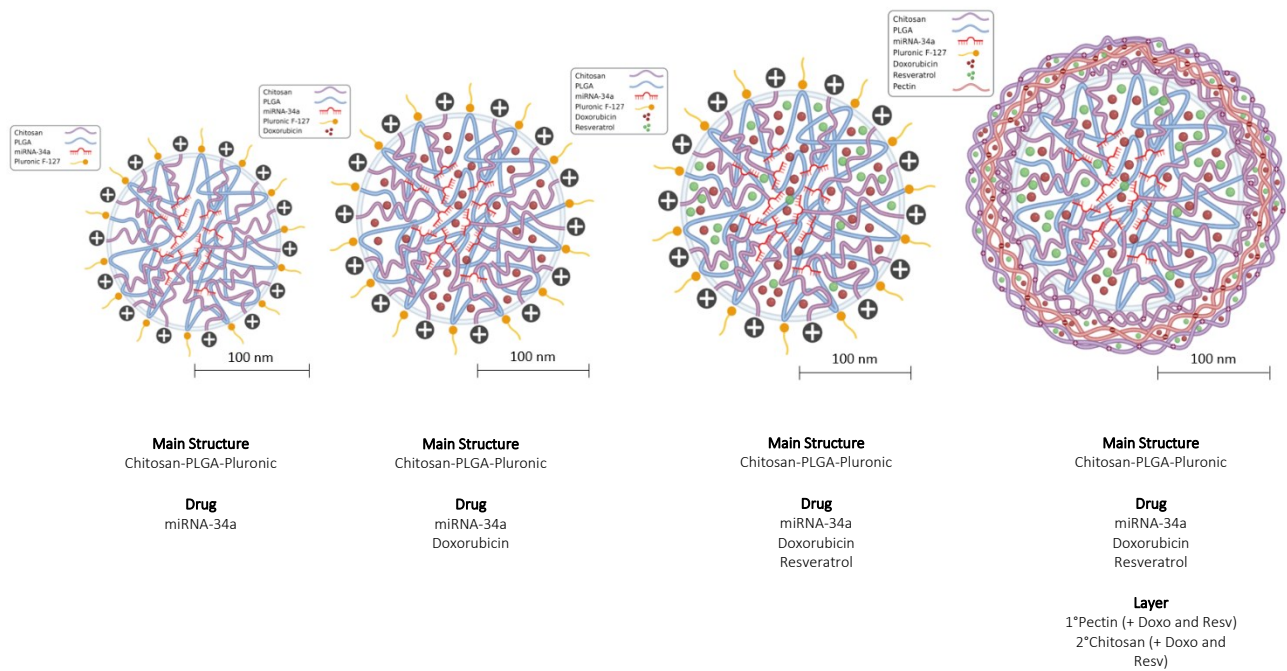


**Figure 4:** The four types of manufactured nanoparticles, starting from the left with the basic one of Chitosan-PLGA-Pluronic-miRNA34a, then adding Doxorubicin and Doxorubicin/Resveratrol in combination and finally the model with the two layer with the two drugs in them and drugs plus miRNA inside the core. Created using BioRender.

### 3.1 Cell models

It was chosen to test the manufactured nanoparticles on two-dimensional models with different cell densities and on 3D spheroid models, called during the work "Sarcospheres". The osteosarcoma cells used for both models were SaoS-2 and U2OS cell lines, which have been chosen and tested in so many works and researches, both in two-dimensional culture and for the formation of osteosarcoma spheroids<sup>[89][90][91]</sup>.

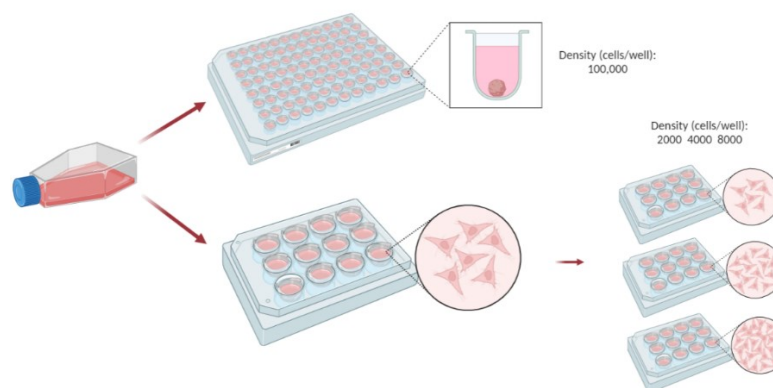


**Figure 5:** two- and three-dimensional cell culture for NPs treatments, created using BioRender.

### 3.2 Sarcosphere

Several studies demonstrated that the use of 2D techniques to investigate cancer cells and tumor processes<sup>[92]</sup> failed to explain tumor biology because they did not mimic properly the tumor macrostructure and did not represent the huge complexity and heterogeneity of the tumor microenvironment<sup>[93-95]</sup>. These 2D models showed very well the growing of the tumor cells but they failed in providing information about the 3D network between the tumor cells and the interaction between cells and extracellular matrix, as well as superficial and environmental conditions<sup>[92][93]</sup>. Different studies demonstrated instead that the 3D culture system were able to mimic tumor tissue characteristic<sup>[97]</sup>, growing up with the concept of “tumor engineering” as a “complex culture model that mimics in vivo tumor microenvironment in order to study the dynamics of tumor development and progression, and to develop clinically relevant models to target cancer and cancer stem cells”<sup>[98][99]</sup>. The potential of spheroids in cancer pharmacology was shown in several studies, highlighting the contribution to eliminate, at the preclinical state, the non-effective drug candidates and helping in identifying those promising drugs non-successful in 2D model<sup>[100][101]</sup>. The several techniques used to create spheroids are mainly divided into scaffold free and scaffold method. We were interested in the scaffold free ones, in which spheroids generate through a spontaneous aggregation process<sup>[102]</sup>, facilitated by liquid overlay<sup>[103][104]</sup> or hanging drop techniques<sup>[105][106]</sup>. In particular we relied on the liquid overlay technique using commercially low binding plates<sup>[94]</sup>. Osteosarcoma spheroids were there realized for both types of cells and they were named “Sarcosphere” during the entire work.

## 4. Materials and Methods

### 4.1 Materials

For pectin extraction, Cocoa pod husks (kindly supplied from Universidad Surcolombiana, Colombia) were grounded into a fine powder to increase the surface area of the material and therefore the efficiency of the reactions, Sodium Hydroxide (pellets, reagent grade,  $\geq 98\%$ , Sigma Aldrich) Distilled water (Milli-Q® water system), Ethanol (99.8%, Sigma Aldrich) were used. For NPs preparation Poly(D,L-lactide-co-glycolide) (lactide:glycolide (75:25), mol wt 66,000-107,000), chitosan (low molecular weight of 50,000-190,000 Da based on viscosity), Pluronic F-127 (powder, BioReagent, suitable for cell culture), acetic acid (glacial, *ReagentPlus*®,  $\geq 99\%$ ), acetone (ACS reagent,  $\geq 99.5\%$ ) were purchased from Sigma Aldrich. MiRNA-140 (MIRacle™ hsa-miR-140-5p miRNA Agomir/Antagomir) was purchased from AcceGen Biotechnology, MiRNA-34a (miRIDIAN microRNA Human has-miR-34a-5p) was purchased from Dharmacon Group company, RNase-free water was purchased from ThermoFisher. Doxorubicin hydrochloride (98.0-102.0% HPLC, powder), Resveratrol (powder,  $\geq 99\%$  HPLC), Dimethyl sulfoxide (DMSO) (ACS reagent,  $\geq 99.9\%$ ) were purchased from Sigma Aldrich, Sodium acetate buffer pH5, pectin extracted from cocoa biowaste, dH<sub>2</sub>O buffer pH5 were used in this thesis project. Aliquot of miRNAs: having 50nmol miRNAs (705.2micrograms) and wanting to make aliquots of 20  $\mu$ M, It was added 2.5ml sterile PBS to the total and then divided into 5 Eppendorf tube (1.0ml) with 500 $\mu$ l of the miRNA solution in each. For cell culture tests, Fetal Bovine Serum (FBS, ThermoFisher, Gibco CAS No. 10500056), penicillin/streptomycin (P/S, Sigma-Aldrich, P0781100 mL), Human Fibroblast Growth Factor (hFGF-2, Sigma-Aldrich, 106096-939), L-Glutamine (LG, 5 mM, Sigma-Aldrich, TMS-002), Phosphate Buffered Saline (PBS Sigma-Aldrich, MFCD00131855), Trypsin/EDTA (Sigma-Aldrich, MFCD00130286), Dulbecco's Modified Eagles Medium (DMEM, Sigma-Aldrich, Gibco high glucose 4500 mg/L, 11995-065) were used.

## 4.2 Pectin extraction

The extraction of the pectin from cocoa biowaste was performed using ultrasound-assisted extraction (UAE) method, shown in Figure 6. Briefly, 0.05 molar NaOH solution (pH=12) was prepared by dissolving 0.4g of NaOH pellets in 20ml of distilled water in a beaker at room temperature under stirring until dissolved. The biowaste powder was measured using the values of the ratios in Table 2 and it was suspended in 150ml of the prepared 0.05 M NaOH, adding them to the corresponding labelled bottles. Minitab was used for the design of experiments through box-Behnken design, generating 20 combinations of variables to use. However, five of these (Temp: 60 degrees C, Ultrasonic bath time: 67.5 mins, Ratio: 1:40) were the central points. Following the DoE, different solutions were placed in the ultrasonic bath (VWR ultrasonic cleaner) for their respective temperature and time shown in Table 2. Once the time of the ultrasonic bath ran out, the bottles were then removed, and the mixtures were poured into centrifuge tubes and centrifuged at 4400rpm for 20 minutes (Thermo Scientific™ Megafuge 16R TX-200 Centrifuge was used) to separate the mixture into solid and liquid phases. These were then filtered using a Buchner funnel to remove as much liquid from the remaining biowaste as possible. The resulting supernatant solution was then measured and mixed with 99.8% ethanol in a 1:1 ratio (ml) in order to produce pectin gel and then refrigerated at 4 °C to allow the precipitation of pectin. After 24h, the solution was poured into centrifuge tubes, all equal amounts, and centrifuged at 4000 rpm for 15 minutes to separate the polymers and ethanol. The ethanol was then removed from the tubes and disposed of, isolating the mixture of the various polymers. These polymers were then separated into different flat-bottomed tubes and placed in an incubator at 37°C for 24 hours to evaporate the ethanol. Then, the pectin was placed on a greaseproof paper as a layer and dried into the oven (Thermo Scientific™ Vacuotherm Jacket-Heating VT 6025 was used) at 70°C for 48h to obtain a thin dried layer of pectin.

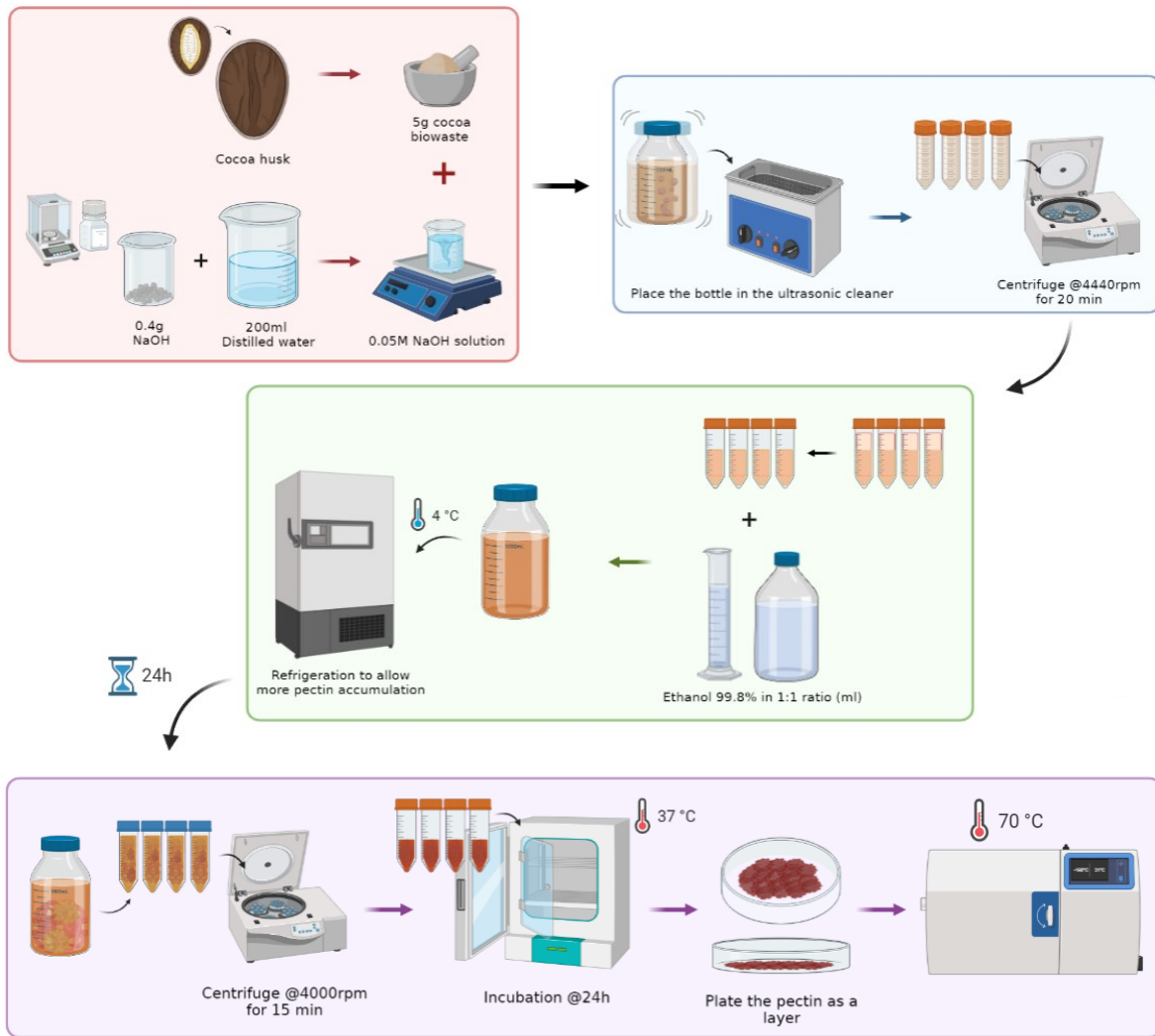


Figure 6: Protocol for 0.05M NaOH Pectin extraction, created using BioRender.

**Table 2:** The Design of Experiment (DoE) for Pectin extraction.

Run No.	Temperature (°C)	Time (min)	Ratio (1:x)	Weight to measure (g)
1	70.00	45.0	30.00	5.00
2	50.00	90.0	50.00	3.00
3	60.00	67.5	40.00	3.75
4	70.00	90.0	30.00	5.00
5	60.00	67.5	40.00	3.75
6	50.00	45.0	30.00	5.00
7	70.00	45.0	50.00	3.00
8	70.00	90.0	50.00	3.00
9	60.00	67.5	40.00	3.75
10	50.00	90.0	30.00	5.00
11	50.00	45.0	50.00	3.00
12	60.00	67.5	40.00	3.75
13	60.00	67.5	23.67	6.34
14	60.00	67.5	40.00	3.75
15	43.67	67.5	40.00	3.75
16	60.00	67.5	40.00	3.75
17	60.00	104.2	40.00	3.75
18	60.00	67.5	56.33	2.66
19	60.00	30.7	40.00	3.75
20	76.33	67.5	40.00	3.75

### 4.3 Pectin Characterization

The molecular composition and structure of the extracted pectin were analyzed through Fourier Transform Infrared (FTIR) analysis, measuring the range of wavelengths in the infrared region absorbed by samples, using this non-destructive analytical technique. Samples were exposed to Infrared radiation and their ability to absorb various wavelengths, according to their bonds, was measured. These measures were obtained with a Spectrum Two™ FT-IR instrument equipped with a horizontal attenuated total reflectance (ATR) crystal (ZnSe) (PerkinElmer Inc., USA). Data were collected in Absorbance mode, with wavenumber values from 4000cm<sup>-1</sup> to 550cm<sup>-1</sup> and each spectrum was the result of the average of 16 scans with 4cm<sup>-1</sup> resolution. After each scan a baseline correction was performed. The zeta potential of the extracted pectin was measured via dynamic light scattering method. The values were obtained with a Zetasizer Nano ZS Instrument (Malvern Panalytical Ltd) and expressed as the mean ± standard deviation. These values were found by looking at the Brownian motion (random movement) of the pectin and linking this to its characteristics. The cuvettes feature two gold electrodes which are involved in measuring the zeta potential: a charge was applied between

the two electrodes and the pectin move towards the oppositely charged one. A laser beam was used to measure the intensity of scattered light as the particles move through the medium, returning a frequency equivalent to their velocity, leading to the voltage being found - this was done at multiple voltages to calculate the zeta potential.<sup>[110]</sup> For the DLS analysis, the samples were then diluted in dH<sub>2</sub>O to reach a concentration of 0.1% w/v. The final value was calculated as average of three measurements, each obtained after a maximum of 100 runs. Six measurements were taken for each of the 20 samples and then averaged, obtaining the final 20 mean values. The production yield of the pectin, that is how much pectin was extracted from the powder of the cocoa biowaste used, was measured by subtracting the mass of biowaste measured at the beginning and the mass of dried pectin measured at the end of the process. Briefly, after the evaporation of the ethanol in the 24h incubation process, the polymers were placed on greaseproof paper (which was weighed and noted) and then they were placed in an oven at 70°C for several hours until dried. Once dried, they were weighed, and the values were used to calculate the yield as:

$$Yield (\%) = \frac{A}{B} * 100 \quad (\text{Eq.1})$$

A is the weight of the extracted dried pectin while B is the weight of the original cocoa powder measured at the beginning of the experiment. The methoxyl (MeO) and anhydrouronic acid (AUA) contents and degree of esterification (DE) in optimized extracted pectin samples were analyzed by conventional methods<sup>[116]</sup>. To 50 mg of pectin, 500 µL of ethanol, 10 mL of distilled water, 0.10 g NaCl and one drop of phenol red indicator were added. The solution was stirred for 15 min to dissolve all of the components, and then titrated with 0.1 M NaOH until the colour changed (Titration A). Subsequently, 2.5 mL of 0.25 M NaOH was added to the mixture and allowed to stand for 30 mins at room temperature. Finally, 2.5 mL of 0.25 M HCl was added and the mixture was titrated again with 0.1 M NaOH until the colour turned red (Titration B). The methoxyl content was calculated by using the following equation (Eq.2):

$$MeO(\%) = \frac{(\text{meq Titration B} * 31 * 100)}{\text{weight of sample (mg)}} \quad (\text{Eq.2})$$

Where meq Titration B are the milliequivalents of NaOH used for the Titration B, and 31 is the molecular weight of the methoxyl group.

The anhydrouronic acid content was calculated according to the equation 3 (Eq.3):

$$AUA(\%) = \frac{176}{z} * 100 \quad (\text{Eq.3})$$

Where 176 is the molecular weight of AUA and

$$Z = \frac{\text{weight of sample (mg)}}{\text{meq Titration A} + \text{meq Titration B}} \quad (\text{Eq.4})$$

Finally, the degree of esterification of the extracted pectin was calculated by:

$$DE(\%) = \frac{176 * MeO\% * 100}{31 * AUA\%} \quad (\text{Eq.5})$$

A colorimetric method based on the m-hydroxydiphenyl reagent was used to measure the total galacturonic acid (GA) content of the extracted pectin following the protocol proposed by Guo et al.<sup>[152]</sup> Briefly, 500  $\mu\text{L}$  of pectin solution (concentration of 200  $\mu\text{g}/\text{mL}$ ) was poured into a glass tube vial, and then 3 mL of sulfuric acid/sodium tetraborate was added and immediately cooled in a bath containing cold water. A continuous operation including shaking the tubes for 30 s with a vortex mixer (VORTEX 3, IKA, Germany), heating in a water bath (GLS Aqua 12 Plus, Grant, UK) at 100 °C for 5 mins and cooling in ice water was performed. Then, 100  $\mu\text{L}$  of m-hydroxydiphenyl (0.15% in 0.5% NaOH) were added to the vial and kept under shaking for 5 minutes (SSM1, Stuart, UK). Finally, the absorbance of the resulting solutions was read at 525 nm using a multiplate reader (FLUOstar Omega, BMG Labtech, Germany). For the preparation of the calibration curve, solutions of galacturonic acid (between 1-200mg·mL<sup>-1</sup>) were used.

#### 4.4 Preparation of the nanoparticles

Nanoparticles with miRNA-140 core were prepared using a nano-complexation method taken from the source using the same materials<sup>[107]</sup> as follows: 60mg of PLGA was added to 20ml of acetone in a beaker at room temperature, under magnetic stirring (IKA<sup>TM</sup>C-MAG MS 7 Magnetic Stirrer was used) inside a fume cupboard to speed up the process of the PLGA dissolution ( $\approx$  30 minutes). In a separate beaker, 3mg of chitosan was added to 50ml of acetic acid (0.5% v/v) and 0.5g of Pluronic F-127 (1%w/v). This second solution was then filtered using a 0.22  $\mu\text{m}$  polyamide filter to remove any chitosan aggregates. 50 $\mu\text{l}$  of miRNA-140 was then added, before being homogenized at various speeds and times to reduce the size of the particles in this solution. The Design of Experiment (DoE) was formulated by Minitab software, shown in Table 3, that enabled to evaluate the relationship between both the speed and time on the size and zeta potential of the nanoparticles. In this instance, it was a central composite design with the centre points, being included a total of 5 times, at 24,000rpm and 75 seconds. The other points consist of cube points, the 4 values in and around the working range, and axial points, the final 4 values and more extreme points, often described as being outside the cube. The two prepared solutions were then combined, with 200 $\mu\text{l}$  of the solution containing PLGA being added to 500 $\mu\text{l}$  of the second

solution, and mechanically stirred at 600rpm for 3 hours to allow for the solvent to evaporate.<sup>[108]</sup> Finally, the samples were centrifuged at 13,000rpm (Thermo Scientific™ Pico™ 17 Microcentrifuge was used) for 1 hour to separate the nanoparticles and the remaining liquid. The same procedure was performed to make the nanoparticles with miR-34a (Figure 8), with some exceptions. In fact, analyzing the zeta potential of both miRNAs through DLS, a greater negativity was found for miRNA-34a, therefore it was decided to use a 0.06% chitosan solution (instead of the previous 0.006%) and using 600µl of the latter, in combination with the 50µl of miRNA-34a, instead of 450µl. The Design of Experiment (DoE) was formulated by Minitab and it is shown in Table 4. Once the preparation of the nanoparticles with miR-34a core was optimized, it was decided to include anti-cancer drugs inside the core so that, in addition to the presence of miRNAs, there is a combination of drugs and thus multiple anti-cancer actions. Once the parameters for the preparation of NPs with miR-34a were optimized, it was decided to include anti-cancer drugs inside the core so that, in addition to the presence of miRNAs, to get multiple anti-cancer actions:

- **miRNA-Doxorubicin nanoparticles (miRDx-NPs):** 10mM doxorubicin solution was prepared in DMSO:PBS 1:1. 5.4mg of doxorubicin was weighed and added into 1.5ml Eppendorf tube with 500µl of DMSO and 500µl of PBS. The tube was vortexed in order to achieve proper mixing and dissolution of the drug. Doxorubicin solution was inserted, during preparation, before the homogenization step, by inserting 2µl of Doxorubicin solution at the same time as the 50µl of miRNA.
- **miRNA-Doxorubicin-Resveratrol nanoparticles (miRDxRs-NPs):** 88mM Resveratrol solution in DMSO was prepared. 5mg of Resveratrol was weighed, these were added into 1.5ml eppendorf tube within which 250µl of DMSO was added. The whole was vortexed in order to obtain proper mixing and dissolution of the drug. The resulting Resveratrol solution was inserted, during preparation, before the homogenization step, by adding 2µl of Resveratrol solution at the same time as the 50µl of miRNA and 2µl of Doxorubicin solution.

For simplicity the different types of nanoparticles will be named throughout the work as: **mR-NPs** the basic nanoparticles with miRNA-34a, **mRDx-NPs** those with miRNA-34a and Doxorubicin in the core and **mRDxRs-NPs** those with miRNA-34a, Doxorubicin and Resveratrol in the core. It will be seen later **LbL-NPs**, those nanoparticles manufactured started by mRDxRs-NPs and complexed with two superficial layers, following a layer by layer technique using two polyelectrolytes plus the addition of drugs inside them.

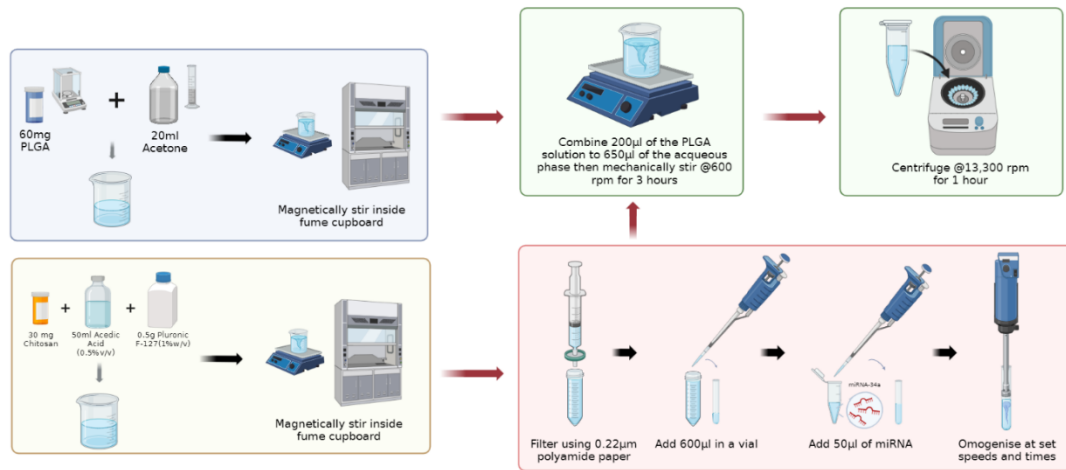


Figure 8: Protocol for the chitosan PLGA nanoparticles with miRNA-34a, created using BioRender.

Table 3: The Design of Experiment (DoE) for the preparation of the nanoparticles with miRNA140, created using BioRender

Run No.	Homogenisation speed (RPM)	Time of Homogenisation (s)
1	20000	30
2	18343	75
3	24000	139
4	20000	120
5	24000	75
6	24000	75
7	24000	75
8	29656	75
9	24000	75
10	28000	30
11	28000	120
12	24000	75
13	24000	11

**Table 4:** The Design of Experiment (DoE) for the preparation of the nanoparticles with miRNA 34a, created using BioRender

Run No.	Homogenisation speed (RPM)	Time of Homogenisation (s)
1	20000	30
2	16250	75
3	27500	138
4	20000	120
5	27500	75
6	27500	75
7	27500	75
8	35000	75
9	27500	75
10	31250	30
11	31250	120
12	27500	75
13	27500	11

#### 4.5 Layer-by-Layer Nanoparticles preparation

Once the fabrication procedures were optimized and the resulting nanoparticles were characterized, two superficial layers of polyelectrolytes on the miRDxRs-NPs surface were obtained by using the Layer by Layer technique that exploited the opposite charge between electrolyte solutions. The miRDxRs-NPs possessed a positive charge, so the first layer to obtain was negative, made of a pectin solution (using pectin previously extracted from cocoa biowaste) by dissolving 20g in 20ml of Sodium acetate buffer at pH 5. For the second layer, which must be positive so that it can interact electrostatically with the pectin layer, chitosan was used and again it was used a 1mg/ml solution of chitosan in sodium acetate buffer at pH5. Briefly, starting with the previously manufactured nanoparticles, the solution was centrifuged (Thermo Scientific™ Pico™ 17 Microcentrifuge was used) for 30min at 13,300 rpm in order to collect the particle pellet. The supernatant was then removed, the pellet was suspended in 100µl of SAB and the first electrolyte solution (pectin positive charge solution) was added until eppendorf tube 1.5ml was filled. At this point, gently pipetting, the two drug solutions (Doxorubicin and Resveratrol solutions previously prepared) were added (5µl of each). The Eppendorf tube was shaken for 20min at 120rpm thus allowing the pectin layer to homogeneously arrange itself around the positively charged nanoparticles and allowing the drug to be able to remain trapped in the forming layer. At this point it was re-centrifuged to collect the now-negative pellet, remove the supernatant by collecting it for further encapsulation assays, suspended in SAB and finally washed with water buffer at pH5 to remove all non-electrostatically attached residues by shaking for a shorter time. Then it was possible to start forming the second layer by going through the same steps, of course using the chitosan solution instead of pectin solution.

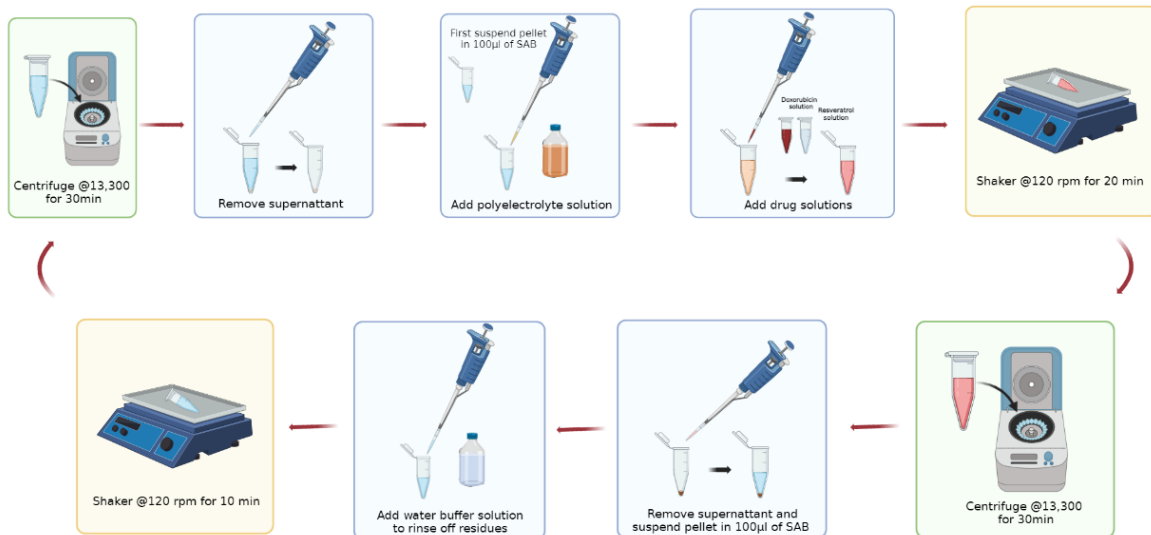


Figure 9: Protocol for layer by layer nanoparticles (LbL-NPs), created using BioRender.

#### 4.6 Characterization of the Nanoparticles

The mean size, zeta potential, and PDI were measured via DLS; the size was expressed as the mean and the value of the most appropriate peak  $\pm$  standard deviation, the zeta potential was expressed as the mean  $\pm$  standard deviation and the PDI is the value output. To prepare the samples for DLS, the supernatant was removed from the vials using a pipette, being careful not to remove any of the sediment at the bottom which contains the nanoparticles, then diluted using distilled water and gently mixed. The resulting solution was filtered using a 0.22 $\mu$ m polyamide filter to remove any large aggregates and make a 1:10 dilution in RNA-free water before being added to the Zetasizer cuvette, which was run three times, with the most appropriate result being considered. The size is established by how quickly the nanoparticles move; larger particles tend to experience slower Brownian motion whereas smaller particles are much faster<sup>[109]</sup>. The morphology of the nanoparticles was determined via a transmission electron microscope (TEM) (Philips CM 100 Compustage FEI) at 100kV. This method returns a highly magnified image, allowing us to clearly determine the resulting shape of the nanoparticle. A beam of electrons is shone through the sample, causing only portions of the electrons to be transmitted depending on the thickness and electron transparency of the sample. The transmitted portion is focused onto a phosphor screen, generating light, and returning an image<sup>[112]</sup> which was captured using an AMT CCD camera (Deben). Afterwards, the images were input into a software, called ImageJ, where they were analyzed to reveal their precise measurements for diameter. The way in which the samples were prepared is the same way as in section 4.4 of this project.

#### 4.7 miRNA 140 Evaluation of Entrapment Efficiency

From the results and analysis, the most successful speed and time of homogenization, 24,000rpm and 75 seconds, was selected for the remanufacture of the nanoparticle with miR-140 to evaluate the entrapment efficiency. The protocol for creating the nanoparticle, described in section 4.4, was followed. Once centrifuged, the supernatant was removed from the vials using a pipette, being careful not to remove any of the sediment, before 1ml of RNase-free water was added. The RNase-free water and sediment were gently homogenized to redisperse the nanoparticles, and then separated into two equal samples (500µl each). The value of entrapment efficiency was found via a NanoDrop spectrophotometer (Thermo Scientific™ NanoDrop™ 2000/2000c Spectrophotometers was used). This works by looking at the absorbance of light from the sample and calculating the concentration accordingly. The samples were centrifuged for 5 minutes before the supernatant was measured – this was done twice. After, the supernatant was removed, and the sediment was redispersed in 100µl of RNase-free water and measured a final time. This method uses the Lambert-Beer law <sup>[113]</sup>

$$A = \epsilon LC \quad (\text{Eq.6})$$

A = absorbance

L = optical path length (cm) C =  
concentration (mol/dm<sup>-3</sup>)

ε = molar extinction coefficient (L mol<sup>-1</sup> cm<sup>-1</sup>)

Therefore, rearranging this to calculate concentration is:

$$C = A/\epsilon L \quad (\text{Eq.7})$$

The optical path length is known for the spectrophotometer used. The absorbance is found from  $\log(I_0/I)$ , where  $I_0$  is the light entering the sample and  $I$  is the light exiting the sample. The molar extinction coefficient is a known value for the material being tested – in this case it would be for RNA. The values returned from the NanoDrop are the concentration and the absorption levels at wavelengths of 230nm, 260nm, and 280nm. These wavelengths measured correspond to the absorption of the light by salts, nucleic acids, and proteins respectively <sup>[114]</sup>; using these values the purity of the samples is calculated, as a fraction of A260/A280 for proteins and A260/A230 for salts – the optimal values are >2 and >1.8 for RNA samples respectively.

## 4.8 Evaluation of miRNA-34a, Doxorubicin and Resveratrol Encapsulation

From the results and analysis, the most successful speed and time of homogenization, 27500 rpm and 75 seconds, was selected for the remanufacture of the nanoparticle to evaluate the entrapment efficiency. The protocol for creating the nanoparticle, described in section 4.2, was followed. Once centrifuged, the supernatant was removed from the vials using a pipette, being careful not to remove any of the sediment, before 1ml of RNase-free water was added. The supernatant collected was used to measure the quantity of miRNA encapsulated for all the three types of NPs, the quantity of Doxorubicin encapsulated for miRDx-NPs and miRDxRs-NPs and the Resveratrol encapsulation for miRDxRs-NPs. An indirect measurement was used: for each sample, the amount of miRNA and drugs in the supernatant was analyzed and the encapsulated amount was obtained by subtraction from the amount originally entered. For LbL-NPs, the amount of Doxorubicin and Resveratrol encapsulated in the two layers was calculated by analyzing the supernatant collected at the end of the second centrifugation for each layer, respectively.

### 4.8.1 miRNA-34a Encapsulation

The value of entrapment efficiency was found via QuantiFluor assay, analyzing the supernatant. The amount of un-encapsulated miRNA-34a in supernatant was determined using an ultraviolet-visible (UV-Vis) spectrofluorometer by measuring the Fluorescence value. The QuantiFluor® RNA System contains a fluorescent RNA-binding dye (492nmEx/540nmEm) that enables sensitive quantitation of small amounts of RNA in purified samples. First of all it was necessary to prepare the QuantiFluor® RNA Dye working solution by diluting the QuantiFluor® RNA Dye 1:2,000 in 1X TE buffer. Then RNA standards were prepared by serially diluting QuantiFluor® RNA Standard (100ng/μl) in order to prepare RNA Standard Curve. Finally, 200μl of QuantiFluor® RNA Dye working solution was pipetted into each well that was intended for an unknown, blank or standard sample. Then standards and unknown samples were added to their corresponding well, incubating for 5 minutes at RT protected from light before measuring the fluorescence at 492nmEx and 540nmEm. The measures were taken using a multiplate reader (FLUOstar Omega, BMG Labtech, Germany). Each sample was read in triplicate and referred to the standard curve generated using the standard RNA concentration. The encapsulation efficiency was calculated as follow:

$$EE(\%) = \frac{(A-B)}{A} * 100 \quad (\text{Eq.8})$$

A and B are the weights of total amount (μg) of entered miRNA-34a and the miRNA-34a fraction recovered (μg) from the supernatant after the centrifugation, respectively.

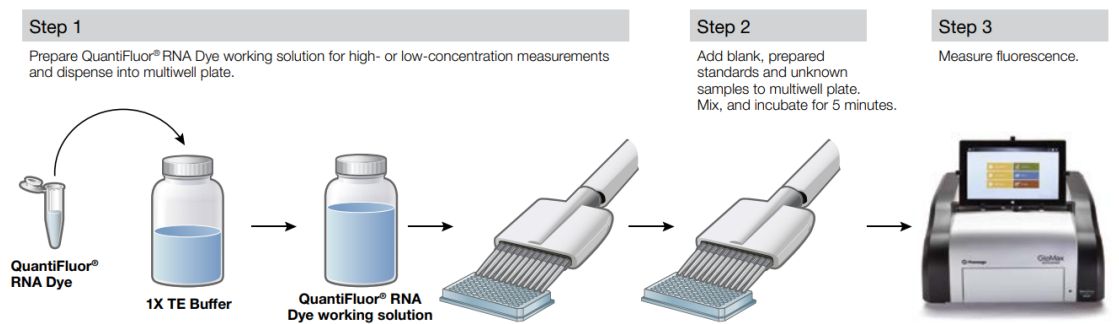


Figure 10: Protocol of QuantiFluor assay for measure the concentration of miRNA encapsulated.

#### 4.8.2 Doxorubicin and Resveratrol Encapsulation

The encapsulation efficiency of Doxorubicin and Resveratrol in manufactured nanoparticles was evaluated by indirect measurements from the un-encapsulated Doxorubicin and Resveratrol recovered from the supernatant. The amount of un-encapsulated DOX in supernatant was determined using an ultraviolet-visible (UV-Vis) spectrofluorometer (FLUOstar Omega, BMG Labtech, Germany) by measuring the absorbance values. The encapsulation efficiency was calculated as previously, following Eq.8 where A and B are the weights of total amount of added drugs and the drugs fraction recovered from the supernatant after the centrifugation, respectively. Supernatants collected were analyzed at 480 nm to detect DOXO and 285nm to detect Resveratrol. Each sample, for both the drugs, was read in triplicate and, referred to a standard curve generated using free Doxorubicin and Resveratrol at known concentrations. The supernatant recovered from NPs without DOX and Resveratrol was used for baseline correction.

#### 4.8.3 Layer by layer NPs Encapsulation

For LbL-NPs, the amount of Doxorubicin and Resveratrol encapsulated in the two forming layers was calculated by analyzing the supernatant collected at the end of the second centrifuge for each layer, respectively. The same steps were performed to calculate the amounts encapsulated in the core of the nanoparticles functionalized by layer by layer. The amount of miRNA, Doxorubicin and Resveratrol encapsulated in the core was measured first, and then it was measured the amount of Doxorubicin and Resveratrol entrapped in the two layer as previously described.

#### 4.9 Evaluation of miRNA-34a, Doxorubicin and Resveratrol Release

The evaluation of the release was determined via UV/VIS spectroscopy. To evaluate the release of miR-34a, Doxorubicin and Resveratrol from all the four manufactured nanoparticles, for each sample prepared following the procedures in section 4.4, the final pellet was dispersed in 1ml of PBS (pH 7.4). The samples were stored at 37°C and continuously vortex at 400 rpm (Thermo Fisher Vortexer). The release was analyzed at different time points: 10min, 20min, 40min, 80min, 160min, 320min, 11h, 24h, 48h, 4day, 5day, 6day. At each time point, samples were shaken for 5 minutes with the shaker at 60rpm and then transferred to centrifugal filter tubes and centrifuged at 13000g for 30 min to separate released miRNA and drugs from miRNA and drugs still encapsulated within the nanoparticles. The supernatant was collected for the analysis of miRNA release by the QuantiFluor Assay measuring the fluorescence and for the analysis of Doxorubicin and Resveratrol measuring the absorbance at 480nm and 285nm respectively (FLUOstar Omega, BMG Labtech, Germany). Standard curves have been previously generated with known concentrations of miRNA, Doxorubicin and Resveratrol. For each type of NP, the cumulative release was calculated adding the release of each time point to the previous one. This process was repeated by suspending remaining particles in PBS, vigorously shaking for 5 min and incubated at 37°C. Each sample was read in triplicate and the data shown represent the mean and SD of number independent experiments.

#### 4.10 Statistical analysis

The DoE of extracted Pectin was analyzed by response surface methodology (RSM). Statistical analysis was performed on the extraction parameters (Temperature (°C), Time (min) and Ratio (g/ml)), analyzing Pareto charts, Surface plots and Contour plots to evaluate their effects on the analytical determinations performed on the extracted pectin: GA(%), Zeta potential (mV) and Yield (%). Moreover, it was performed also the Response Optimization in order to find the optimal parameters for minimize the Zeta potential and maximize Yield and Galacturonic acid content. The DoE of miR-NPs was analyzed by response surface methodology (RSM), analyzing data as well as it was described above for Pectin. Whilst, the sizes of the four manufactured NPs and the LbL-NPs (from bare core to first and second layer) and released miR-34a, Doxorubicin and Resveratrol at the two final time points, were processed by one-way ANOVA, with mean separation by Tukey's test at 95% confidence level in order to understand whether there was indeed statistically significant difference between the various groups in terms of size and releases or whether this difference is due to the fact that the variability within the groups might be greater than the variability between them and thus lead to numerically different but not statistically significant values.

#### 4.11 Cell Culture

The human osteosarcoma SaoS-2 and U2OS cell line were purchased from Sigma-Aldrich. Cells were grown in DMEM containing 10 % FBS, 100 U mL<sup>-1</sup> penicillin, and 100 µg mL<sup>-1</sup> streptomycin at 37 °C in a 5 % CO<sub>2</sub> atmosphere. Cells were seeded in a 75 cm<sup>2</sup> flask, and when 70–80 % of confluence was reached, cells were subcultured (1 mL TrypLE™ per 75 cm<sup>2</sup> flask).

#### 4.12 Sarcospheres preparation

Preliminarily, a falcon with methylcellulose in 0.25% DMEM was prepared. The development of the spheroids was achieved by the low attaching technique with minor modifications. Cells were seeded in Costar UltraLow Attachment 96 well-plates with a density of 100,000 cells/well in DMEM culture medium supplemented with a specific factors cocktail composed by 0.25% Methylcellulose in DMEM. Briefly, a flask with growing cells (90% of confluence) was rinsed with sterile PBS, and then, cells were harvest by adding 3ml trypsin and incubating for 5 min at 37°C. Once detached, the cells were counted and the suspension was adjusted to have a concentration of 100,000 cells/well; this concentration was selected to get 400 µm diameter spheroids at the beginning of the treatment with the compound. The total amount of cells to be retained after centrifugation step is calculated as follow:

$$n^{\circ}\text{cells} = n^{\circ}\text{well} * 100,000 \quad (\text{Eq.9})$$

$n^{\circ}\text{well}$  is the number of well we want , so the number of sarcosphere to prepare because there will be one sarcosphere each well. Once discarded the surplus amount of cell, the remained cell suspension was centrifuged at 1,2000 rpm for 5 min and then dispersed with the new medium with methylcellulose that will contribute to cell aggregation and energetically pipetting so as to homogeneously disperse the cells. At this point, 150µl of this mix of cells and medium was pipetted in each well and subsequently incubated at 37° to allow the sarcospheres to form. The cocktail of 0.25% methylcellulose and medium was added to each well every 2 days for a total of 20 days of culture at 37 °C and in 5% CO<sub>2</sub> atmosphere conditions, observing sarcospheres formation. The total amount (ml) of 0.25% methylcellulose/DMEM to be added to the right amount of the centrifuged cells pellet was calculated as follow:

$$\text{Sarcosphere culture cocktail (ml)} = (n^{\circ}\text{well} * 150\mu\text{l} + 1,5 \mu\text{l} * n^{\circ}\text{well}) * 10^3 \quad (\text{Eq.10})$$

The plate was cultured under the standard conditions for 21 days, replacing 50 % of the culture media every 48 h.

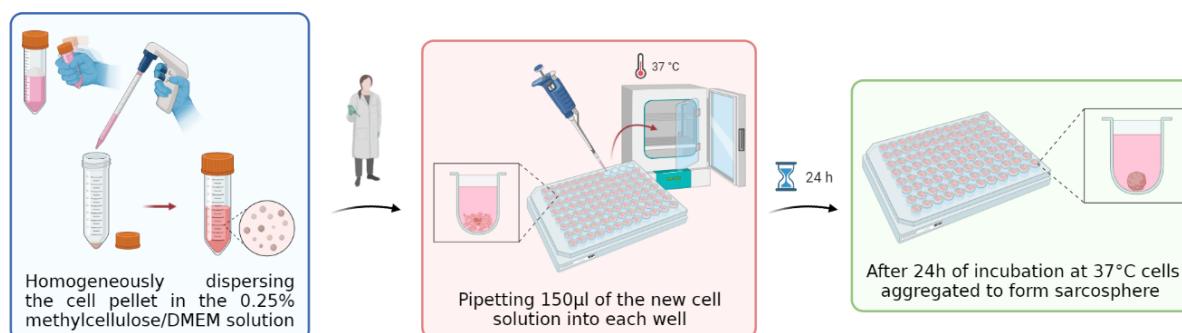


**Figure 11:** Protocol for Sarcospheres preparation starting from detached cells in pellet, created using BioRender.

## 4.13 Sarcospheres characterization

### 4.13.1 Sarcospheres size over time

It was decided to analyze the size of the manufactured spheroids over time, both for those obtained with SaoS-2 and those with U2OS. Seven time points were chosen (1-3-5-6-10-15-21 days) at which the spheroids were imaged by EVOS M5000 fluorescence microscope and then analyzed using ImageJ software by measuring the diameter. The results are shown in terms of mean value and standard deviation of all analyzed samples.

### 4.13.2 Scanning electron microscopy (SEM) analysis

Tescan Vega 3LMU scanning electron microscope was used for analyzing the morphology of cellular samples. At the chosen time point, samples were fixed in 2% glutaraldehyde for 1h at 4°C, rinsed in PBS twice and dehydrated in ethanol grades (30 min in 25% EtOH, 30 min in 50% EtOH, 30 min in 75% EtOH, 30 min in 95% EtOH and twice 1h in 100% EtOH). Samples were dried to critical pointing (BALTEC 030, Leica Geosystems Ltd, UK) mounted on carbon discs and gold-coated using Polaron E5000 SEM Coating unit (Quorum Technologies Ltd, UK) as shown in Figure 12. Samples were imaged at different magnifications.



**Figure 12:** Sarcospheres mounted on carbon discs for SEM analysis.

#### 4.14 Cellular Test

Two types of cell models were created, for both cell types, testing them with the four types of manufactured nanoparticles: 2D cells model represented by bidimensional cells culture in Greiner CELLSTAR® multiwell 48 with three different densities (2000,4000,8000 cells/well) and 3D Sarcospheres with a density of 100000cells/well in Costar UltraLow Attachment 96 well-plates, as shown in Figure 13.

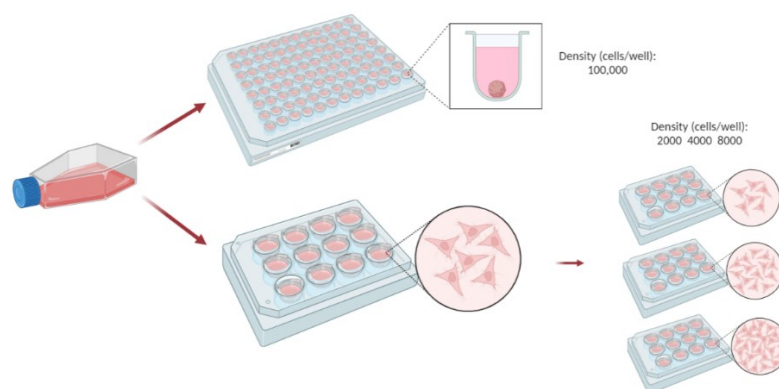


**Figure 13:** Cellular models for testing manufactured nanoparticles. (a) 3D model – Sarcospheres with density of 100000 cells/well in Costar UltraLow Attachment 96 well-plates, (b) 2D model – Bidimensional culture in Greiner CELLSTAR® multiwell 48, with three different densities (2000, 4000, 80000 cells/well).

These samples were treated with the nanoparticles (miR-NPs, miRDx-NPs, miRDxRs-NPs, LbL-NPs), incubating them for 24h, 48h and 72h. At each time point cell viability, metabolic activity and cell morphology were analyzed. Two different concentrations of nanoparticles were used accordingly to the cell model, significantly increasing the amount for the Sarcospheres, given the large number of cells and the complexity of the model.

##### 4.14.1 PrestoBlue assay

PrestoBlue™ Cell Viability Reagent is a resazurin-based ready-to-use reagent that is reduced by metabolically active cells, providing a quantitative measure of viability and proliferation of the cells. When cells are alive and healthy, they maintain a reducing environment within their cytosol so upon entering a living cell, PrestoBlue™ reagent is reduced to resorufin which is red in color and highly fluorescent. The health of the cell can be then monitored by the change in fluorescence. Non-viable cells cannot reduce the indicator dye and therefore do not generate a change in signal. Using this technique for both cell types (SaoS-2 and U2OS), metabolic activity was analyzed before and after the incubation with the different types of NPs. The analysis was performed on the 2D model (with cells densities of 2000, 4000 and 8000 cells/well) and on the 3D model of Sarcospheres (100,000 cells/well). Briefly, samples were incubated with the NPs for 24h,48h and 72h, and at each time point PrestoBlue solution was prepared by diluting the PrestoBlue™ reagent in DMEM (1:10) protected from light and vortex to obtain a solution. Then 1ml of solution was added to the samples previously washed with PBS

and the fluorescence (Ex544nm/Em590nm) was read at 20min, 40min, 1h and 1.5h by using a Filter-based FLUOstar® Omega multi-mode reader.

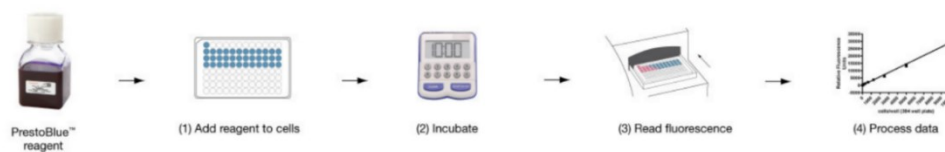


**Figure 14:** Protocol of PrestoBlue™ Cell Viability assay

#### 4.14.2 Live/Dead assay

In order to investigate the effects of the manufactured nanoparticles on the cells viability, Live/Dead assay (LIVE/DEAD Cell Imaging Kit, Life Technologies, UK) was performed before and after the incubation of the cells (both 2D and Sarcosphere models) with the different nanoparticles. This fluorescence-based kit combines calcein AM and ethidium bromide to yield two-colour discrimination of the population of live cells (green) from the dead cells (red). Live cells are distinguished by the presence of intracellular esterase activity, determined by the enzymatic conversion of the virtually nonfluorescent cell-permeant calcein AM to the intensely fluorescent calcein that is well retained within live cells, producing an intense uniform green fluorescence (ex/em ~495 nm/~515 nm). EthD-1 enters cells with damaged membranes producing a bright red fluorescence in dead cells (ex/em ~495 nm/~635 nm). For both cell types and models, cells samples were incubated with the NPs for 24h, 48h and 72h; at each time point they were washed twice with DPBS and incubated with 100 µl of L/D staining realized mixing 1µl of Calcein with 4µl of Ethidium in 2ml of DPBS. Samples were incubated for 30 min at 37°C and then imaged using EVOS M5000 fluorescence microscope from Thermo Fisher Scientific.

#### 4.14.3 Immunostaining assay

Cell's morphology was observed by staining their cytoskeleton using Actin Red™ 555 ReadyProbes Reagent (purchased from Thermo Fisher Scientific) and nucleus observed with 4',6-diamino-2-phenylindole (DAPI). Both cell types (SaoS-2 and U2OS) and models (2D and Sarcospheres cultures) were analyzed by immunostaining investigating the effects of the 4 types of NPs on their morphology. Samples were incubated with NPs for 24h,48h and 72h, and at each time point cell samples were fixed in pre-warmed 4% w/v paraformaldehyde (PFA) for 30 min at 37°, in order to fix the cells in a non-stress pose. Then the PFA was removed, and cells were rinsed twice in 0.1%v/v Tween20 (Sigma Aldrich, UK) in PBS. Then, ActinRed solution was made by putting 2drop/ml of PBS and about 150µl of this solution were put into each well and incubated for 20 min at RT, protected from light. Then they were washed twice in 0.1%PBS/Tween20 solution in order to remove residues of ActinRed and finally one drop of Dapi was put in each well, left for 6 min at RT and then rinsed in PBS. Samples were imaged using EVOS M5000 fluorescence microscope from Thermo Fisher Scientific.

## 5. Results and discussions

### 5.1 Physico-chemical characterization of the extracted pectin

#### 5.1.1 Extraction yield

Table 5 provided the experimental data of the yields obtained from the pectin extraction process and the measurements were taken following the method previously described. The highest yield obtained was 22.7% from sample 8, at the second highest temperature (70°C) for 50 minutes and 3g of biowaste utilized during the extraction. The lowest yield (11.3%) was obtained for sample 13 with 6.34g of cocoa biowaste at 67.50°C, for ~24 minutes in the ultrasonic cleaner. This sample also corresponded to the lowest used ratio value of all, at 23.67g/ml. For all the others samples it could be seen a similar extraction yield, above or close to 15%. The use of the Buchner funnel to separate solid and liquid phases was more efficient than separating them by hand and could therefore improve the yield of pectin as there would be a reduction in loss during manufacture.

*Table 5: Yield measurements for the different samples of extracted pectin.*

Trial No.	T (C)	Time (min)	Weight to measure (g)	pectin weight (g)	Yield (%)
1	70.00	45.000	5.00	0.8110	16.22
2	50.00	90.000	3.00	0.4531	15.10
3	60.00	67.500	3.75	0.7863	20.97
4	70.00	90.000	5.00	0.7345	14.69
5	60.00	67.500	3.75	0.7300	19.47
6	50.00	45.000	5.00	0.8258	16.52
7	70.00	45.000	3.00	0.4511	15.04
8	70.00	90.000	3.00	0.6796	22.65
9	60.00	67.500	3.75	0.5684	15.16
10	50.00	90.000	5.00	0.8811	17.62
11	50.00	45.000	3.00	0.5551	18.50
12	60.00	67.500	3.75	0.6698	17.86
13	60.00	67.500	6.34	0.7142	11.26
14	60.00	67.500	3.75	0.6168	16.45
15	43.67	67.500	3.75	0.5918	15.78
16	60.00	67.500	3.75	0.6920	18.45
17	60.00	104.243	3.75	0.7609	20.29
18	60.00	67.500	2.66	0.4695	17.65
19	60.00	30.758	3.75	0.7579	20.21
20	76.33	67.500	3.75	0.6525	17.40

### 5.1.2 Fourier-transform infrared spectroscopy - FTIR

Samples were prepared for the FTIR analysis following the method previously described. The spectrum of the pectin extracted from the cocoa biowaste during this study was compared with the spectrum from commercial apple pectin and they were shown in Figure 15. It could be noticed from the graphs the presence of similar peaks. The presence of absorption peaks recorded around 3500-3300  $\text{cm}^{-1}$  were caused by O-H stretching, while characteristic absorption peak of pectin-reproduced polysaccharides due to C-H stretching of  $\text{CH}_2$  groups was observed between 3000-2800  $\text{cm}^{-1}$ .<sup>[115][116]</sup> The bands around 1750 and 1550  $\text{cm}^{-1}$  correspond to the esterified carboxyl group ( $\text{COO-R}$ ) and non-esterified carboxyl groups ( $\text{COO}^-$ ) of pectin, respectively<sup>[117]</sup>. The tendency of increasing intensities and band area of esterified carboxyl groups may indicate an increase in degree of esterification<sup>[118]</sup>. Bands related to the stretching of the C-O bond were observed between 1300 and 1000  $\text{cm}^{-1}$ <sup>[119]</sup>, while the absorption band at 1225  $\text{cm}^{-1}$  was due to the cyclic C-C bond in the ring structure of pectin. Finally, the region between 1100-950  $\text{cm}^{-1}$  has been reported for the spectral identification of galacturonic acid in peptide polysaccharides<sup>[120]</sup>. It could be then seen from the two graphs that the peaks for extracted and commercial pectin were at around the same wavelengths, thus indicating structural and bonding similarity between the two ones.

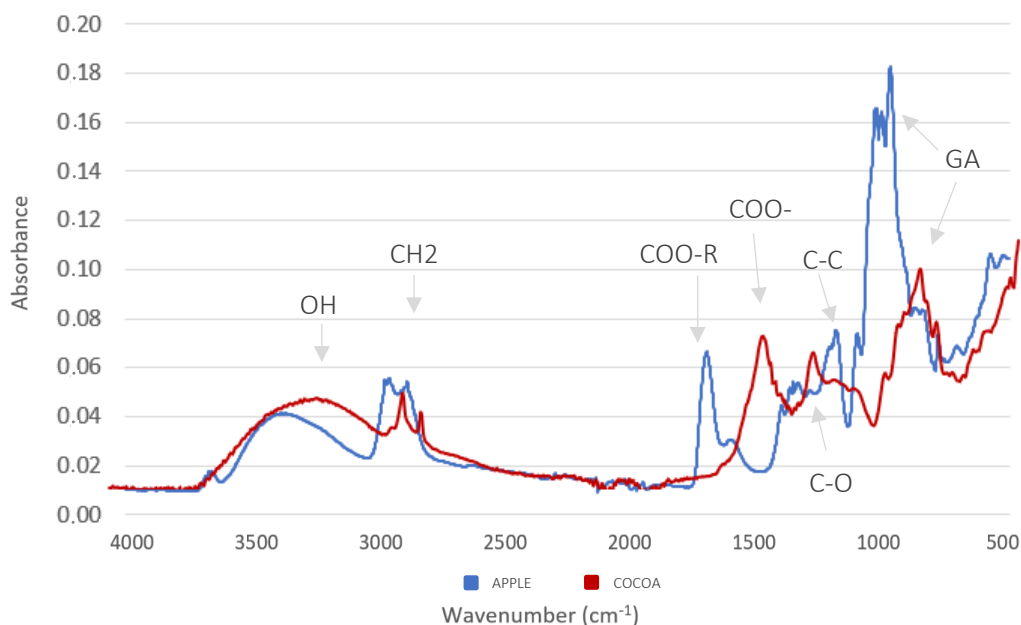


Figure 15: FTIR spectrum of Pectin extracted from cocoa biowaste after basic extraction (0.05M - pH 12).

### 5.1.3 Dynamic Light Scattering - DLS

Table 6 showed the zeta potential of the extracted pectin samples. This data showed that the charge of the diluted pectin was strongly negative with the highest negative value for sample 8 with -58.8mV. As it could be seen from the results, a strong negative charge was observed for each of the samples. The strong negative charge means that the pectin can be used easily as a polyelectrolyte (polyanion) in the production of the nanocoating, for our LbL-NPs, through layer-by-layer assembly, using it in conjunction with a positively charged substance, like chitosan<sup>[122][123]</sup>. The process parameters of the best sample in term of charge were then 70°C for temperature, 90min and ratio of 50g/ml. In Figure 16 was reported an example of zeta potential result calculated for an extracted pectin sample through DLS analysis.

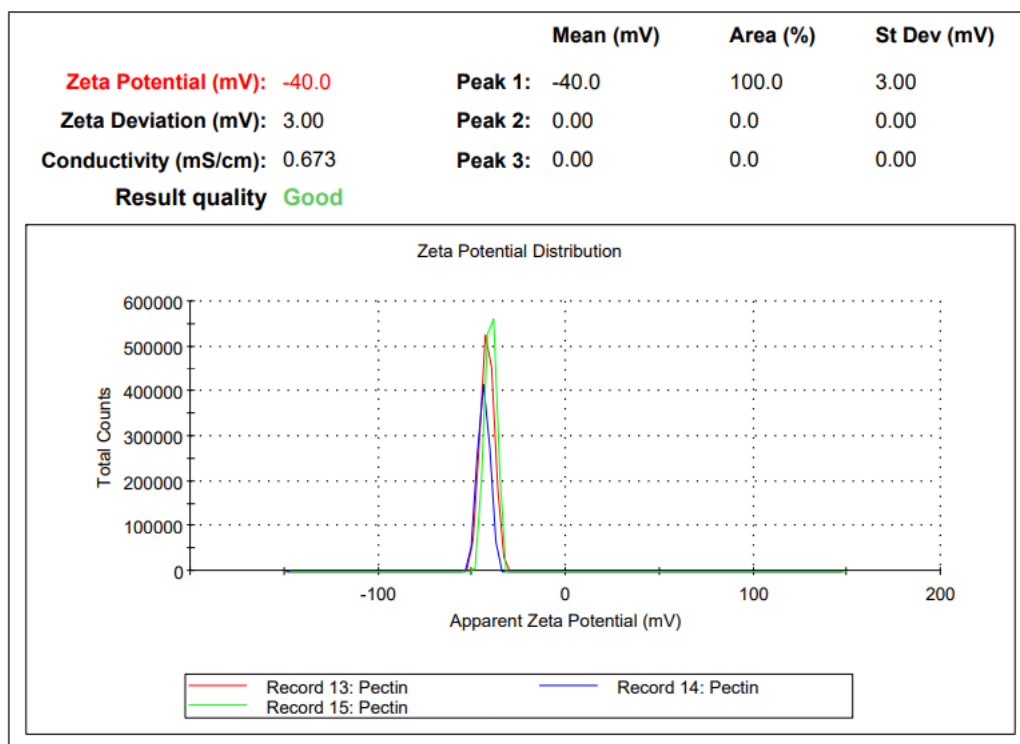


Figure 16: Zeta potential of extracted Pectin. Measured using Dynamic Light Scattering analysis.

**Table 6:** Zeta Potential measurements of the different samples from pectin extracted.

Trial No.	Mean ZP ± Dev.st ZP (mV)
1	-57.72 ± 1.70
2	-53.77 ± 1.05
3	-51.70 ± 2.23
4	-44.64 ± 1.11
5	-47.91 ± 2.66
6	-51.67 ± 2.99
7	-50.68 ± 1.88
8	-58.81 ± 2.39
9	-50.79 ± 2.36
10	-47.57 ± 2.47
11	-49.96 ± 3.18
12	-50.18 ± 1.93
13	-52.01 ± 3.61
14	-43.00 ± 2.41
15	-47.24 ± 4.01
16	-39.48 ± 3.96
17	-48.52 ± 1.63
18	-48.90 ± 2.26
19	-51.66 ± 1.22
20	-50.90 ± 1.52

#### 5.1.4 Galacturonic acid measurement

Table 7 showed the Galacturonic acid (GA) content of the extracted pectin at the measured pH 12. It was important in order to evaluate the quality of the final extract, taking into account that commercial pectins have a galacturonic acid content greater than 65%<sup>[120]</sup>. The greater is the Galacturonic acid content, the greater is the quality of the extracted pectin. The Galacturonic acid content of the extracted pectin ranged from 16% (samples 6 and 13) to of 42% (sample 3, 5 and 8). High percentage of GA was also seen in samples 4, 9, 12 and 14 with percentage of around 35%. All these were characterized by extraction temperature from 60°C on, so this observation could suggest that higher values of temperature extraction could lead to higher percentage of galacturonic acid. It was actually seen in statistical result section that temperature parameter was significant in influencing galacturonic acid content, in particular at higher values of temperature corresponded higher percentages of galacturonic acid.

**Table 7:** Galacturonic acid content (%) of the different samples from pectin extracted.

Trial No.	T (C)	Time (min)	Ratio (g/ml)	GA (%)
1	70.00	45.000	30.00	26.9697
2	50.00	90.000	50.00	22.1212
3	60.00	67.500	40.00	42.1210
4	70.00	90.000	30.00	35.7143
5	60.00	67.500	40.00	42.3810
6	50.00	45.000	30.00	16.2771
7	70.00	45.000	50.00	29.2208
8	70.00	90.000	50.00	41.8571
9	60.00	67.500	40.00	38.3983
10	50.00	90.000	30.00	18.8745
11	50.00	45.000	50.00	25.8442
12	60.00	67.500	40.00	35.1080
13	60.00	67.500	23.67	15.7576
14	60.00	67.500	40.00	39.3070
15	43.67	67.500	40.00	21.4900
16	60.00	67.500	40.00	32.5540
17	60.00	104.243	40.00	26.1039
18	60.00	67.500	56.33	31.8182
19	60.00	30.758	40.00	33.2200
20	76.33	67.500	40.00	24.9351

The pectin thus obtained from the cocoa biowaste was used as a polyelectrolyte in the preparation of the LbL-NPs. The parameters that were found to be the most optimal for the required coating, regarded sample 8, since it showed the highest values of yield and galacturonic acid, which therefore symbolize higher quality of the extracted pectin. Sample 8 also exhibited the biggest negative zeta potential among all, which was very important since a strong negative charge was required to homogeneously complex around the positively charged miRDxRs-NPs. The chosen sample had a zeta potential value of -58.81mV, GA percentage of 41.8% and Yield equal to 22.65%; as extraction parameters, from Table 2 70°C, 90 time 50g/ml ratio were used. From this optimized extracted pectin MeO degree and esterification degree were calculated as previously reported in section 4.3 and there were found MeO percentage equal to 25.8 % (st dev 5.7%) and DE of 58.9% (st dev5.3%).

### 5.1.5 Statistical results

The parameters varied in each trial could be seen in Table 2. Using Minitab, the results were input, and statistical analysis was performed to evaluate whether either parameter was statistically significant in influencing the yield, galacturonic acid content and zeta potential of the extracted pectin. Contour and surface plots of the results against the parameters could be seen in Figures 18, 19 and 20 for yield, zeta potential and GA respectively, as well as Pareto charts – these display how close each parameter, or a combination of each, was to being statistically significant – Figure 17.

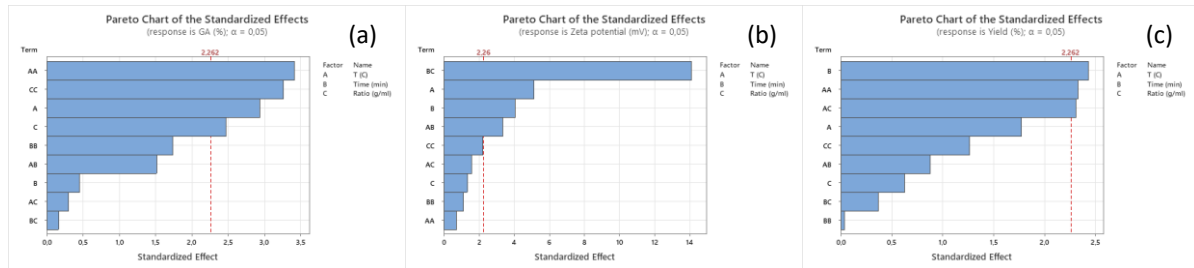


**Figure 17:** (a) Pareto charts for GA (%) showing the alpha value and the standardized effect of each parameter on the resulting GA of the extracted Pectin, (b) Pareto charts for Zeta Potential (mV) showing the alpha value and the standardized effect of each parameter on the resulting Zeta Potential of the extracted Pectin, (c) Pareto charts for Yield (%), showing the alpha value and the standardized effect of each parameter on the resulting Yield of the extracted Pectin. All created on Minitab.

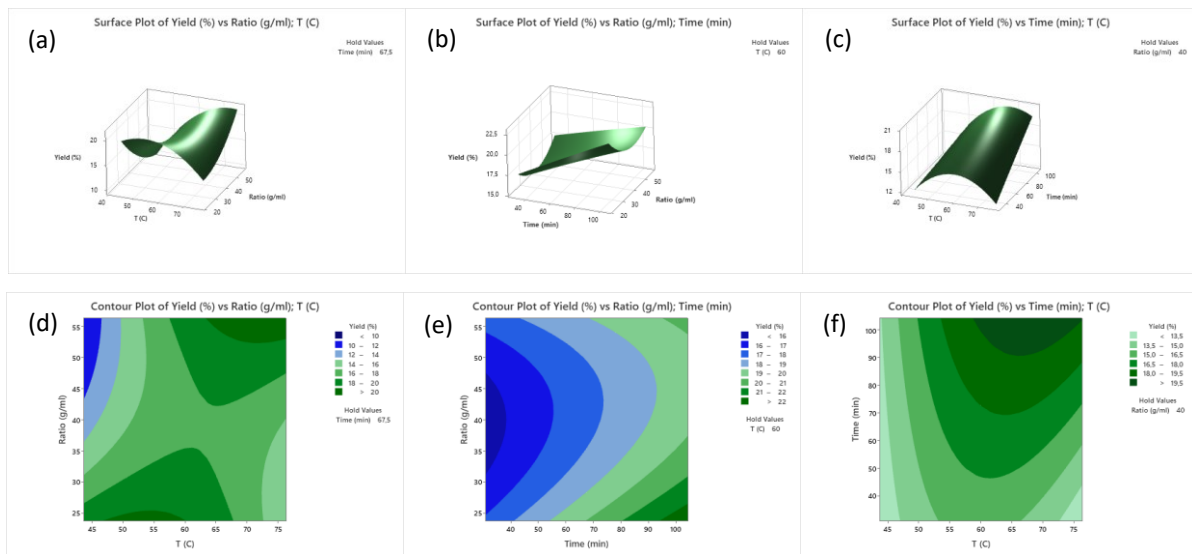


**Figure 18:** (a) Surface plot of Yield (%) against Ratio (g/mol) and T (°C), (b) Surface plot of Yield (%) against Ratio (g/mol) and Time (min), (c) Surface plot of Yield (%) against Time (min) and T (°C), (d) Contour plot of Yield (%) against Ratio (g/mol) and T (°C), (e) Contour plot of Yield (%) against Ratio (g/mol) and Time (min), (f) Contour plot of Yield (%) against Time (min) and T (°C). All created on Minitab.

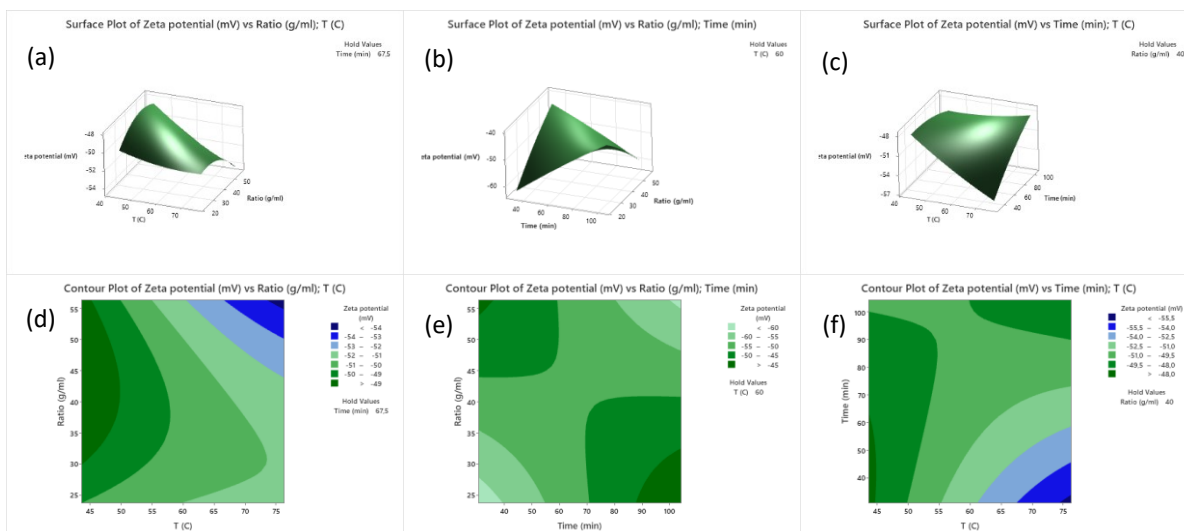


**Figure 19:** (a) Surface plot of Zeta potential (mV) against Ratio (g/mol) and T (°C), (b) Surface plot of Zeta potential (mV) against Ratio (g/mol) and Time (min), (c) Surface plot of Zeta potential (mV) against Time (min) and T (°C), (d) Contour plot of Zeta potential (mV) against Ratio (g/mol) and T (°C), (e) Contour plot of Zeta potential (mV) against Ratio (g/mol) and Time (min), (f) Contour plot of Zeta potential (mV) against Time (min) and T (°C). All created on Minitab.

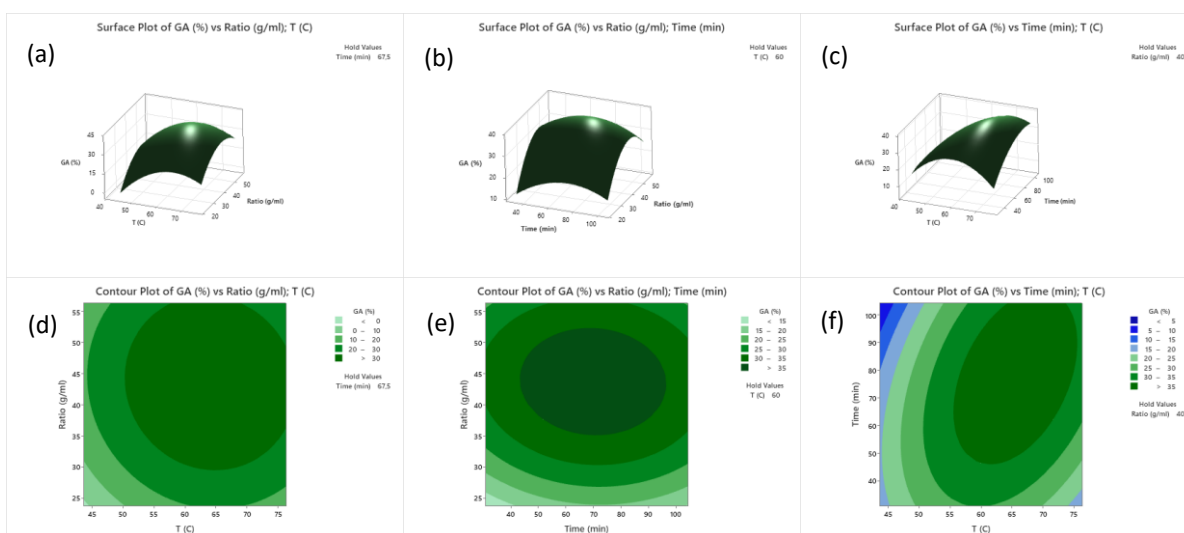


**Figure 20:** (a) Surface plot of GA (%) against Ratio (g/mol) and T (°C), (b) Surface plot of GA (%) against Ratio (g/mol) and Time (min), (c) Surface plot of GA (%) against Time (min) and T (°C), (d) Contour plot of GA (%) against Ratio (g/mol) and T (°C), (e) Contour plot of GA (%) against Ratio (g/mol) and Time (min), (f) Contour plot of GA (%) against Time (min) and T (°C). All created on Minitab.

Based on Pareto chart of the galacturonic acid, temperature (°C) and ratio (g/mol) exceeded the alpha value and, therefore, they were significant in influencing the GA of the extracted pectin. Looking at its Surface plot and Contour plot indeed centre points of temperature and ratio seemed to produce the most consistent results with the highest value of galacturonic acid. In Pareto chart of the zeta potential, temperature (°C) and time (min) exceeded the threshold value so they were significant in influencing the zeta potential of the pectin, although the greatest influence in this case was attributed to the combination of time (min) and ratio (g/ml) which exceeded the threshold by far more than the previous two parameters. From the pareto chart of the yield it could be seen that the combination of

temperature (°C) and ratio (g/mol) and the temperature (°C)-temperature (°C) exceeded the threshold slightly, while greater was the case of time which was significant in influencing the yield of the pectin. Looking at the surface plots, It was noticed some specific comfortable regions, especially for GA plot in which the central points were, for all of the combination, the most comfortable region. In order to have maximum values of GA, temperature (°C) was found to be in range 55-75°C, Ratio (g/ml) in 37-53g/ml and time (min) in 50-100 minutes. Changing parameters around these intervals gave the maximum percentage of galacturonic acid. Looking at the contour plot of the zeta potential, the most comfortable region with the highest negative values was achieved with high values of temperature (around 75-80°C), time in range 30-40 minutes and ratio above 55 g/ml. Based of Contour plot of the yield, a comfortable region with high values was achieved with high values of time, between around 90-110 minutes, low value of ratio (under 25 g/ml) and temperature in range 60-75°C.

R-squared values for each case from Minitab were also considered, the values were 78.8% for GA and 71.84% for yield and 90.54% for zeta potential; this suggests that for all the three characteristics there was optime correlation between the resulting values and the regression model. The full statistical results can be found in the appendix, section 9.1.

On these data it was performed also the Response Optimization using Response Optimizer on Minitab, in order to find the optimal parameters for minimize the zeta potential and maximize yield and galacturonic acid content. The results are shown in Figure 21.

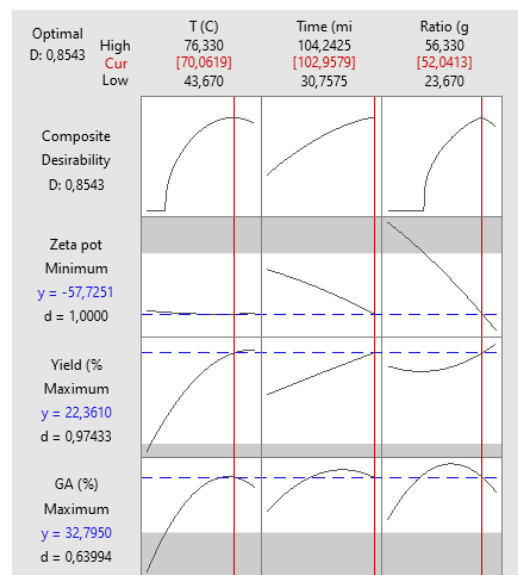


Figure 21: Response Optimization using Response Optimizer on Minitab

## 5.2 Characterization of manufactured NPs

### 5.2.1 Characterisation and Morphology

The size, zeta potential, and PDI were found using DLS analysis and the samples were prepared following the method previously described. The nanoparticles with Chitosa-PLGA-miR-140 demonstrated a mean diameter of 259.2nm, a mean PDI of 0.35 and a mean zeta potential of +17.4mV. While the nanoparticles with Chitosa-PLGA-miR-34a showed a mean diameter of 271.5nm, a mean PDI of 0.30 and a mean zeta potential of +29.1mV. PLGA is a polyanion, meaning it cannot interact with the miRNA; the chitosan packages the miRNA by electrostatic interaction between its positive amino residues and the negative phosphate residues of the miRNA, this provides the mean positive charge of the particle as well as helping to condense and protect the miRNA - as they form polyelectrolyte complexes - preventing some levels of nuclease degradation.<sup>[111]</sup> The results for miR-140 were shown in Table 8 and a graphical display of size distributions were presented in Figure 22, while in Table 9 and Figure 23 were shown the results for miR-34a and a graphical display of it, showcasing some of the differences from each trial; larger, thinner peaks correspond to a smaller PDI as the particles are less distributed, meaning the standard deviation is also proportionally smaller than what is seen for the particles with a large variety, as well as giving a mean size that is similar to the size found by the most appropriate peak.

**Table 8:** Characteristics of chitosan PLGA nanospheres with miR-140, obtained through DLS analysis.

Trial No.	Mean size (nm)	Size (by intensity) (nm)	Peak percentage(%)	PDI	Zeta Potential (mV)
Control	325.70	429.5 ± 197.00	88.9	0.369	46.4 ± 7.84
1	220.00	231.2 ± 96.10	92.3	0.301	34.2 ± 8.93
2	301.30	370.6 ± 178.00	100.0	0.193	23.0 ± 9.19
3	204.90	209.5 ± 70.26	96.9	0.209	11.4 ± 9.85
4	245.60	346.0 ± 195.20	100.0	0.272	1.1 ± 3.72
5	179.90	196.4 ± 57.12	100.0	0.111	28.6 ± 4.22
6	186.40	229.4 ± 109.40	100.0	0.167	30.6 ± 9.48
7	513.00	196.7 ± 44.56	31.9	0.619	1.8 ± 3.46
8	257.10	249.9 ± 89.88	95.7	0.326	36.5 ± 5.26
9	1176.00	247.2 ± 45.66	17.6	0.485	8.9 ± 4.68
10	504.40	276.6 ± 67.75	61.8	0.715	25.0 ± 3.44
11	463.70	259.0 ± 44.16	100.0	0.503	17.5 ± 2.12
12	507.60	151.4 ± 37.00	12.1	0.421	17.0 ± 6.01
13	307.00	405.0 ± 233.00	100.0	0.176	-9.07 ± 11.5
Mean	385.19	259.1 ± 123.16	78.4	0.350	17.43 ± 7.50

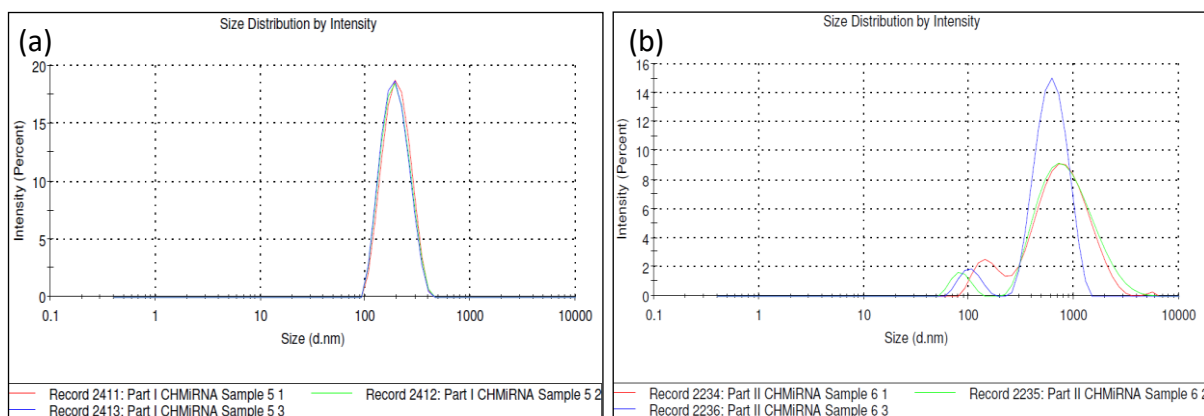


**Figure 22:** (a) Size distribution by intensity for trial 5 and (b) Size distribution by intensity for trial 12 for chitosan PLGA nanoparticles with miR-140.

The source used for the method achieved smaller, more charged particles with great consistency between each trial, where they altered miRNA concentration from 100 $\mu$ g to 500 $\mu$ g. They had a mean size of 166nm, and a mean zeta potential of +35.3mV.<sup>[107]</sup> The source was also able to achieve a much lower PDI, with a mean value of 0.19. It could be seen from Table 9 that almost all of the samples exhibited very good positive zeta potential, with the exception of samples 4 and 7, which exhibited a very low charge close to one, and sample 13 unexpectedly negative charged. Samples 5 and 12 turned out to be the best in terms of size, in fact they presented a size of 196.4 nm and 151.4 nm, respectively, which was significantly lower than the other samples. Their charge was quite high, with values of 28.6mV and 17mV respectively. In addition, sample 5 showed the smallest value of PDI, which was very important to be able to say that indeed most of the particles in the sample were in the vicinity of the detected peak, with little deviation from the latter.

All the samples with miRNA-34a showed very high surface charge, significantly higher than that with miRNA-140, and less variability. Looking at the Table 9, the best samples were 5 and 7 with a size of 178.8nm and 148.3nm respectively and charge among the highest with 42.0mV for sample 5 and 42.6mV for sample 7. The value of PDI was, in general, acceptable for most of the samples, especially for sample 5 it turned out to be very low with a value of 0.077 while sample 7 had a PDI of 0.245. The optimal parameters thus turned out to be 27500rpm homogenization speed and 75s time of homogenization, since these two parameters were common to both selected best samples 5 and 7. These two parameters were used then for the manufacture of the others three types of designed nanoparticles.

**Table 9:** Characteristics of chitosan PLGA nanospheres with miR-34a, obtained through DLS analysis.

TrialNo.	Mean size (nm)	Size (by intensity) (nm)	Peak percentage(%)	PDI	Zeta Potential (mV)
Control	364.9	435.5 ± 155.0	93.9	0.351	44.4 ± 5.76
1	329.5	415.6 ± 215.0	98.3	0.291	17.9 ± 4.37
2	165.0	187.1 ± 87.02	96.1	0.424	9.86 ± 3.90
3	233.2	283.9 ± 144.3	97.2	0.245	44.3 ± 7.31
4	325.7	429.5 ± 197.0	88.9	0.369	28.6 ± 4.22
5	160.7	178.8 ± 49.87	100.0	0.077	42.0 ± 5.67
6	186.9	246.8 ± 130.4	97.1	0.321	30.6 ± 5.87
7	136.1	148.3 ± 107.3	98.2	0.245	42.6 ± 6.85
8	220.0	231.2 ± 96.10	92.3	0.301	42.9 ± 5.26
9	155.8	191.9 ± 105.2	96.2	0.406	22.5 ± 8.84
10	164.2	204.5 ± 100.2	99.4	0.332	10.8 ± 4.21
11	237.0	258.3 ± 112.9	92.1	0.312	12.6 ± 4.13
12	174.4	263.7 ± 138.1	94.5	0.326	34.3 ± 5.62
13	252.6	327.1 ± 162.0	100.0	0.219	23.8 ± 7.93
Mean	221.85	271.5 ± 128.6	96.0	0.301	29.1 ± 5.71

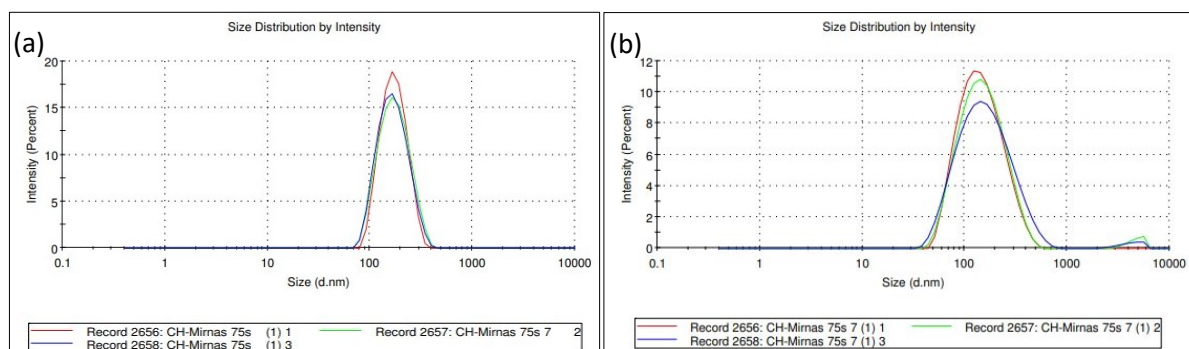


**Figure 23:** (a) Size distribution by intensity for trial 5 and (b) Size distribution by intensity for trial 7 for chitosan PLGA nanoparticles with miR-34a.

The morphology of the nanoparticle with miRNA-140 was shown to be primarily spherical, through TEM analysis, and is in line with what was produced from the source used for the method.<sup>[107]</sup> A schematic of the particle, as well as the TEM images, can be seen in Figure 24.

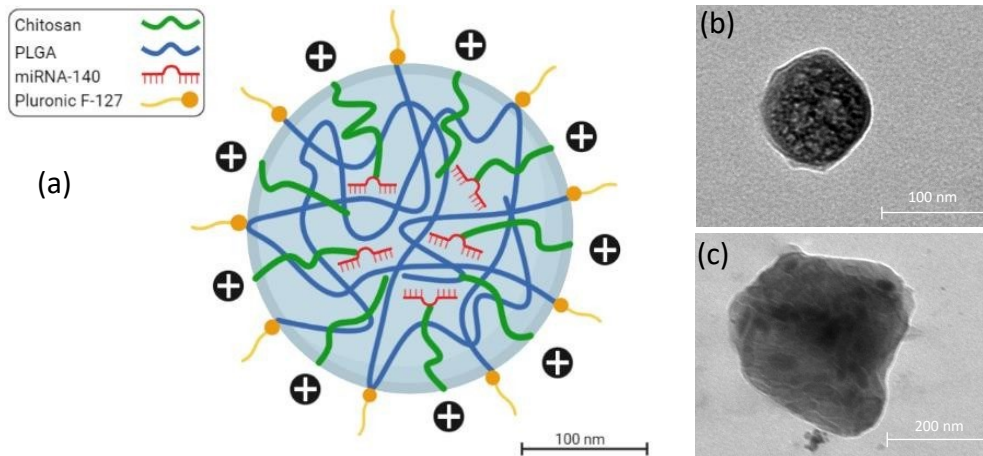


**Figure 24:** (a) schematic of a mean-sized chitosan PLGA nanoparticle, created using BioRender, (b) TEM image of a smaller chitosan PLGA nanoparticle – bar 100nm, and (c) TEM image of a larger chitosan PLGA nanoparticle – bar 200nm.

After analysis on ImageJ, the diameters of the particles in the images were calculated. The particle displayed in Figure 24 (b) was revealed to have a mean diameter of 113.7nm, and the particle displayed in Figure 24 (c) was revealed to have a mean diameter of 372.6nm. Considering Chitosan-PLGA-miR140 NPs, altogether, the size, charge, and PDI were all found to not be in line with the engineering specifications in Table 1 with the particle being larger, less charged, and more diverse than desired. When it is established that the trials were performed for statistical analysis rather than all of them being the optimized values, the results do demonstrate some of the trials satisfying the specifications, namely trials 5 and 6. On the other hand, for Chitosan-PLGA-miR34a NPs, almost all trials seemed to meet the engineering specifications better than those with miR140. The shape produced fulfilled the specification, from TEM analysis revealing it to be a spherical nanoparticle, as well as the method being reproducible, with no complications or difficulties being experienced when carrying out the methods.

The morphology of the miR-NPs, miRDx-NPs, miRDxRs-NPs and LbL-NPs was analyzed through TEM analysis. A schematic of the particles, as well as the TEM images, could be seen in Figure 25 (miR-NPs), Figure 26 (miRDx-NPs), Figure 27 (miRDxRs-NPs) and Figure 28 (LbL-NPs).

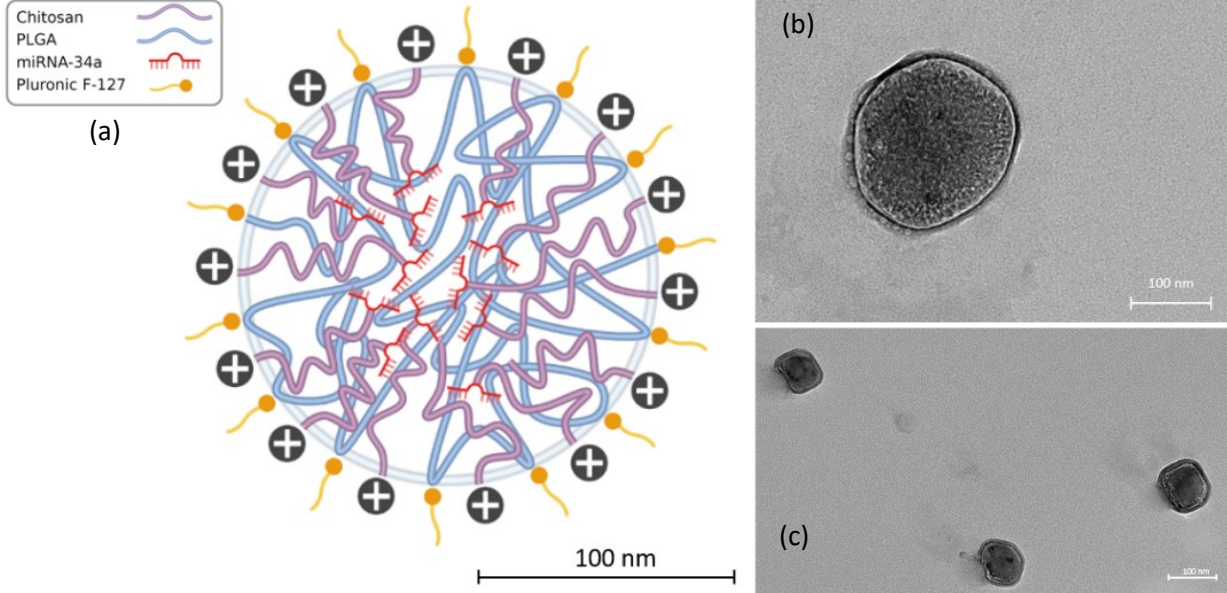


**Figure 25:** (a) schematic of a mean-sized chitosan PLGA miR-34a nanoparticle (miR-NPs), created using BioRender, (b) TEM image of a chitosan PLGA miR-34a nanoparticle – bar 100nm, (c) TEM image of three chitosan PLGA miR-34a nanoparticle – bar 100nm.

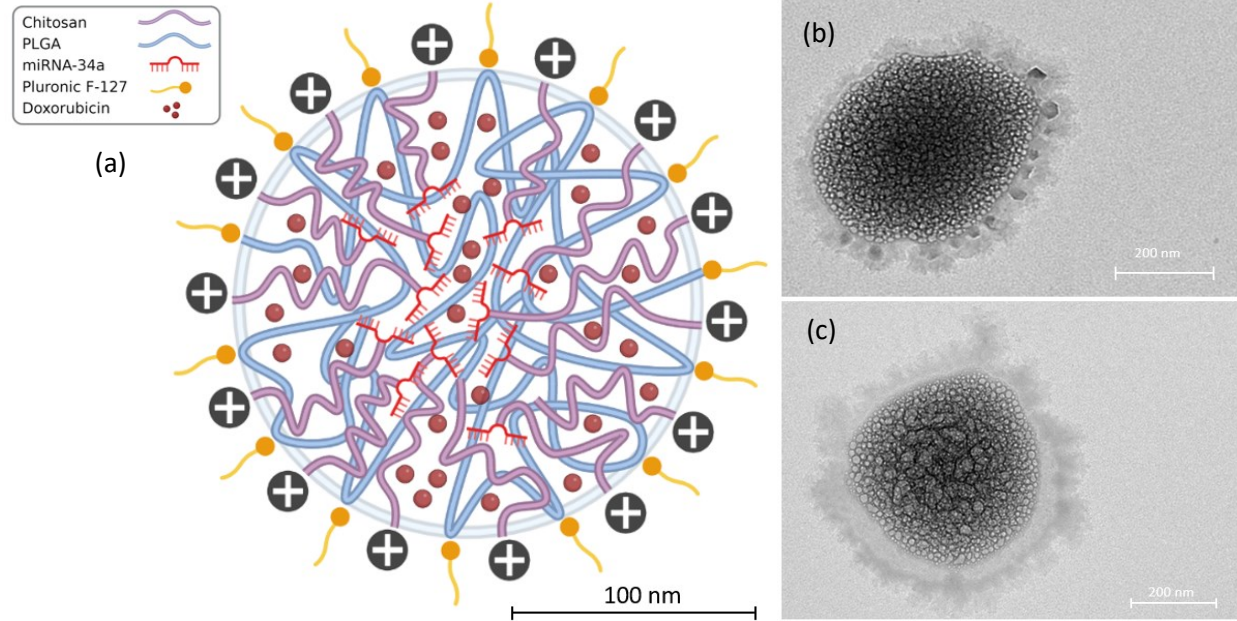


**Figure 26:** (a) schematic of a mean-sized chitosan PLGA miR-34a-Doxo nanoparticle (miRDx-NPs), created using BioRender, (b) TEM image of a chitosan PLGA miR-34a-Doxo nanoparticle – bar 200nm, (c) TEM image of a chitosan PLGA miR-34a-Doxo nanoparticle – bar 200nm

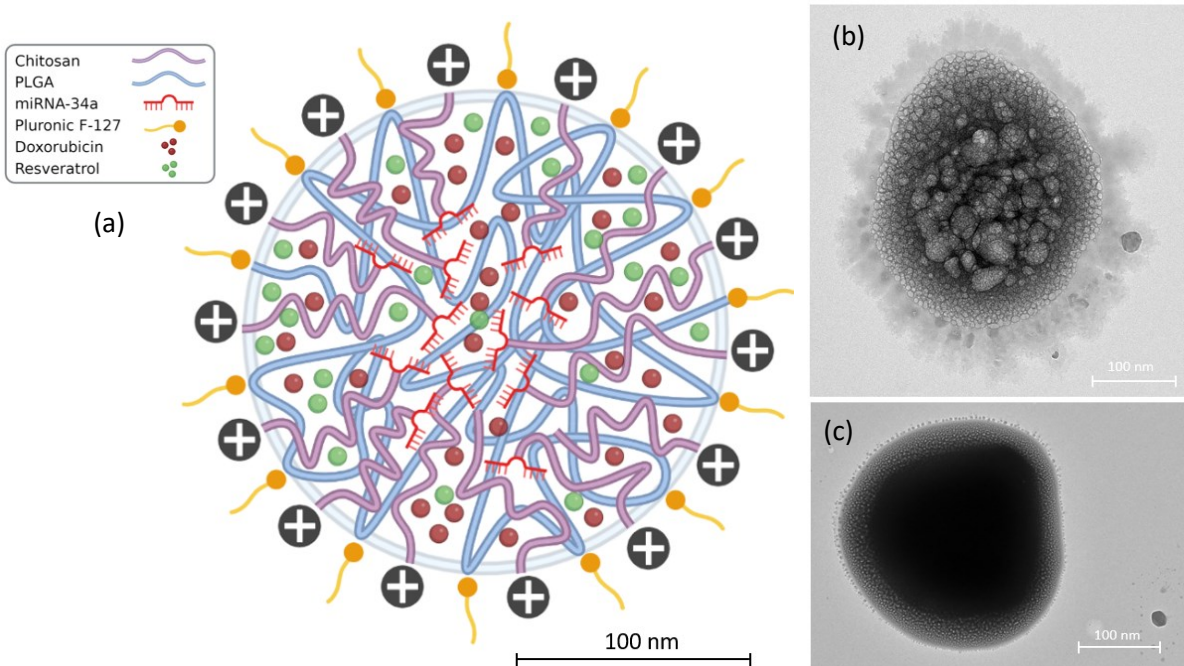


**Figure 27:** (a) schematic of a mean-sized chitosan PLGA miR-34a-Doxo-Resv nanoparticle (miRDxRs-NPs), created using BioRender, (b) TEM image of a chitosan PLGA miR-34a-Doxo-Resv nanoparticle – bar 100nm, (c) TEM image of a chitosan PLGA miR-34a-Doxo-Resv nanoparticle – bar 100nm.

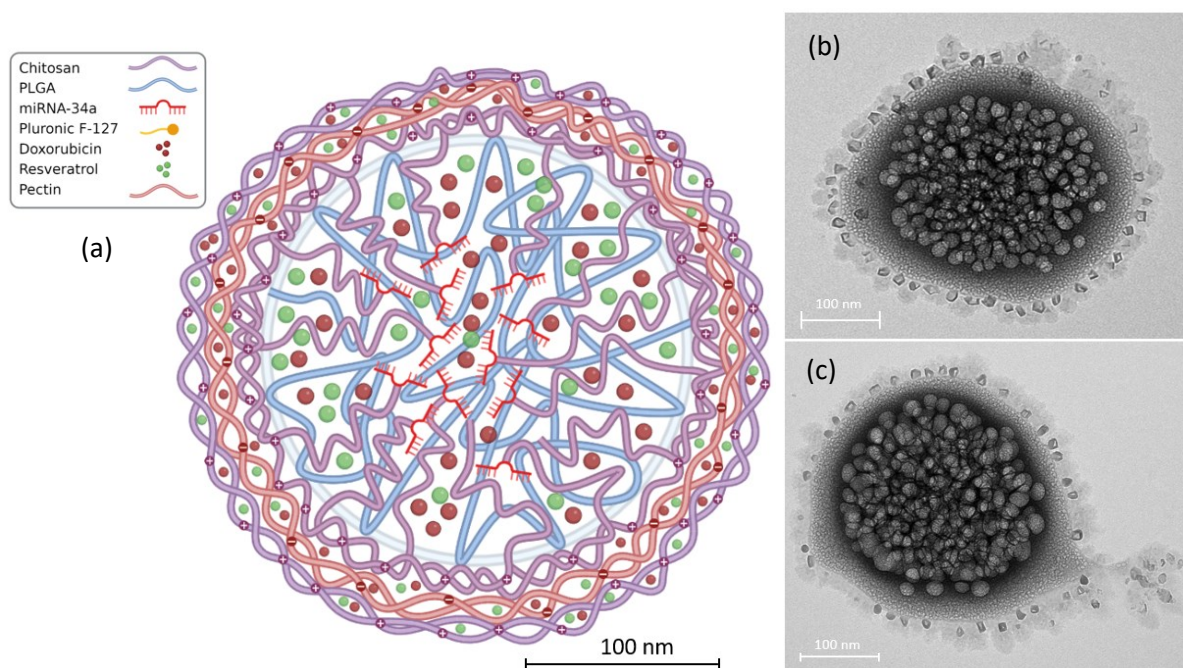


**Figure 28:** (a) schematic of a mean-sized pectin-chitosan layer by layer nanoparticle (LbL-NPs), created using BioRender, (b) TEM image of a pectin-chitosan layer by layer nanoparticle – bar 100nm, (c) TEM image of a pectin-chitosan layer by layer nanoparticle – bar 100nm.

From the reported results, it was observed a larger miR-NP in Figure 25 (b) and three smaller ones in Figure 25 (c) and, measuring their diameter by ImageJ, mean values of 178nm and 101nm were found, respectively. TEM results of miRDx-NPs were shown in Figure 26 (b)(c) and their diameters were analyzed by using ImageJ as well, finding mean values of 251nm and 230nm, respectively. A remarkable different morphology was noticed between miRDx-NPs and miR-NPs, probably due to the presence of the Doxorubicin inside miRDx-NPs, instead absent in miR-NPs. Looking at the TEM results of miRDxRs-NPs in Figure 27, its diameter was compared with that obtained for miRDx-NPs and it was noticed a very little difference, probably attributed to the poor encapsulation of the Resveratrol in the second types, as it was confirmed in section 5.2.3. In Figure 27 (b), a peculiar internal morphology was observed, similar to that of miRDx-NPs, probably because of the presence of the drugs inside the core. Figure 28 (a) showed the schematization of the LbL-NPs and its TEM results in Figure 28 (b) and (c): it was immediately observed a larger size of the core and a circular superficial halos clearly reported outside the surface, that could be the homogeneously arranged forming layers around the core of the nanoparticle. An outermost superficial circular halo was found also in Figure 26 and 27, probably due to the chitosan homogeneously laid around the nanoparticle core.

In Figure 30 was reported a bar chart showing the diameter values of miR, miRDx, miRDxRs-NPs and their schematization, created using BioRender, in Figure 29, as well as for bare miRDxRs and its first and second layer (making LbL-NPs) in Figure 31 and 32. Figure 32(b) showed the zeta potential results obtained from bare miRDxRs-NPs core and the same core covered with the first and second layer, respectively.

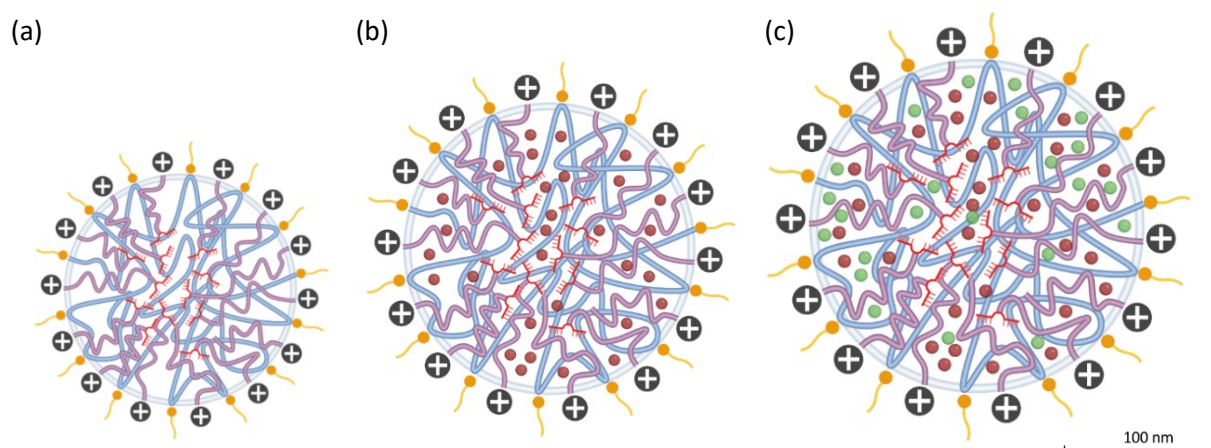


**Figure 29:** Showing the increasing size of the manufactured nanoparticles; (a) schematic of a chitosan-PLGA miR-34a nanoparticle (miR-NPs), (b) schematic of a chitosan-PLGA miR-34a-Doxorubicin nanoparticle (miRDx-NPs), (c) schematic of chitosan-PLGA miR-34a-Doxorubicin-Resveratrol nanoparticle (miRDxRs-NPs), created using BioRender

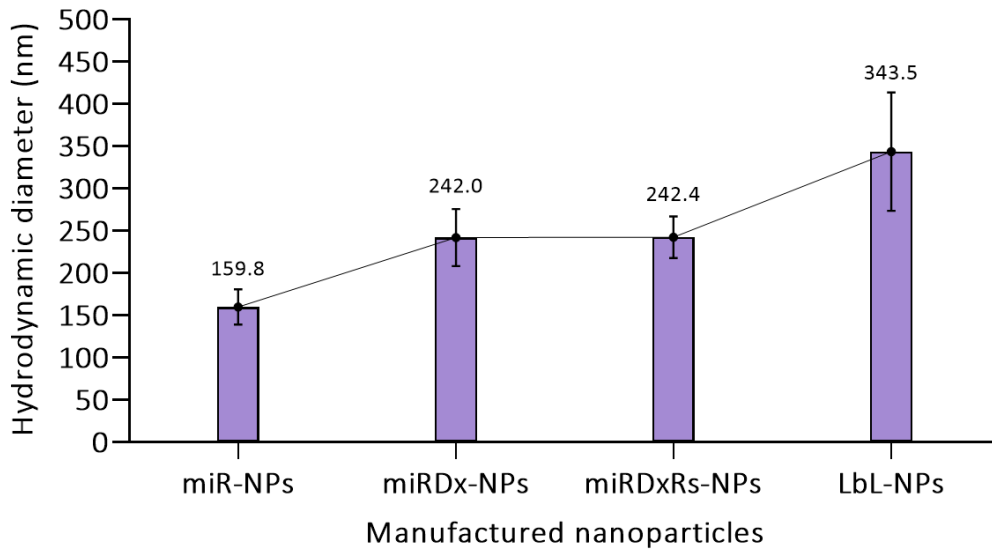


Figure 30: (a) Line graph showing the behavior of the sizes of the manufactured nanoparticles, (b) Bar chart showing the behavior of the sizes of the manufactured nanoparticles, created using GraphPad.

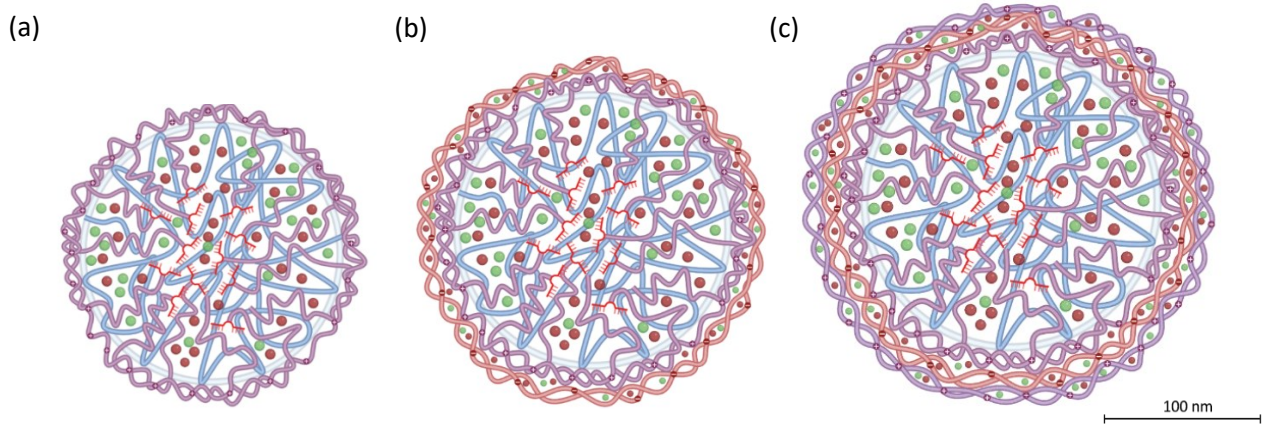


Figure 31: Showing the increasing size of the layer by layer manufactured nanoparticle; (a) schematic of a mean-sized chitosan-PLGA miR34a-Doxo-Resv nanoparticle (miRDxRs-NPs), (b) schematic of a chitosan-PLGA miR34a-Doxo-Resv nanoparticle covered with the first layer of Pectin, (c) schematic of the final nanoparticle with the second layer of Chitosan, final result of the layer by layer technique (LbL-NPs), created using BioRender.

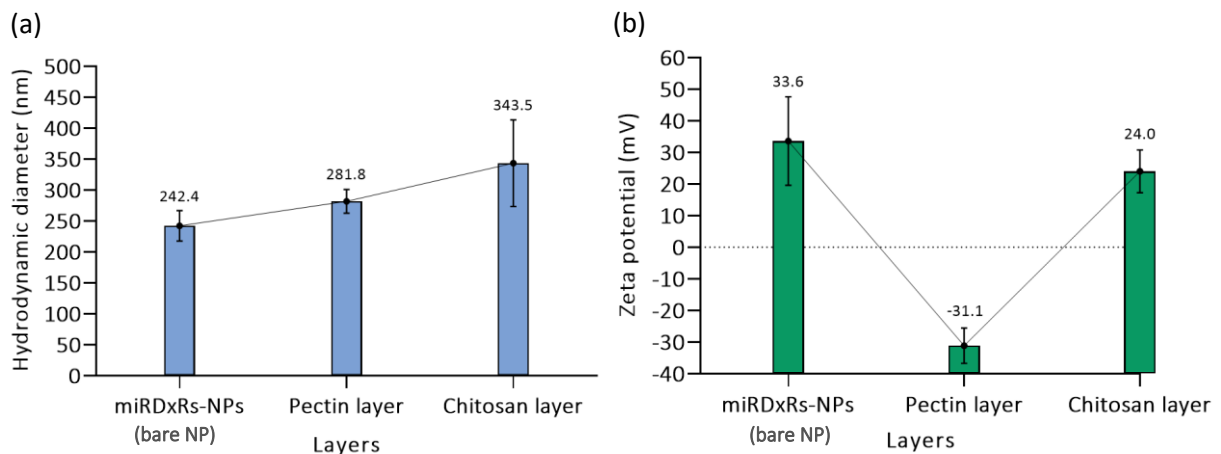


Figure 32: (a) Line graph showing the sizes of the manufactured layer by layer nanoparticle, (b) Line graph showing the charge of the manufactured layer by layer nanoparticle.

From the bar graph in Figure 30 it was noticed an increasing trend of the diameters size of the different types of NPs, as the drug was added, in fact starting with the miR-NPs and adding Doxorubicin, the size increased from 159.87nm to 242nm of the miRDx-NPs. By inserting Resveratrol, obtaining the miRDxRs-NPs, the size did not increase significantly, in fact it seemed to remain roughly equal to that for miRDx-NPs. This could be due to the low Resveratrol encapsulation in the core, as previously mentioned and as reported in section 5.2.3. By creating the two polyelectrolyte layers around the core of the miRDxRs-NPs, the size increased to almost twice the initial size of the miR-nanoparticles. These values were analyzed by ANOVA statistical test in order to understand whether the four diameters were significantly different from each other or whether this difference was due to a variability, within each group, greater than the variability between them. Figure 31 showed the schematization of the LbL nanoparticle, starting with the core of the bare miRDxRs nanoparticle (on the left), coated with the pectin layer (in the middle) and finally coated with chitosan (on the right). Looking at the Figure 32, it was noticed from the two graphs that the sizes and charges changed as a layer was added: the size increased while the charge, as it was expected, changed from the positively charged surface of the miRDxRs-NPs to the negative charge of the pectin layer complexed to the positive surface and then the again positive charge given by the chitosan layer interacted with the pectin surface.

### 5.2.2 Entrapment Efficiency of miR-140

The entrapment efficiency was calculated by looking at the concentration remaining in the supernatant and dividing this by the total concentration in the sample (280ng/μl). These values, as well as the purity values, can be seen in Table 10.

**Table 10:** Entrapment efficiencies of chitosan PLGA nanoparticles, and the purity values of the samples in the NanoDrop.

Trial No.	Entrapment Efficiency (%)	Purity (protein)	Purity (salt)
1 <sup>st</sup> Centrifuge			
5	72.7	-0.04	1.38
6	28.9	3.2	0.75
2 <sup>nd</sup> Centrifuge			
5	73.1	1.09	1.34
6	27.6	0.02	1.41

The results show that in trial 5 a suitable mean value of 72.9% was achieved, meeting the engineering specification. In trial 6, the value was far lower than expected, achieving a value of 28.25% - this did not meet the engineering specification and was not comparable to the source, which achieved exceptional results.<sup>[107]</sup> Chitosan acts as a condensing agent, electrostatically interacting with the miRNA due to their opposing charge. The purity values calculated indicate that in all but the first centrifuge of trial 6 the values were lower than the optimal, indicating a significant number of impurities and contaminated samples. The entrapment efficiency for Chitosan-PLGA-miR140 NPs also fulfilled the specification in one of the samples for those nanoparticles. Given the purity values were predominantly different to the optimal values, it could be assumed that there was an issue in the sample that failed to meet the specifications as it was also not close to the values achieved by the source.<sup>[107]</sup> The factors behind a large portion of the specifications failing to be met have been investigated and could be explained. The differences in the results from the source followed for the method<sup>[107]</sup> were likely based on various contributing factors. One of the most prominent differences was the substitution of Pluronic F-127 in place of poloxamer 188. This material acts as a surfactant; these are amphiphilic molecules<sup>[142]</sup> which help to limit the aggregation of the newly formed nanoparticles as well as playing a role in the eventual sizes of the nanoparticles.<sup>[143]</sup> In one article, different surfactants were investigated for their effects on PLGA nanoparticles; the nanoparticles prepared with poloxamer 188 were found to be smaller than those prepared with an alternative surfactant, Pluronic F-108.<sup>[144]</sup> This demonstrated that the use of Pluronic F-127 in the method would have had a direct effect on the size of the nanoparticle and the aggregation potential, leading to different values of PDI and charge. In this project, it could be assumed it had a negative effect on what was trying to be achieved: the particles created were larger, less charged, and exhibited larger distributions than both the source and the engineering specification. Poloxamer 188 was specifically selected for this, as noted by the source, so the use of Pluronic F-127 may also lead to a difference in

cytotoxicity by exhibiting an inferior or superior ability to preserve cell membranes compared to poloxamer 188. Another difference was the speed of centrifugation; the source stated that the solution was to be centrifuged at 70,000rpm for 1 hour,<sup>[107]</sup> a value that could not be met. Instead, the solution was centrifuged at 13,000rpm for the same period. The centrifugation process was a necessary step to help separate the particles from the remaining solution, a lower speed may have resulted in many of the smaller, and therefore lighter, particles not being involved in the formation of the sediment, and so when the supernatant was removed in preparation for the DLS, some of the particles may have been removed, influencing the results. The particles were also subject to long waiting times between manufacturing and testing which may have influenced the results. In the source, it doesn't state whether there was a delay between the final step of the method and the DLS analysis.<sup>[7]</sup> In this project, there was sometimes 7 days between these steps which may have been the cause of increased aggregation, altering the results output for all characteristics. The final 7 results were subject to this waiting time between production and analysis, and it is evident in the PDI; excluding 13, the PDI values were generally larger than those of the first 6 trials, demonstrating the presence of a larger mass distribution and, therefore, more aggregates having formed in the sample. There were also some anomalies in the tabulated data; in trials 4 and 7, the zeta potential was far lower than expected, and in 13 it was negative. The DLS analysis was performed on a machine called a Zetasizer and special cuvettes were used. Due to the mechanism DLS uses, being light scattering, some issues can arise; the sensitivity of DLS is extremely high, with the light scattered by particles being  $10^6$  the magnitude of its diameter. It often means larger particles will end up suppressing the signals from the smaller ones and, hence, the results will be exaggerated in favour of these, and they may even reveal peaks that do not even exist.<sup>[145]</sup> This could solve why some of the particles had size values far greater than what was expected. Another factor that may have had some influence on the randomness of the data was the homogenizer itself. The homogenizer used was the labGEN 125 (Cole-Parmer LabGEN 125 Homogenizer; 115V) which does not feature a digital display, but rather a slide button with 9 increments between 5,000 and 35,000 rpm. This means that there was sometimes difficulty selecting the required speed quickly, as the process was also timed, which may have led to some trials being performed over the intended level. If the midpoints are to be considered the most consistent results, performing some of these at different levels of speed may have caused the anomalies highlighted.

### 5.2.3 Entrapment Efficiency of miR-34a, Doxorubicin and Resveratrol

The encapsulation values of miRNA, Doxorubicin and Resveratrol for any of the manufactured NPs were shown in the Tables 12-15 and in Figures 33 and 34. Table 12, Table 13 and Figure 33 exhibited their entrapment efficiency (%) while Table 14, Table 15 and Figure 34 reported their entrapped amounts in terms of  $\mu\text{g}$ . First, the amounts of miRNA-34a, Doxorubicin and Resveratrol initially inserted during the manufacturing process of the nanoparticles were shown in Table 11.

**Table 11:** Amounts of miRNA-34a, Doxorubicin and Resveratrol initially inserted during the manufacturing NPs processes

Manufactured NPs	miRNA 34a ( $\mu\text{g}$ )	Doxorubicin ( $\mu\text{g}$ )	Resveratrol ( $\mu\text{g}$ )
miR-NPs	14	-	-
miRDx-NPs	14	10.8	-
miRDxRs- NPs	14	10.8	40.1
layer1°	-	27.1	100.4
layer2°	-	27.1	100.4
LbL-NPs	14	65.0	240.9

MiR-34a and Doxorubicin seemed to be well encapsulated in any of the types of manufactured NPs; the highest entrapment efficiency was found in miR-NPs, where miRNA-34a was the only drug inside, reporting an entrapment efficiency of 80.24%. However, the encapsulation of miRNA-34a looked to be higher than 50% in the other three types of NPs as well. Looking at the entrapment efficiency of the Doxorubicin, the highest values were observed for miRDx-NPs with a percentage of 76.24%. In LbL-NPs, a greater quantity of Doxo was found in the first Pectin layer, probably due to the fact that, since Doxorubicin possessed a slightly positive charge, it was more encapsulated in the negative layer of pectin rather than in the positive chitosan layer. However, even in this case the differences in percentages were not far apart: in the first layer there was 19.91% of Doxo encapsulation while in the second layer 12.98%, with a bigger variability in the first layer. Overall, Resveratrol encapsulation seemed to be very low in both the core of miRDxRs-NPs and the layers of LBL-NPs. Indeed, compared to the amounts of Resveratrol originally encapsulated in the core (40.1  $\mu\text{g}$ ) and in the layers (100.4  $\mu\text{g}$ , respectively in both layers), the entrapped amounts turned out to be very small, reporting 4.16  $\mu\text{g}$  in the core and 12.96  $\mu\text{g}$  in the overall LBL-NPs.

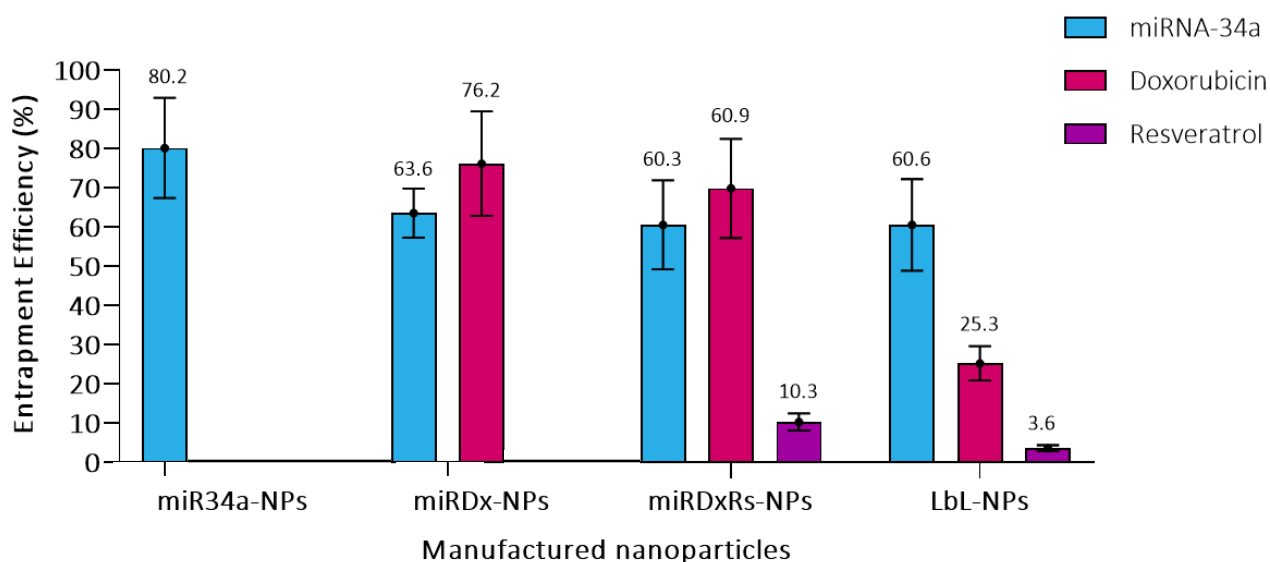


**Figure 33:** Bar graph showing the entrapment efficacy (%) of miRNA-34a in miR-NPs, miRNA-34 and Doxorubicin in miRDx-NPs, miRNA-34a Doxorubicin and Resveratrol in miRDxRs-NPs and all of these in LbL-NPs plus Doxorubin and Resveratrol entrapped in the two forming layer

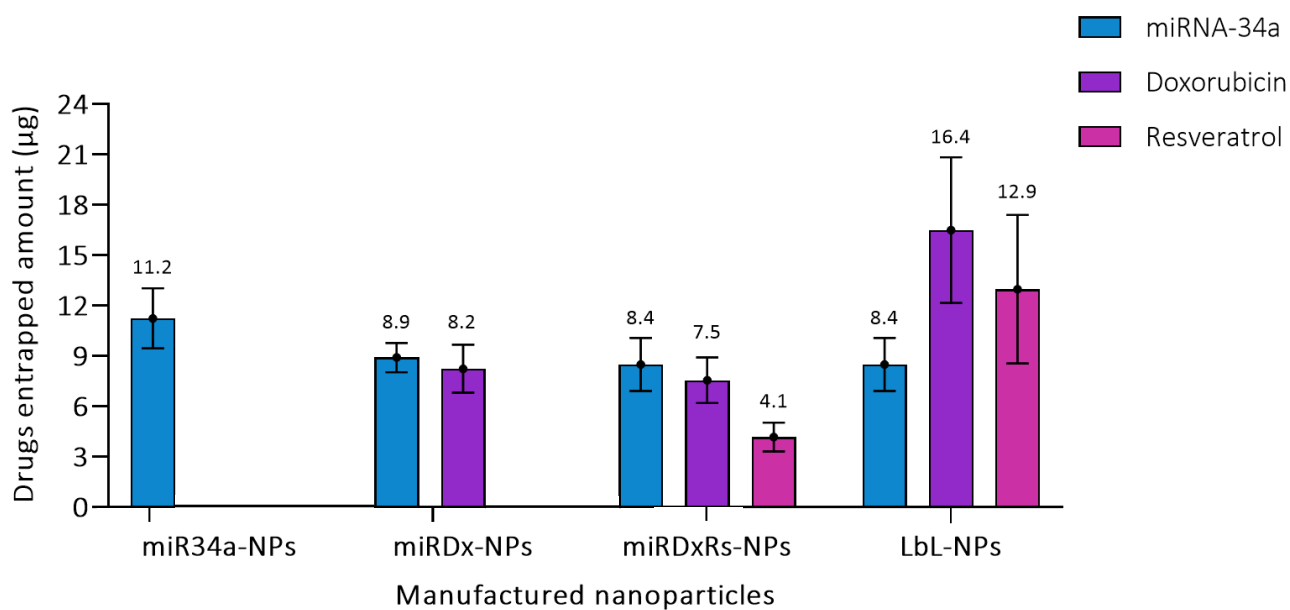


**Figure 34:** Bar graph showing the amount entrapped (µg) of miRNA-34a in miR-NPs, miRNA-34 and Doxorubicin in miRDx-NPs, miRNA-34a Doxorubicin and Resveratrol in miRDxRs-NPs and all of these in LbL-NPs plus Doxorubin and Resveratrol entrapped in the two forming layer.

**Table 12:** Entrapment efficiencies (%) of miR-34a, Doxorubicin and Resveratrol

Manufactured NPs	Size (nm)	Zeta Potential (mV)	miRNA 34a EE (%)	Doxorubicin EE (%)	Resveratrol EE (%)
miR-NPs	159.87 ± 20.91	34.23 ± 2.34	80.24 ± 12.79	-	-
miRDx-NPs	242.00 ± 33.98	35.58 ± 5.33	63.61 ± 6.25	76.24 ± 13.32	-
miRDxRs- NPs	242.40 ± 24.58	33.60 ± 14.02	60.63 ± 11.31	69.95 ± 12.62	10.36 ± 2.16
LbL-NPs	343.55 ± 69.99	24.00 ± 6.79	60.63 ± 11.31	25.31 ± 4.37	3.66 ± 0.76

**Table 13:** Entrapment efficiencies (%) of Doxorubicin and Resveratrol in the two forming layer of LbL nanoparticle.

N° layer	Size (nm)	Zeta Potential (mV)	miRNA 34a EE (%)	Doxorubicin EE (%)	Resveratrol EE (%)
1° Layer (Pectin)	281.87 ± 19.25	-31.10 ± 5.61	-	19.91 ± 7.27	4.14 ± 2.02
2° Layer (Chitosan)	343.55 ± 69.99	24.00 ± 6.79	-	12.98 ± 3.52	4.64 ± 1.53

**Table 14:** Entrapment of miR-34a (µg), Doxorubicin (µg) and Resveratrol (µg).

Manufactured NPs	Size (nm)	Zeta Potential (mV)	miRNA 34a Enc. (µg)	Doxorubicin Enc. (µg)	Resveratrol Enc. (µg)
miR-NPs	159.87 ± 20.91	34.23 ± 2.34	11.23 ± 1.79	-	-
miRDx-NPs	242.00 ± 33.98	35.58 ± 5.33	8.90 ± 0.87	8.23 ± 1.43	-
miRDxRs- NPs	242.40 ± 24.58	33.60 ± 14.02	8.48 ± 1.58	7.55 ± 1.36	4.16 ± 0.86
LbL-NPs	343.55 ± 69.99	24.00 ± 6.79	8.48 ± 1.58	16.49 ± 4.33	12.96 ± 4.42

**Table 15:** Entrapment of Doxorubicin (µg) and Resveratrol (µg) in the two forming layer of LbL NP.

N° layer	Size (nm)	Zeta Potential (mV)	miRNA 34a Enc. (µg)	Doxorubicin Enc. (µg)	Resveratrol Enc. (µg)
1° Layer (Pectin)	281.87 ± 19.25	-31.10 ± 5.61	-	5.41 ± 2.10	4.14 ± 2.02
2° Layer (Chitosan)	343.55 ± 69.99	24.00 ± 6.79	-	3.52 ± 0.86	4.64 ± 1.53

#### 5.2.4 Release of miR-34a, Doxorubicin and Resveratrol

To evaluate the release of miR-34a, Doxorubicin and Resveratrol from the manufactured NPs, the nanoparticles were incubated at 37°C in PBS at pH 7.4, mimicking storage and blood plasma conditions, and analyzing their releases following the method previously described. Figure 35-38 showed their cumulative release over a period of 6 days. Looking at the cumulative release of miR-34a from miR-NPs, in Figure 35, it could be noticed that from the originally entrapped amount (11.23 µg), approximately 70% of the total miR-34a cargo was released within 2 days. This consideration was very similar to the miR-34a release from miRDx-NPs and miRDxRs-NPs showed in Figure 36 and 37. Looking at the cumulative release of the Doxorubicin from miRDx-NPs and miRDxRs-NPs, approximately 70% of the total entrapped amount (8.23 µg for miRDx-NPs and 7.55 µg for miRDxRs-NPs) was released within 2 days and almost 45% was released within 5 hours from the incubation. In LbL-NPs miR-34a release turned out to be slower compared to the other NPs and there was not a gradual and regular release of Doxorubicin and Resveratrol, in fact almost 40% of their total amount was released within 10 minutes, followed by a bigger drastic increase after 24h of incubation, plateaued until the end of the evaluation time point (6 days). This consideration could be due to the presence of the two superficial layers on the surface of the nanoparticle, which have two different times of degradation, that could prevent a gradual e regular release, leading to a sudden and consistent release of the drugs once each layer was degraded. For this reason, miRNA and the drugs could then find more difficult to leave the nanostructure. It was realized that these conditions of incubation in PBS did not perfectly mimic physiological or intracellular environments (pH 5.5 for mimicking endolysosomal conditions), and that future studies should be performed to investigate miR-34a and drugs release in serum and under conditions representing in vivo mixing. However, these studies did provide valuable information regarding the release profile of miR-34a, Doxo and Resv from the manufactured NPs under extracellular pH conditions.

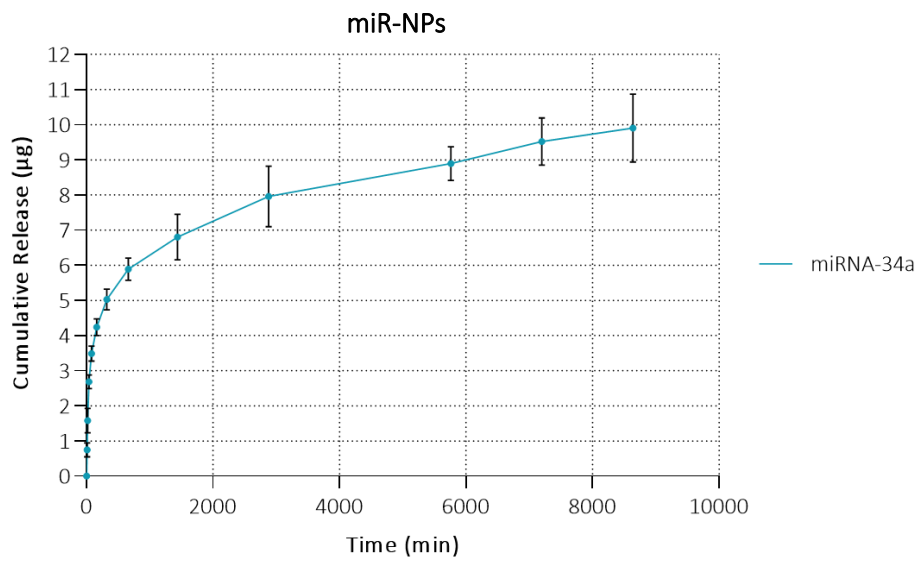


Figure 35: Cumulative release ( $\mu\text{g}$ ) of miRNA-34a from miR-NPs.

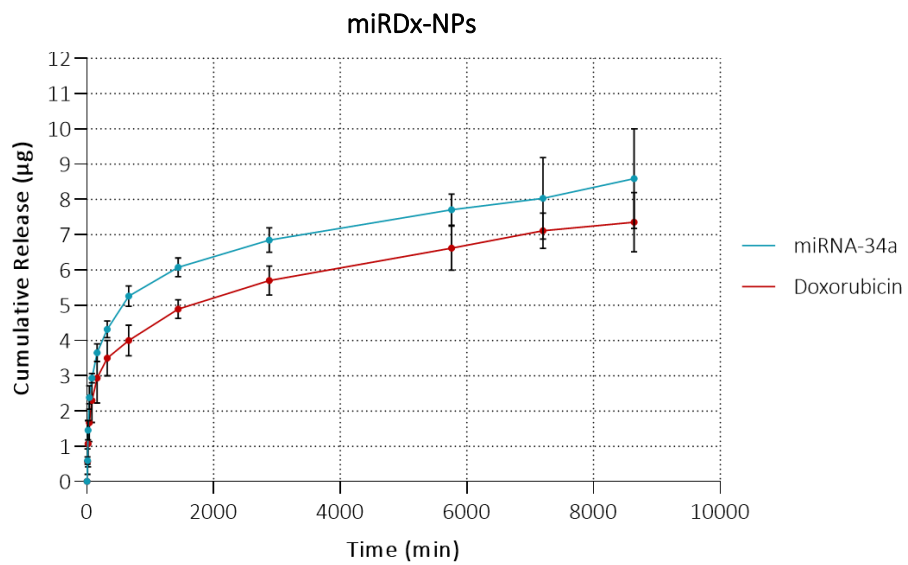


Figure 36: Cumulative release ( $\mu\text{g}$ ) of miRNA-34a and Doxorubicin from miRDx-NPs.

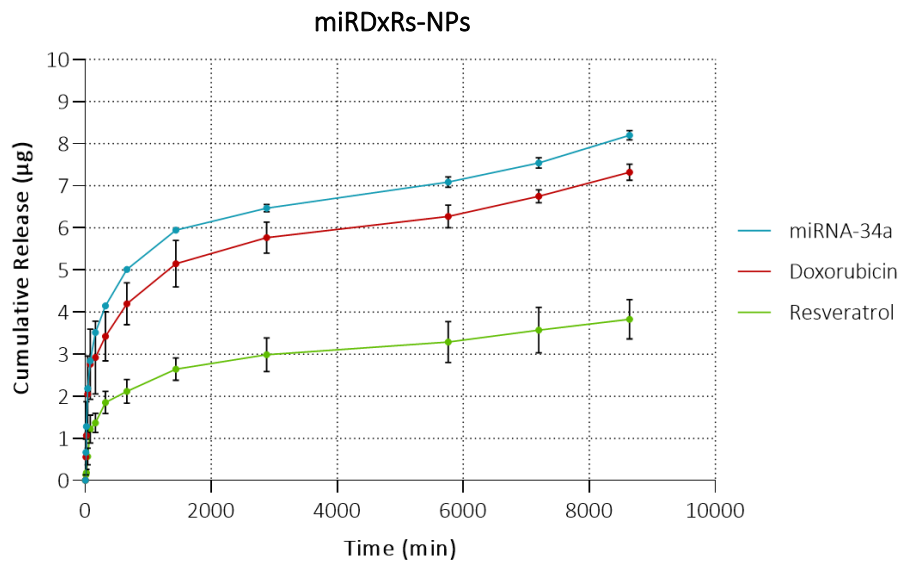


Figure 37: Cumulative release ( $\mu\text{g}$ ) of miRNA-34a, Doxorubicin and Resveratrol from miRDxRs-NPs

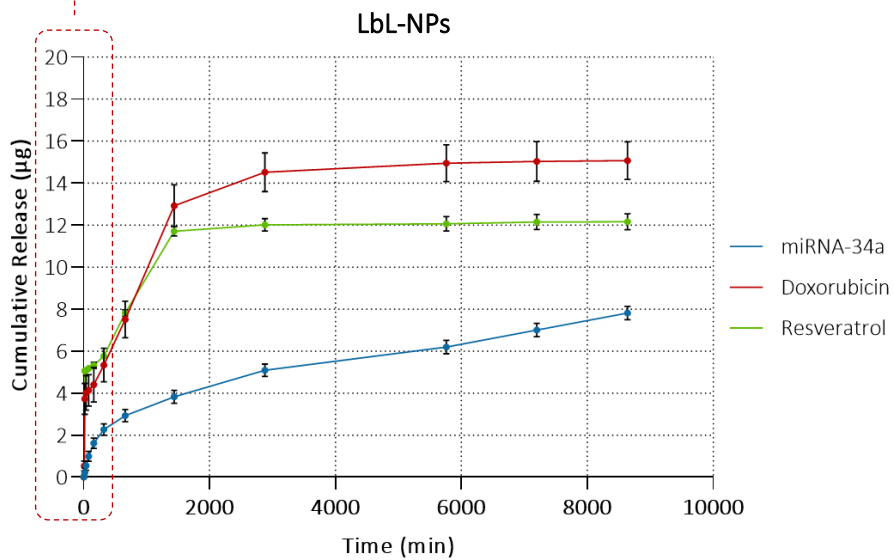
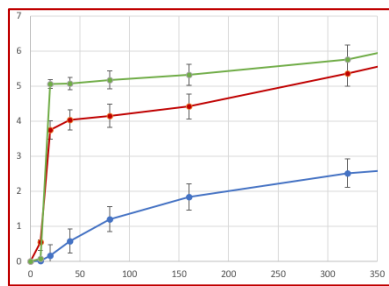
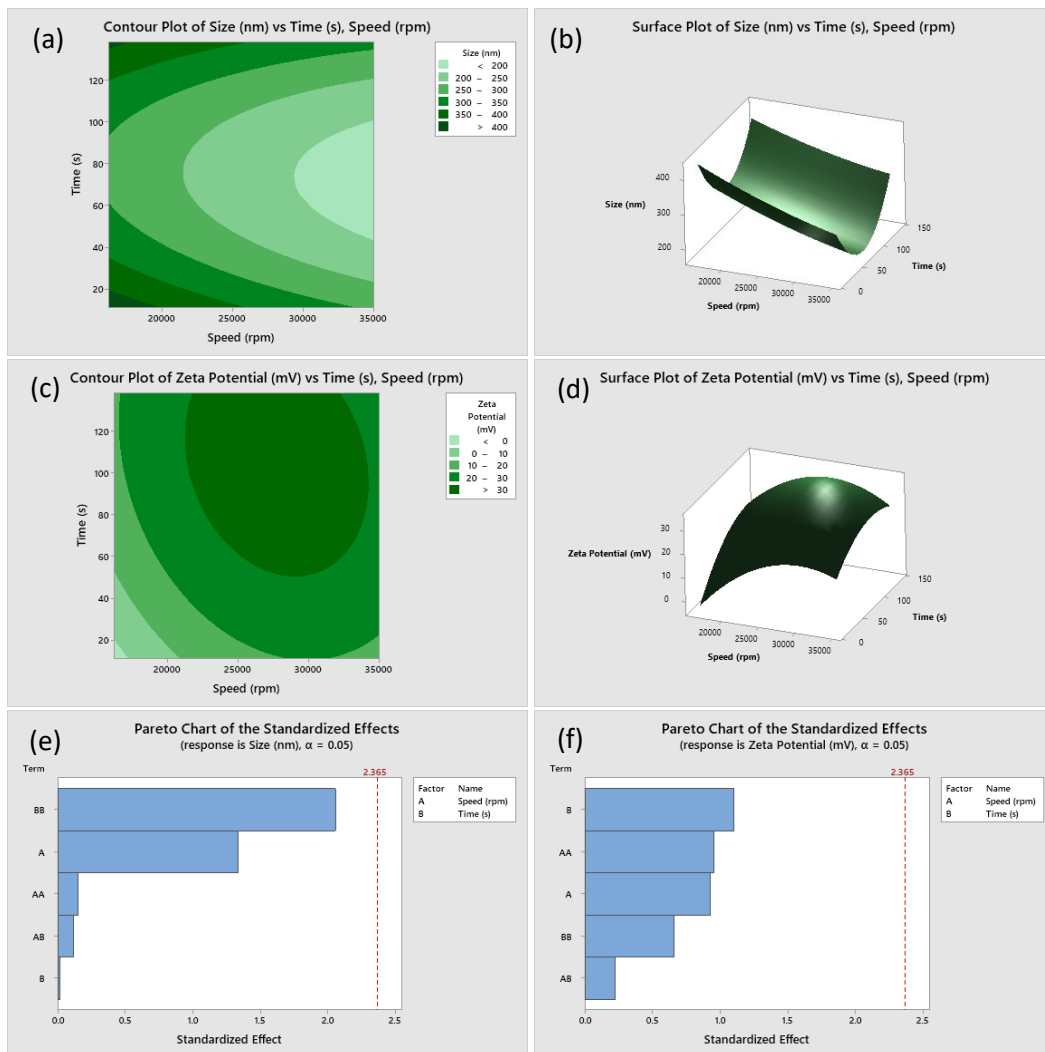


Figure 38: Cumulative release ( $\mu\text{g}$ ) of miRNA-34a, Doxorubicin and Resveratrol from LbL-NPs.

## 5.3 NPs Statistical Results

### 5.3.1 Chitosan-PLGA miRNA34a NPs

The parameters varied in each trial could be seen in Table 4. Using Minitab, the results were input, and statistical analysis was performed to evaluate whether either parameter was statistically significant in influencing the size and/or charge of the nanoparticle. Contour and surface plots of the results against the parameters could be seen in Figure 39 (a, c, e, f), as well as Pareto charts – these display how close each parameter, or a combination of each, was to being statistically significant – Figure 39 (b, d).



**Figure 39:** (a) Contour plot of Size (nm) against Speed (rpm) and Time (s), (b) Surface plot of Size (nm) against Speed (rpm) and Time (s), (c) Contour plot of the Zeta Potential (mV) against Speed (rpm) and Time (s), (d) Surface plot of Zeta Potential (mV) against Speed (rpm) and Time (s), (e) Pareto charts for Size (nm), showing the alpha value and the standardised effect of each parameter on the resulting size of the particle, (f) Pareto charts for Zeta Potential (mV), showing the alpha value and the standardised effect of each parameter on the resulting zeta potential of the particle. All created on Minitab.

Based on the Pareto charts, no parameter exceeded the alpha value and, therefore, they were not significant in influencing the size or zeta potential of the nanoparticle. The surface plots and tabulated results indicate that, although satisfactory results were achieved at certain combinations, there was little to no pattern, prohibiting accurate predictions of either characteristic. From the contour plots of the zeta potential, it could be seen a most comfortable region for about 24000-34000rpm interval of speed and 60-130s as interval of time of homogenization, region where the highest negative values of zeta potential didn't change. Looking at the contour plots of Size, it could be seen a most comfortable region over 30000rpm for speed and 60-90s as interval of time of homogenization, region where the lowest size could be reached. The full statistical results can be found in the appendix, section 9.1.

### 5.3.2 ANOVA – The four manufactured NPs

Statistical analysis, by using one-way ANOVA method, was done on the results obtained in terms of size and cumulative release in order to understand whether there was indeed statistically significant difference between the various groups in terms of size and releases or whether this difference was due to the fact that the variability within each group was greater than the variability between them and thus lead to numerically different but not statistically significant values. ANOVA one-way tested the hypothesis that the averages of the populations were equal (t-test extension) and tells whether there were statistically significant differences between them. It compares mean values in pair, formulating an hypothesis  $H_0$  of equality between them and, for a p-value lower than the threshold value (0.05), the hypothesis  $H_0$  can be rejected. ANOVA analysis require basic assumptions in order to be used: normal distribution of residues, sampling them as randomly as possible, and homogeneity of variance of the data sampled. First of all the residuals plots were presented, allowing to understand if it made sense to do the ANOVA, because the residuals must had normal distribution in the histogram plot, there had to be no trend over time in the versus order plot, they must followed the normal probability plot line and there had to be uniform distribution around 0 in the versus fits plot.

#### Size on overall NPs

Figure 40 showed the residueals plots where it could be seen that the data had no normal distribution in the Histogram plot, there were no trends over time in the versus order plot and they homogenously followed the line in the Normal Probability plot.

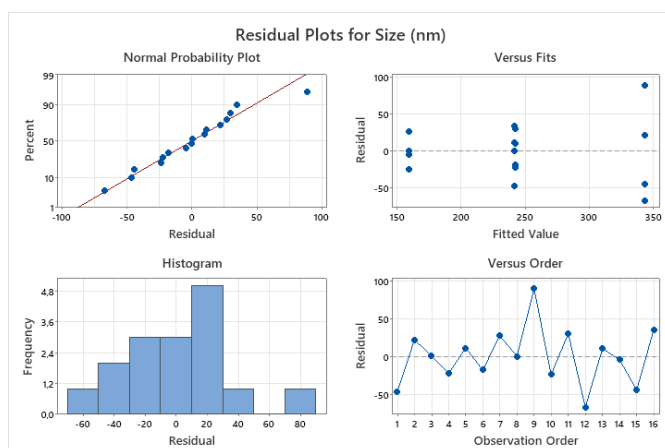


Figure 40: Residual plot, created using Minitab.

Figure 41 (a) exhibited the interval plot in which all the midpoints were plotted with together the standard deviation of each group, while Figure 42 (b) presented the individual plot in which the mean but also the respective points were represented, thus observing where they were placed and whether there may were outliers.

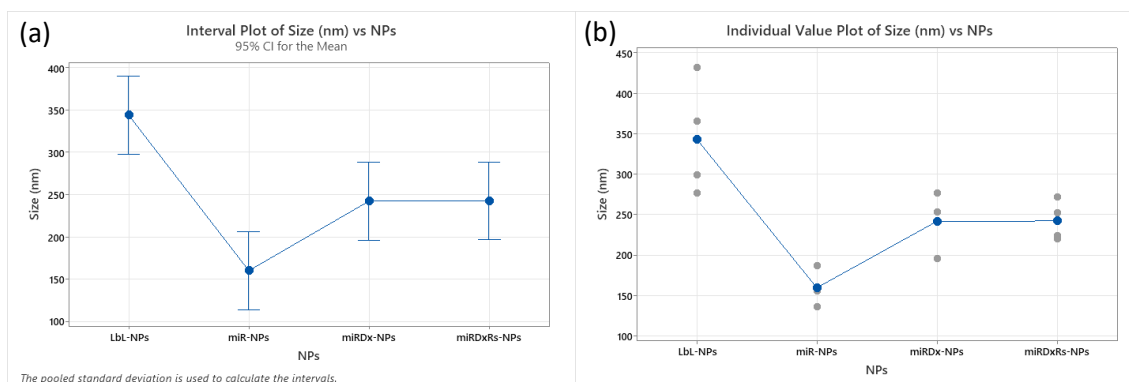


Figure 41: (a) Interval Plot of Size (nm) vs NPs, (b) Individual Value Plot of Size (nm) vs NPs, creating using ANOVA one-way in Minitab.

The results of the ANOVA test were shown in Table 18, where the 95% confidence level intervals were all reported. The p-value obtained was less than 0.05% (alpha value) which meant that some comparisons of mean of groups could be statistically different. If the 95%CI intervals had no overlap, it meant that there was a statistically significant difference between the averages of the two groups, otherwise it was not possible to confirm that. From Table 16, it could be seen that LbL-NPs particles had no numerical overlap with all other NPs, different was the case with miRDx-NPs and miRDxRs-NPs, which thus seemed to have no difference between their averages, given the high numerical overlap between the two groups. The concept was investigated through Tukey's comparison, Tukey Pairwise Comparisons. From the results obtained in Table 17 and Figure 42 it could be seen that only the differences with LbL-NPs were statistically different as they did not share letters, furthermore

confirmed that by the p-values of the combinations with LbL-NPs that were lower than alpha-value, looked at the Table 18, in concert with no presence of 0 value in their intervals.

**Table 16:** ANOVA one-way analysis on Size measurement of the different four manufactured NPs.

Manufactured NPs	Size mean (nm)	StDev (mV)	95% CI
LbL-NPs	343.5	70.0	(297.7; 389.4)
miRDxRs-NPs	159.9	20.9	(114.0; 205.8)
miRDx-NPs	242.0	34.0	(196.1; 287.9)
miR-NPs	242.4	24.6	(196.5; 288.3)

**Table 17:** Grouping Information Using the Tukey Method and 95% Confidence, Size measurement of the different four manufactured NPs

Manufactured NPs	Mean (nm)	Grouping
LbL-NPs	343.5	A
miRDxRs-NPs	242.4	B
miRDx-NPs	242.0	B
miR-NPs	159.9	B

**Table 18:** Tukey Simultaneous Tests for Differences of Means, on Size measurement of the different four manufactured NPs

Difference of Levels	Difference of Means	SE of Difference	95% CI	T-Value	Adjusted P-Value
miR-NPs - LbL-NPs	-183.7	29.8	(-272.1; -95.2)	-6.17	0.000
miRDx-NPs - LbL-NPs	-101.5	29.8	(-190.0; -13.1)	-3.41	0.023
miRDxRs-NPs - LbL-NPs	-101.1	29.8	(-189.6; -12.7)	-3.40	0.024
miRDx-NPs - miR-NPs	82.1	29.8	(-6.3; 170.6)	2.76	0.072
miRDxRs-NPs - miR-NPs	82.5	29.8	(-5.9; 171.0)	2.77	0.070
miRDxRs-NPs - miRDx-NPs	0.4	29.8	(-88.0; 88.8)	0.01	1.000

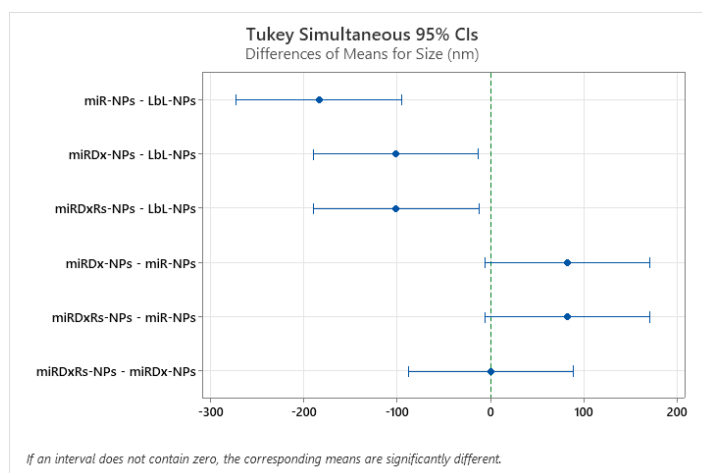


**Figure 42:** Tukey Simultaneous 95% CIs on Size measurement of the different four manufactured NPs.

### Size on Layer-by-Layer NPs

Figure 43 showed the residues plots where it could be seen that the data had no normal distribution in the Histogram plot, there were no trends over time in the versus order plot follow the line in the Normal Probability plot.

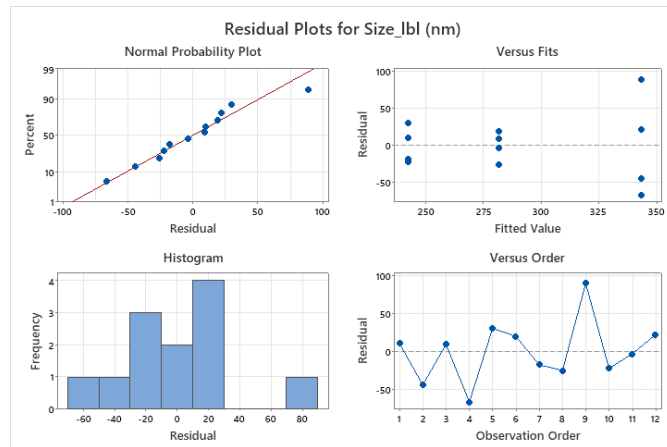


Figure 43: Residual plot, created using Minitab

Figure 44 (a) exhibited the interval plot in which all the midpoints are plotted with together the standard deviation of each group, while Figure 44 (b) presented the individual plot in which the mean but also the respective points were represented, thus observing where they were placed and whether there may were outliers.

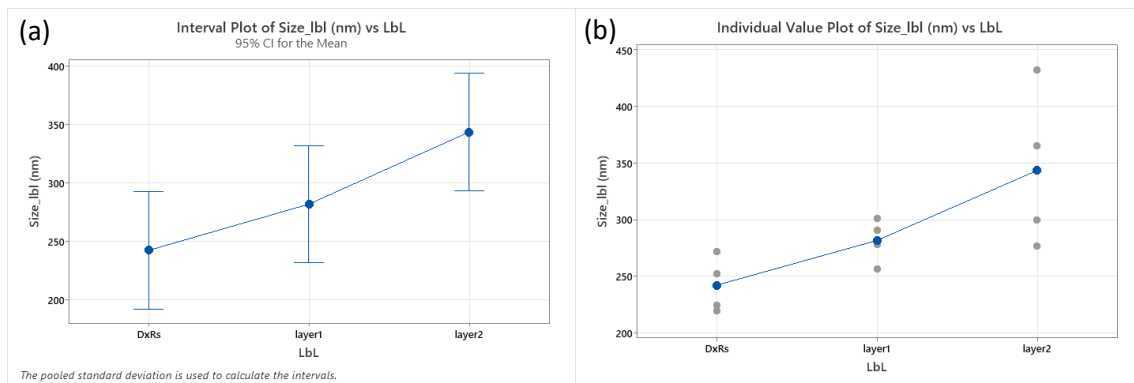


Figure 44: (a) Interval Plot of Size (nm) vs LbL, (b) Individual Value Plot of Size (nm) vs LbL, creating using ANOVA one-way in Minitab.

The results of the ANOVA test were shown in Table 19, in which the 95% confidence level intervals were presented. The p-value obtained was 0.03, lower than 0.05% (alpha value). From 95%CI interval in Table 19, It could be seen that the bare miRDxRs-NPs were overlapped with the size of the nanoparticles composed with the same core plus the first layer of pectin, while there was no overlap with the final nanoparticle coated also with the second layer of chitosan. The concept was investigated through Tukey Pairwise Comparisons and, from the results obtained in Table 20 and Figure 45, it was seen that the first layer NPs shared the same letter with the bare NPs and the final NPs, so there was

no significance difference between them. This was confirmed ulteriorly by the p-values, showed in Table 21, of the different levels in combination with the first layer NPs, which presented a p-value bigger than 0.05. The concept was again supported by the presence of 0 value in their 95%CI intervals, showed in Table 21.

**Table 19:** ANOVA one-way analysis on Size measurement from the bare miRDxRs-NPs, miRDxRs-NPs with pectina layer (1° layer) and miRDxRs-NPs with Chitosan layer (2° layer).

Manufactured NPs	Size mean (nm)	StDev (mV)	95% CI
miRDxRs-NPs	242.4	24.6	(192.3; 292.5)
layer1	281.8	19.2	(231.8; 331.9)
layer2	343.5	70.0	(293.5; 393.6)

**Table 20:** Grouping Information Using the Tukey Method and 95% Confidence.

Manufactured NPs	Mean (nm)	Grouping
layer2	343.5	A
layer1	281.8	A B
miRDxRs-NPs	242.4	B

**Table 21:** Tukey Simultaneous Tests for the bare miRDxRs-NPs, miRDxRs-NPs with pectina layer (1° layer) and miRDxRs-NPs with Chitosan layer (2° layer).

Difference of Levels	Difference of Means	SE of Difference	95% CI	T-Value	Adjusted P-Value
layer1 - miRDxRs-NPs	39,5	31,3	(-47,9; 126,9)	1.26	0.450
layer2 - miRDxRs-NPs	101,1	31,3	(13,8; 188,5)	3.23	0.025
layer2 - layer1	61,7	31,3	(-25,7; 149,1)	1.97	0.175

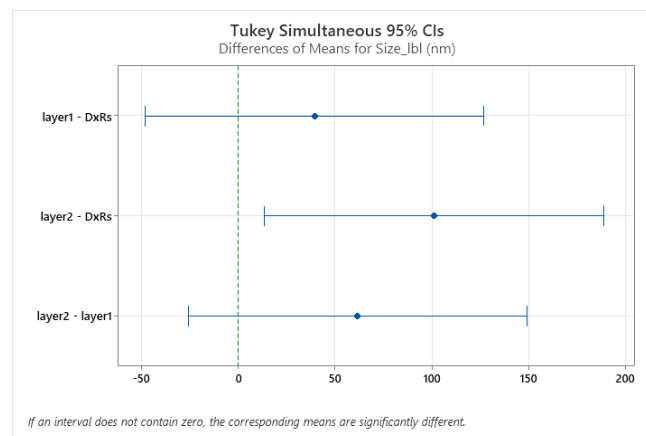


**Figure 45:** Tukey Simultaneous 95% CIs on Size measurement of the bare miRDxRs-NPs, miRDxRs-NPs with pectina layer (1° layer) and miRDxRs-NPs with Chitosan layer (2° layer).

### Cumulative Release

By one-way ANOVA statistical test with Tukey comparison, it was evaluated the final two time points of release of the drugs in order to understand whether a final release plateau was present or not. If there was a release plateau, it would mean that the averages of the end points were not statistically different from each other, so the release between the two time points could not be considered statistically different which means that the drug was released completely in the earlier time points. The results were shown in Table 22 and Table 23. The mean, standard deviation and corresponding 95% confidence intervals were shown in Table 22, from which we could understand whether, for each analyzed pair, there was overlap of the intervals and therefore no significant difference. In Table 23 the comparison was made, for each pair of points, and the confidence interval and p-value were identified. It was immediately noticed that only three of the 9 analyzed pairs of points presented a p-value less than 0.05, and these concerned miRNA-34a and Doxorubicin from miRDxRs-NPs release and miRNA-34th release from LbL-NPs. In fact, these pairs were the only ones with a confidence interval in which the numerical value 0 was not present, as could also be confirmed by Figure 46 in which the Tukey simultaneous plots were depicted. Thus, it could be deduced that only for these three pairs of values it was possible to confirm a statistically significant difference between the averages of the values at time point 7200 min and 8640 min, so no release plateau was present. Instead, in all other cases it was impossible to come up with this consideration, not being able to reject the hypothesis of equality

**Table 22:** ANOVA one-way analysis on cumulative release of the last two time points of the analyzed nine cumulative releases

NPs release	TP (min)	Mean	StDev	95% CI
miRNA-34a from miRNPs	7200	9.518	0.671	(8.184; 10.851)
	8640	9.904	0.966	(8.570; 11.237)
miRNA-34a from miRDxNPs	7200	8.027	1.158	(5.956; 10.099)
	8640	8.593	1.414	(6.522; 10.665)
Doxorubicin from miRDxNPs	7200	7.111	0.500	(6.003; 8.218)
	8640	7.353	0.839	(6.246; 8.460)
miRNA-34a from miRDxRsNPs	7200	7.544	0.125	(7.351; 7.737)
	8640	8.196	0.114	(8.003; 8.389)
Doxorubicin from miRDxRsNPs	7200	6.747	0.152	(6.471; 7.024)
	8640	7.320	0.190	(7.044; 7.597)
Resveratrol from miRDxRsNPs	7200	3.568	0.543	(2.757; 4.379)
	8640	3.827	0.466	(3.016; 4.638)
miRNA-34a from LbLNPs	7200	7.005	0.320	(6.490; 7.520)
	8640	7.809	0.323	(7.294; 8.324)
Doxo from LbLNPs	7200	15.035	0.948	(13.555; 16.515)
	8640	15.065	0.898	(13.585; 16.545)
Resv from LbLNPs	7200	12.144	0.357	(11.544; 12.745)
	8640	12.156	0.392	(11.555; 12.756)

**Table 23:** Tukey Simultaneous Tests for cumulative release of the last two time points of the analyzed nine cumulative releases.

NPs release	Difference of Levels	Difference of Means	SE of Difference	95% CI	T-Value	Adjusted P-Value
miRNA-34a from miRNPs	8640 - 7200	0.386	0.679	(-1.500; 2.271)	0.57	0.600
miRNA-34a from miRDxNPs	8640 - 7200	0.570	1.060	(-2.360; 3.500)	0.54	0.620
Doxorubicin from miRDxNPs	8640 - 7200	0.242	0.564	(-1.323; 1.808)	0.43	0.690
miRNA-34a from miRDxRsNPs	8640 - 7200	0.651	0.098	(0.379; 0.924)	6.64	0.003
Doxorubicin from miRDxRsNPs	8640 - 7200	0.573	0.141	(0.182; 0.964)	4.07	0.015
Resveratrol from miRDxRsNPs	8640 - 7200	0.259	0.413	(-0.888; 1.406)	0.63	0.564
miRNA-34a from LbLNPs	8640 - 7200	0.804	0.262	(0.076; 1.533)	3.06	0.038
Doxo from LbLNPs	8640 - 7200	0.030	0.754	(-2.064; 2.123)	0.04	0.971
Resv from LbLNPs	8640 - 7200	0.011	0.306	(-0.838; 0.861)	0.04	0.972

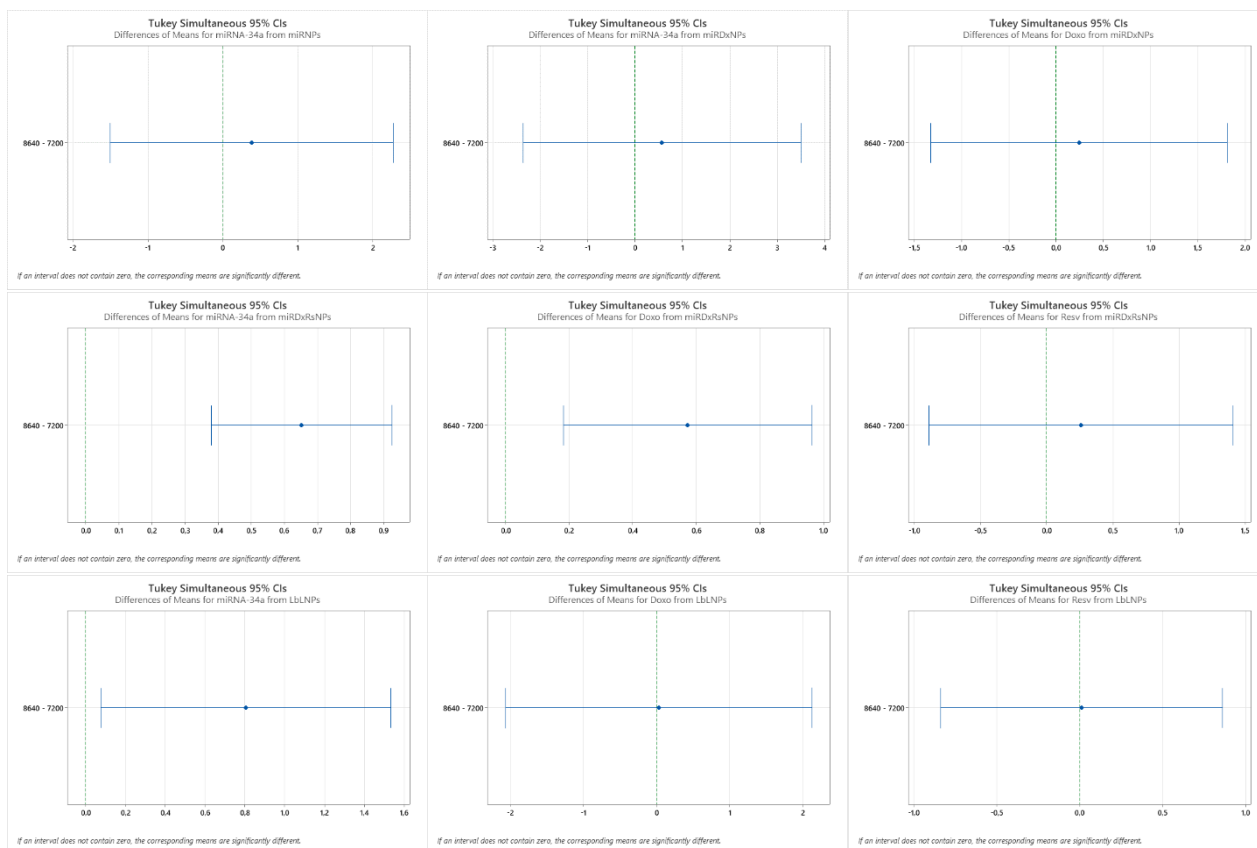


**Figure 46:** Tukey Simultaneous 95% CIs on cumulative release of the last two time points of the analyzed nine cumulative releases.

## 5.4 Morphological characterization of Sarcospheres

SaoS-2 and U2OS were chosen as Osteosarcoma cells to create the spheroids<sup>[124][125]</sup>. Figure 47 showed the U2OS and SaoS-2 cells in 2D culture at day 7 and in spheroids models at 6 and 15 days of culture.

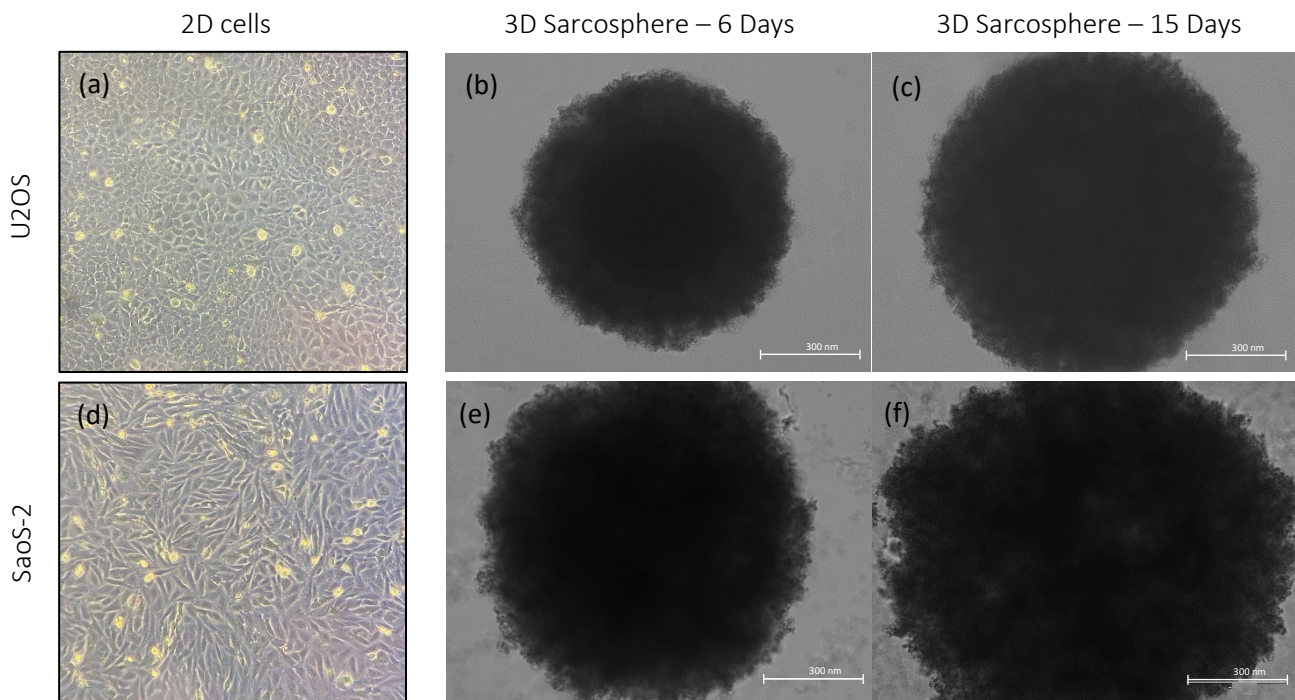


**Figure 47:** (a) Bidimensional U2OS cell culture at 7 days of culture, (b) U2OS Sarcosphere at 6 days, (c) U2OS Sarcosphere at 15 days of culture, (d) Bidimensional SaoS-2 cell culture at 7 days of culture, (e) SaoS-2 Sarcosphere at 6 days, (f) SaoS-2 Sarcosphere at 15 days of culture.

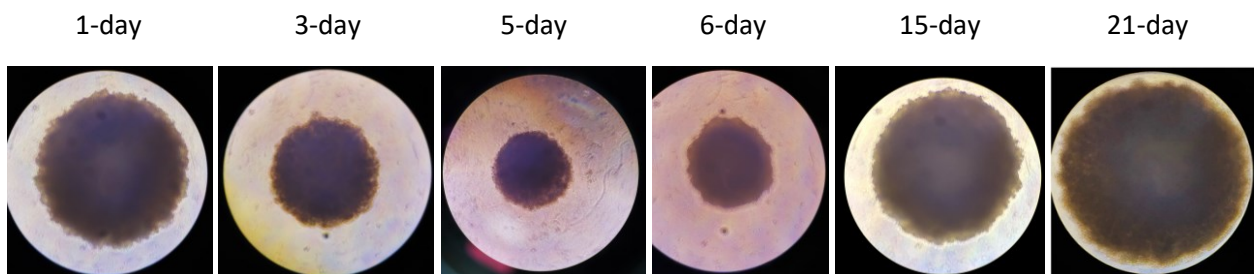


**Figure 48:** U2OS Sarcospheres over time.

Figure 49 and 50 show the trend of spheroids size over a 21-day period with U2OS and SaoS-2 cells respectively. The trend seemed similar for both SaoS-2 and U2OS spheroids<sup>[125][140][141]</sup>. In fact, starting at 24h with a medium diameter ( $\sim 750\mu\text{m}$ ), this gradually decreased up to day 6 and then increased again to almost twice the initial size. The difference, however, lies in the fact that the spheroids with U2OS cells appeared to have greater roundness and were more compact, therefore these were slightly smaller than those with SaoS-2 cells, which appeared to be less compact and homogeneous<sup>[124][125]</sup>. The size decreased over the first 6 days because the cells initially tended to aggregate to each other, to give rise to the spheroid, then, as they proliferated they increased in number and, thus, the diameter increased over time<sup>[149]</sup>, as shown in Figures 49 and 50.

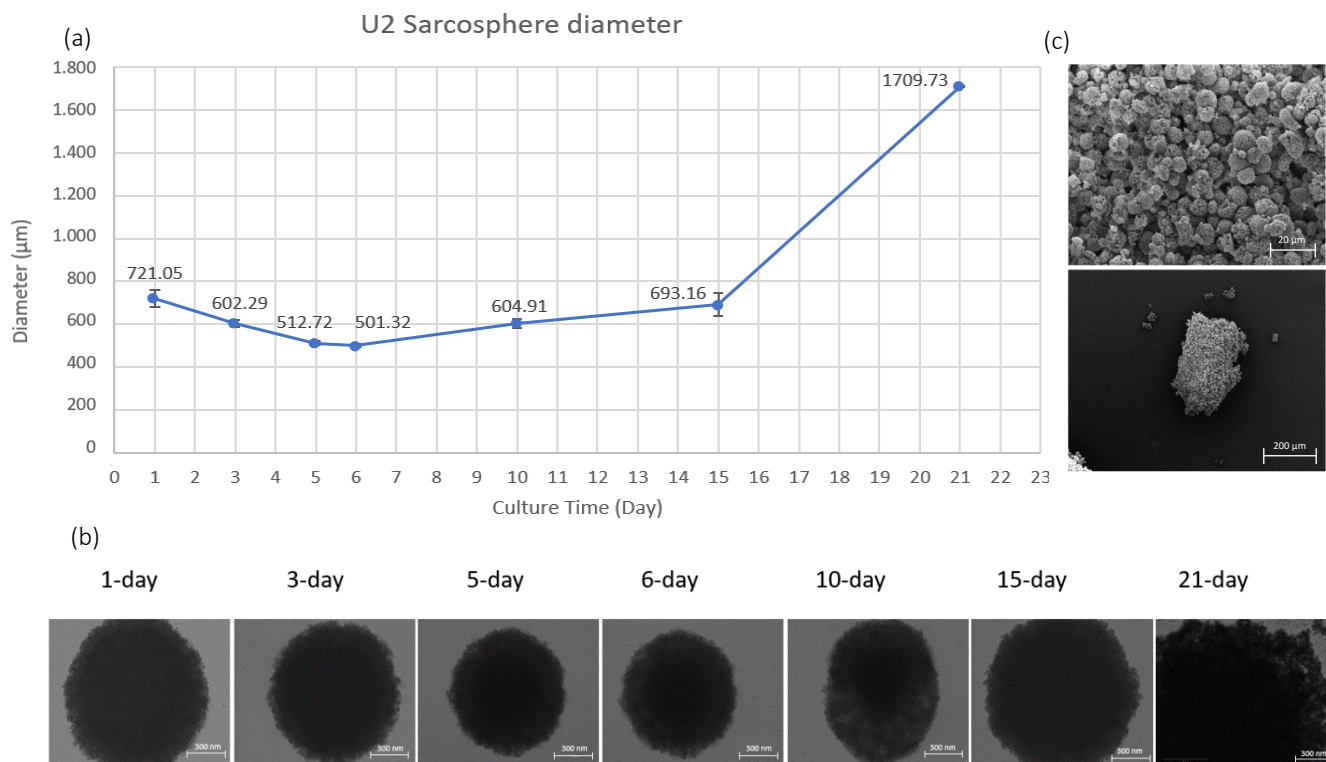


**Figure 49:** (a) U2OS Sarcospheres diameter over 21 days analyzing values with ImageJ software, (b) U2OS Sarcospheres images taken with EVOS M5000 Fluorescence Microscope over 21 days – bar 300nm, (c) TEM images U2OS Sarcospheres – bar 20 μm (above), 200 μm (below).

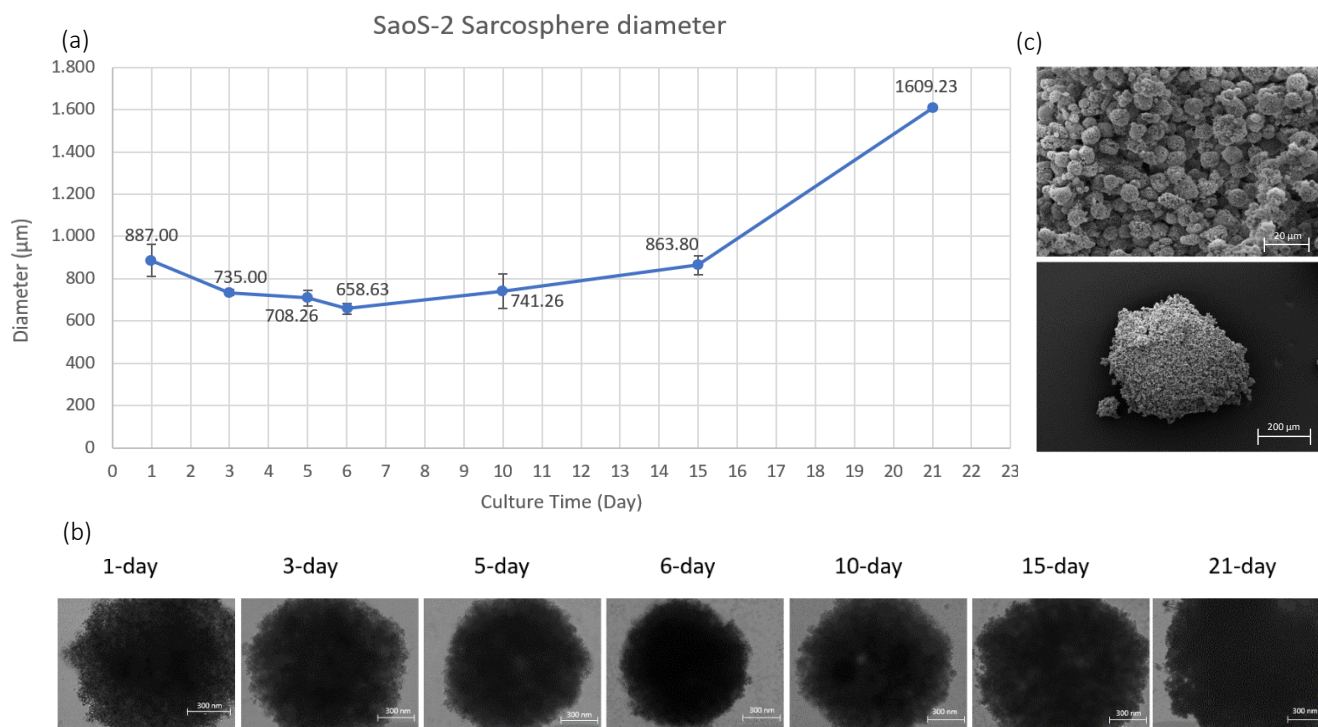


**Figure 50:** (a) SaoS-2 Sarcospheres diameter over 21 days analyzing values with ImageJ software, (b) SaoS-2 Sarcospheres images taken with EVOS M5000 Fluorescence Microscope over 21 days, (c) TEM images SaoS-2 Sarcospheres - bar 20 μm (above), 200 μm (below).

## 5.5 Cell Tests

### 5.5.1 Cell-interacting drugs amount

In Table 24 and 25 have been reported the amount of NPs, mixed with DMEM medium, incubated with the cell and the different amounts of miRNA and drugs used for the treatments. In particular, these amounts refer to the total per well, showing in Table 24 and 25 the amounts used to treat cell in one well of 2D cell model and one well with one Sarcosphere, respectively. Regarding the concentration of nanoparticles used with the 2D cell model, it was chosen to take 200 $\mu$ l from each of the four types of NPs (previously suspended in SAB) and add 800  $\mu$ l of DMEM medium<sup>[107][121]</sup>. From this resulting 1ml of solution, 500  $\mu$ l were taken to interact with the cells, pipetting this quantity into each well of the 2D culture. Regarding the concentration of NPs used for the spheroids, it was taken, from each of the four types of nanoparticles, 200  $\mu$ l and added to this 50 $\mu$ l of DMEM medium. The obtained 250 $\mu$ l, was incubated with one cellular Sarcosphere, pipetting the total 250 $\mu$ l of the solution into each well. The amounts of miRNA-34a and drugs actually incubated with the cells were calculated and the results were shown in Table 24 (for the amounts interacted with 2D cell model) and in Table 25 (for the amounts interacted with Sarcosphere model), taking into account the amount of miRNA and drugs was previously encapsulated by each of the four NPs.

**Table 24:** Amount of miR-34a and drugs made to interact with 2D cell model (for one well).

NPs	Withdrawn amount of NPs ( $\mu$ l)	Added medium to the amount of NPs ( $\mu$ l)	Withdrawn amount ( $\mu$ l) of NPs+medium	miR-34a ( $\mu$ g) in withdrawn amount	Doxorubicin ( $\mu$ g) in withdrawn amount	Resveratrol ( $\mu$ g) in withdrawn amount
miR-NPs	200	800	500	1.00	-	-
miRDx-NPs	200	800	500	1.00	0.95	-
miRDxRs-NPs	200	800	500	1.00	0.88	0.50
LbL-NPs	200	800	500	1.00	1.90	1.00

**Table 25:** Amount of miR-34a and drugs made to interact with 3D Sarcosphere model (for one well).

NPs	Withdrawn amount of NPs ( $\mu$ l)	Added medium to the amount of NPs ( $\mu$ l)	Withdrawn amount ( $\mu$ l) of NPs+medium	miR-34a ( $\mu$ g) in withdrawn amount	Doxorubicin ( $\mu$ g) in withdrawn amount	Resveratrol ( $\mu$ g) in withdrawn amount
miR-NPs	200	50	250	2.58	-	-
miRDx-NPs	200	50	250	2.09	1.90	-
miRDxRs-NPs	200	50	250	1.97	1.77	0.97
LbL-NPs	200	50	250	2.82	3.88	2.07

### 5.5.2 Live and Dead assay

#### Live and Dead assay on bidimensional model

Figures 51-59 show the live and dead tests conducted on cells in the two-dimensional model, in order to evaluate cells viability with and without incubation with the different manufactured nanoparticles, at different time points (2,5,7 days) and cell densities (2000,4000,8000 cells/well). In Figure 51 live and dead images of the SaoS-2 cells were shown at three different time points, without the incubation with any of the manufactured nanoparticles, as well as for the U2OS cells in Figure 52. First of all, the morphology of the two cell types was different, reporting SaoS-2 cells more elongated and bigger than U2OS cells<sup>[150]</sup>. It was also seen how both cell types proliferated and thus grew in numbers as the number of days of culture increased<sup>[149]</sup>. In Figure 53 were shown live and dead images of the U2OS cells at three different density, after 24h, 48h and 72h of incubation with the miR-NPs, as well as for U2OS cells incubated with miRDx-NPs, miRDxRs-NPs and LbL-NPs in Figure 54-56. In the upper part, live (green) and dead (red) cells were shown together while in lower part just the dead ones.

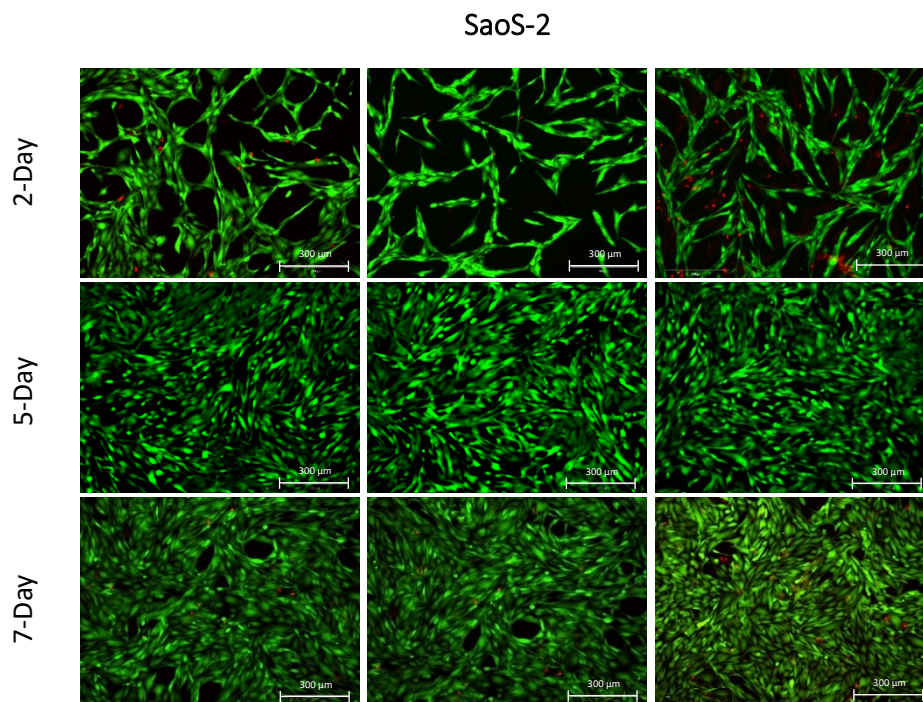


*Figure 51: Live and dead images of non-treated SaoS-2 cells in bidimensional culture, at different time points.*

## U2OS

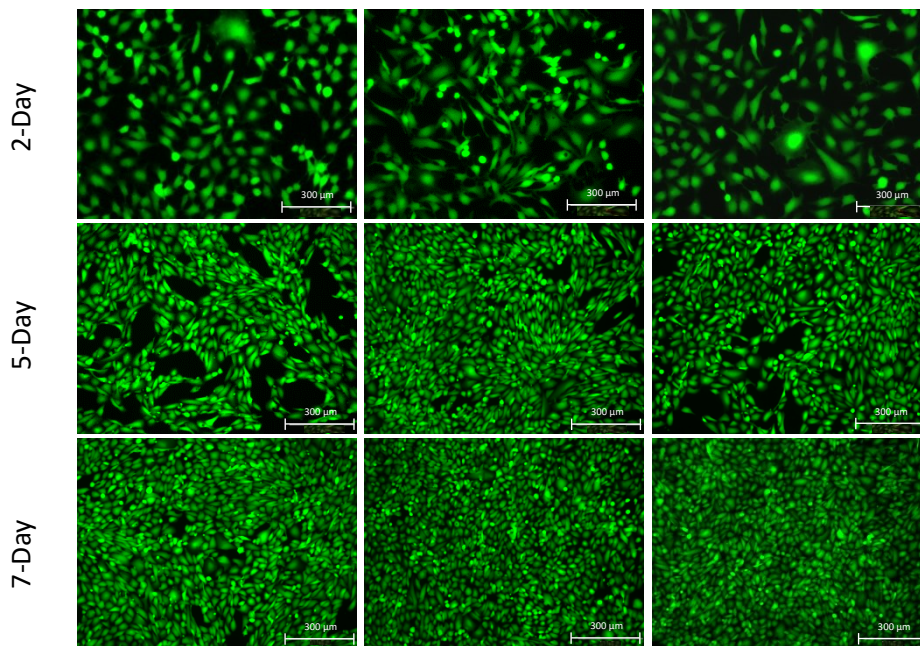


*Figure 52: Live and dead images of non-treated U2OS cells in bidimensional culture, at different time points.*

Looking at the Figure 53, no marked cell death was noticed, indicating low apoptotic activity of miR-NPs, in fact the amount of dead cells didn't change significantly between the different time points. It seemed that the amount of live cells remained approximately the same but, at 48h and 72h, they changed their morphology conformation becoming smaller and more compact compared to the cells after 24h of incubation<sup>[142]</sup>. The cells treated with miRDx-NPs showed reduced cell viability, suggesting that intracellular restoration of miRNA-34a and delivery of Doxorubicin could have led to the apoptosis of U2OS cells, in particular the amount of dead cells increased as the hours of incubation increased. Previous studies reported in fact that miRNAs have synergistic antitumor effects with conventional chemotherapy as Doxo<sup>[139]</sup>. Furthermore, it was seen a remarkable change of morphology as the time of incubation increased. In Figure 55 the incubation with miRDxRs-NPs turned out to have a slight influence on the vitality of the cells because the number of dead cells remained approximately the same, increasing a little from 24h to 72h of incubation, while the morphology seemed to change, as previously reported, with the other NPs treatments. Significant decreases in cell viability were observed in U2OS cells treated with LbL-NPs compared to the cells treated with the other three types of NPs, in fact, in Figure 56, it was noticed the LbL-NPs remarkable apoptotic activity on U2OS cells, yet from 24h of incubation; the dead cells were very high in number yet at 24h of incubation, rapidly increasing at 48h and 72h. This suggested that nanoparticles with natural nanocoating materials achieved by layer-by-layer technique might be more efficient in carrying miR-34a, Doxo, and Resv internal to the core without excessive dispersion of them out of the target site<sup>[146]</sup>, and would also be able to carry more drugs due to their additional presence in the various layers. The more cytotoxic effect could therefore

be due to the synergistic action of the various drugs that manage to reach the target<sup>[147][148]</sup>, considering also the small amount of resveratrol that had been encapsulated and therefore may also have succeeded in treating the cells<sup>[145]</sup>.

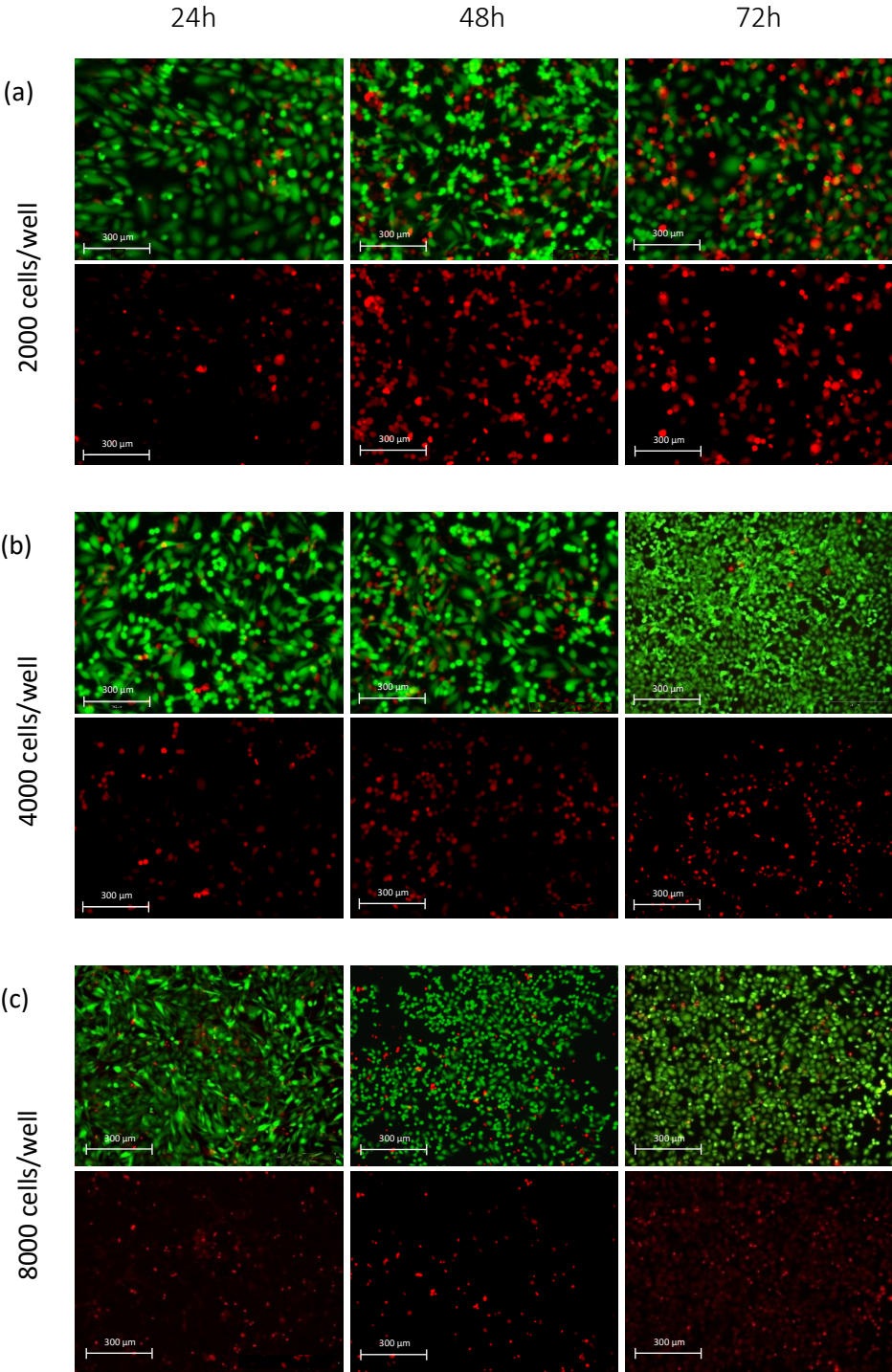


*Figure 53: (a) Live and dead U2OS cells with 2000cells/well as density, after 24h,48h,72h of miR-NPs incubation, (b) Live and dead U2OS cells with 4000cells/well as density, after 24h,48h,72h of miR-NPs incubation, (c) Live and dead U2OS cells with 8000cells/well as density, after 24h,48h,72h of miR-NPs incubation*

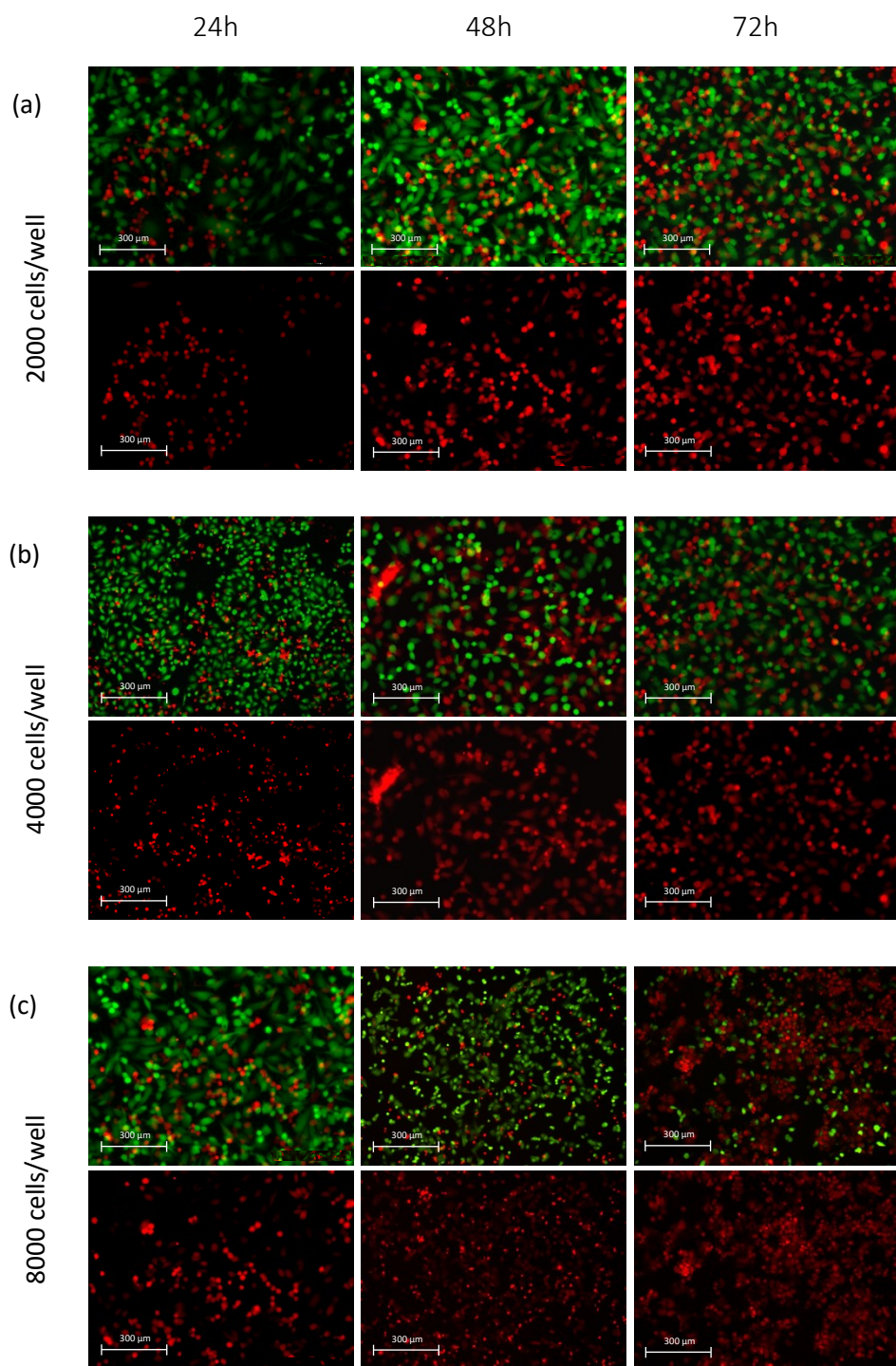


*Figure 54: (a) Live and dead U2OS cells with 2000cells/well as density, after 24h,48h,72h of miRDx-NPs incubation, (b) Live and dead U2OS cells with 4000cells/well as density, after 24h,48h,72h of miRDx-NPs incubation, (c) Live and dead U2OS cells with 8000cells/well as density, after 24h,48h,72h of miRDx-NPs incubation.*

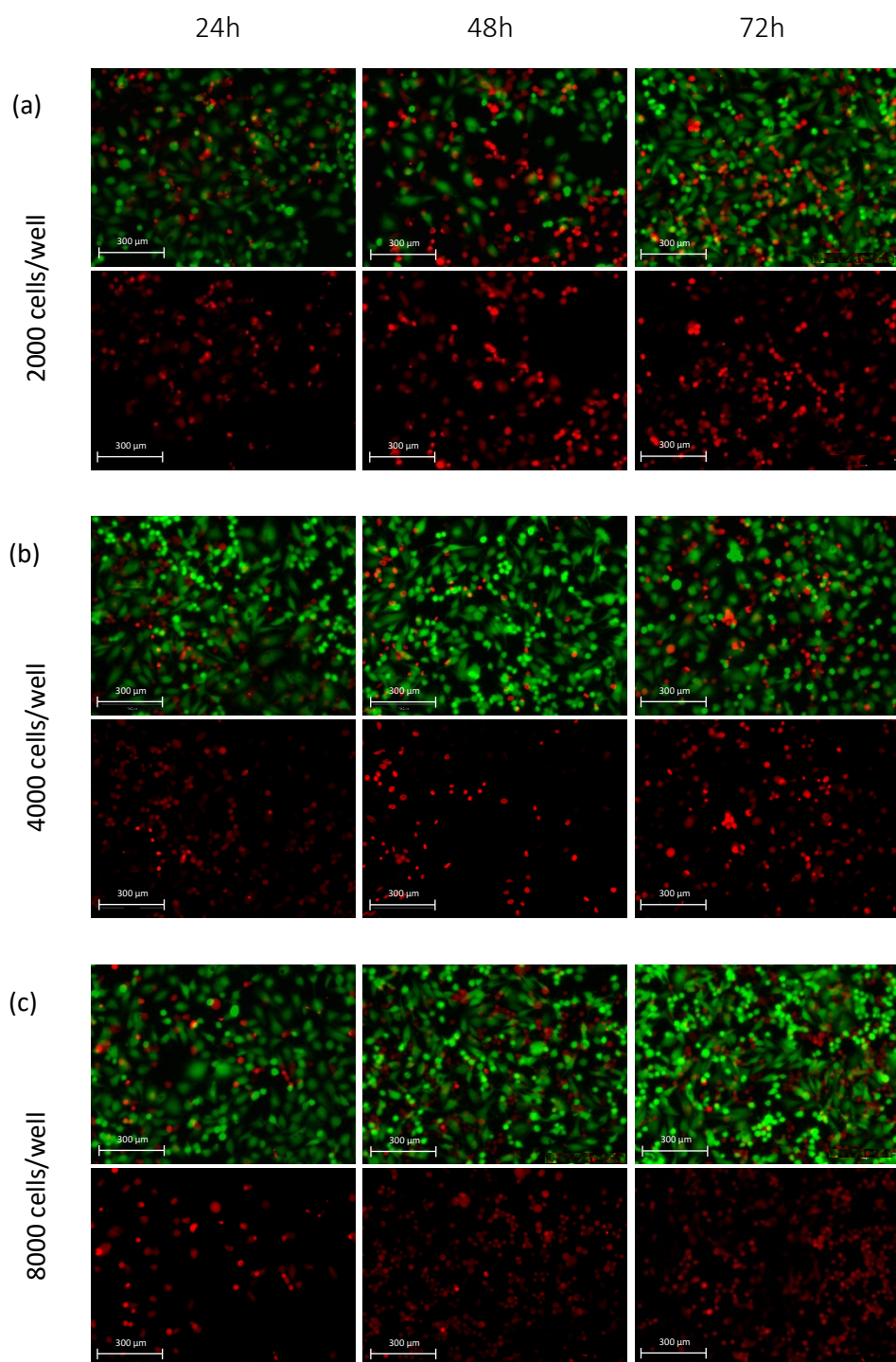
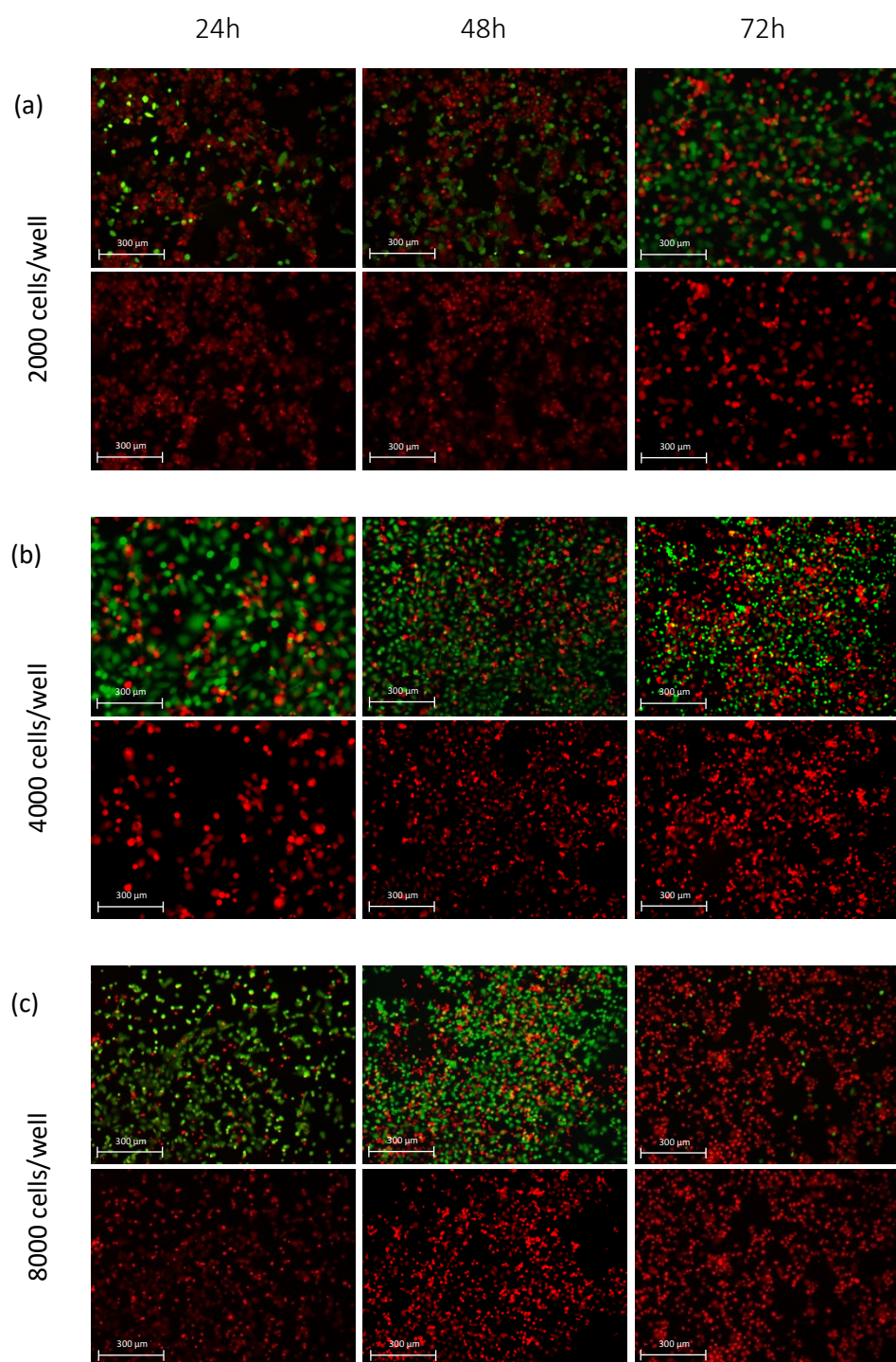
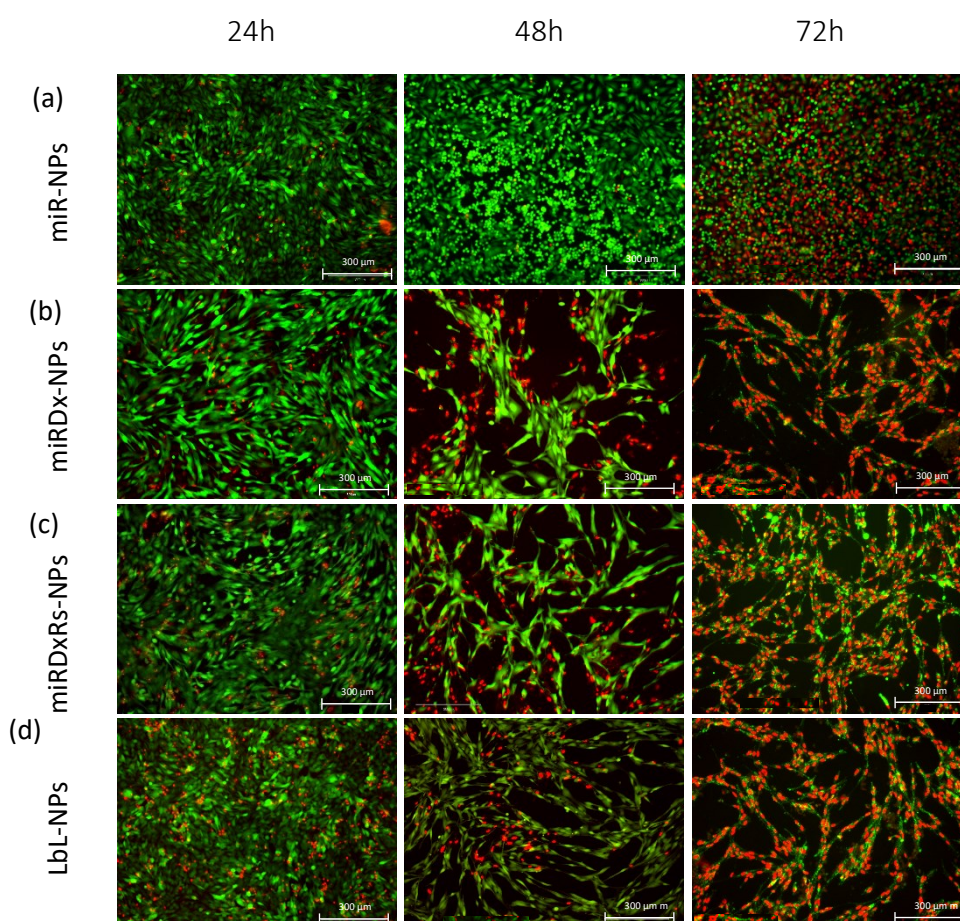


Figure 55: (a) Live and dead U2OS cells with 2000cells/well as density, after 24h,48h,72h of miRDxRs-NPs incubation, (b) Live and dead U2OS cells with 4000cells/well as density, after 24h,48h,72h of miRDxRs-NPs incubation, (c) Live and dead U2OS cells with 8000cells/well as density, after 24h,48h,72h of miRDxRs-NPs incubation.



*Figure 56: (a) Live and dead U2OS cells with 2000cells/well as density, after 24h,48h,72h of LbL-NPs incubation, (b) Live and dead U2OS cells with 4000cells/well as density, after 24h,48h,72h of LbL-NPs incubation, (c) Live and dead U2OS cells with 8000cells/well as density, after 24h,48h,72h of LbL-NPs incubation.*

In Figure 57 have been shown live and dead SaoS-2 cells after 24h, 48h and 72h of incubation with any of manufactured nanoparticles. Live (green) and dead (red) cells were shown together. First of all, a remarkable difference between miR-NPs and the other treatments was observed, noticing a not remarkable influence of miR-NPs on cell viability after 24h and 48h of incubation. In fact, the number of dead cells after 24h and 48h of treatment was almost null, showing on the other hand, a difference in the morphology conformation of the cells, which became smaller and more compact. Conversely, after 72h of incubation, the number of live cells notably decreased<sup>[143][144]</sup>, together with the decreased dimension and changed morphology of the cells. The effect of miRDx, miRDxRs and LbL NPs looked to be very similar to each other, with a very low number of dead cells after 24h of treatment, whereas almost all died after 72h of incubation; this suggested again more efficient synergistic antitumor effects of combinations with conventional chemotherapy drugs<sup>[127][147][148]</sup>. Moreover, it seemed that SaoS-2 cells needed longer incubation times in order to completely kill them, compared to the times required from U2OS cells.



**Figure 57:** (a) Live and dead SaoS-2 cells with 2000cells/well as density, after 24h,48h,72h of LbL-NPs incubation, (b) Live and dead SaoS-2 cells with 4000cells/well as density, after 24h,48h,72h of LbL-NPs incubation, (c) Live and dead SaoS-2 cells with 8000cells/well as density, after 24h,48h,72h of LbL-NPs incubation.

### Live and Dead assay on Sarcosphere model

Figure 58 and 57 showed live and dead U2OS and SaoS-2 cells in Sarcospheres models (100000cells/well) respectively, after 24h, 48h and 72h of incubation with any of the manufactured NPs. In the upper part, live and dead cells were shown together while in lower part there were shown just the dead cells. Both SaoS-2 and U2OS Sarcospheres seemed to have similar trends toward NPs treatments. As the time of incubation increased, the green circular structure, represented live cells, became smaller, while the necrotic core, represented the dead cells, seemed to increase, remarking the growth of dying cells in the core as the time of the treatment increased. The presence of the necrotic core confirmed that this model was characterized by hypoxic regions and necrotic centers, and thus it represented a valid model capable of mimicking tumor micro-regions or micro-metastasis as reported in previous studies<sup>[151]</sup>. No study has been conducted in the literature on the effect of miR-34a on U2OS and SaoS-2 spheroids models of osteosarcoma but, from what it was reported during this study, it seemed that the addition of Doxorubicin and Resveratrol in the NPs increased their apoptotic and interfering activity in the spheroids, in fact a bigger necrotic core was observed, compared to necrotic core of spheroid treated with NPs with just miRNA-34a inside. This consideration was in line with others studies, where doxorubicin was proved to have a remarkable cytotoxic effect on OS spheroids<sup>[45][151]</sup> and the that miRNAs could have more efficient synergistic antitumor effects with conventional chemotherapy drugs as Doxo<sup>[127][147][148]</sup>,

U2OS - Sarcospheres

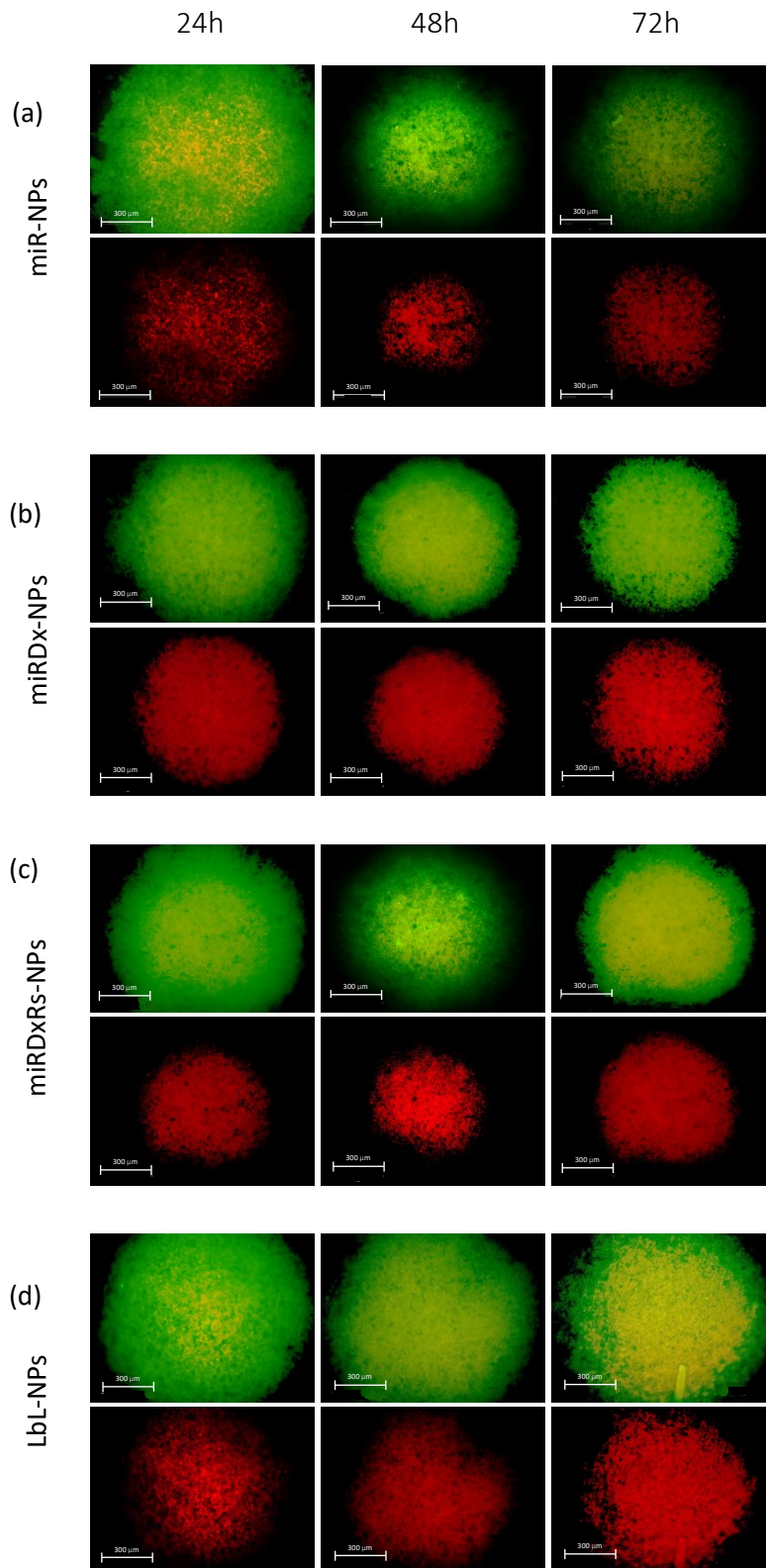


**Figure 58:** (a) live and dead U2OS Sarcosphere cells after 24h,48h,72h of miR-NPs incubation, (b) live and dead U2OS Sarcosphere cells after 24h,48h,72h of miRDx-NPs incubation (c) live and dead U2OS Sarcosphere cells after 24h,48h,72h of miRDxRs-NPs incubation, (d) live and dead U2OS Sarcosphere cells after 24h,48h,72h of LbL-NPs incubation.

SaoS2 - Sarcospheres

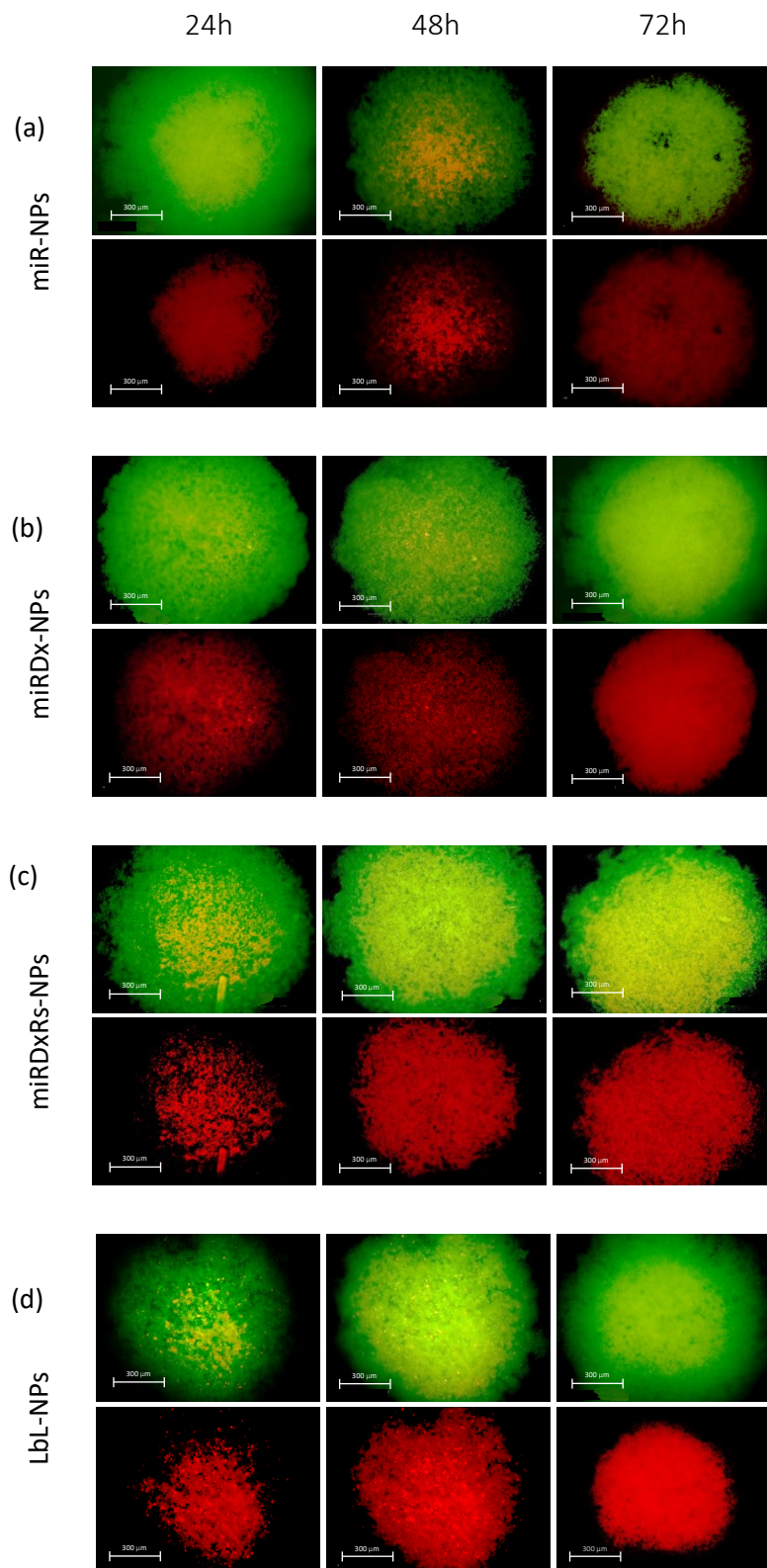


**Figure 59:** (a) live and dead SaoS-2 Sarcosphere cells after 24h,48h,72h of miR-NPs incubation, (b) live and dead SaoS -2 Sarcosphere cells after 24h,48h,72h of miRDx-NPs incubation (c) live and dead SaoS -2 Sarcosphere cells after 24h,48h,72h of miRDxRs-NPs incubation, (d) live and dead SaoS -2 Sarcosphere cells after 24h,48h,72h of LbL-NPs incubation.

### 5.5.3 PrestoBlue essay

#### PrestoBlue essay on bidimensional model

Figures 60 and 61 show the PrestoBlue essay conducted on the cells in two-dimensional model, in order to evaluate the metabolic activity of the cells, before and after the treatment with any of the manufactured nanoparticles. Figure 60 reported metabolic activity, in terms of fluorescence values of the PrestoBlue solution, of U2OS cells at four time points of the evaluation of the essay (1h,2h,3h,4h), after 24h,48h and 72h of incubation with the nanoparticles, as well as for the SaoS-2 cells in Figure 61. It was immediately noticed that greater fluorescence values, and thus greater metabolic activity, were shown after the incubation with miR-NPs, which therefore seemed to interfere less, compared to the other NPs, with cell metabolic activity. Fluorescence values increased rapidly as the period of incubation with the PrestoBlue solution increased and as the cell density within each time point grew. This trend was quite common to all the 4 combinations of NPs tested. Looking at the three different time points in Figure 60, it was reported that, after 24h of incubation, the cells showed higher metabolic activity with fluorescence growth slopes steeper (for any of the treatments) compared to the subsequent time points (48h and 72h).

Samples treated with LbL-NPs, after 48h of incubation, showed a gradual small increase of the fluorescence value, indicating a reduced metabolic activity, as well as for samples treated with any of the NPs after 72h of incubation, at exception of the miR-NPs treatment. Figure 61 reported the values of fluorescence obtained for SaoS-2 cells: 24 and 48h of incubation looked to be very similar to the values obtained at same time points for U2OS cells, while 72h of incubation in SaoS-2 cells showed many differences. In fact, even after 72h of incubation with any of the manufactured NPs, the metabolic activity of SaoS-2 cells were not affected as greatly as U2OS cells were, but instead their fluorescence appeared to still be rapidly growing during the different time points. This suggested greater resistance from SaoS-2 cells to the NPs treatment. The reported general decrease in cells metabolic activity, after the different nanoparticles treatments, could be due to the fact that NPs interfered with their metabolic activity, killing many of them so that fewer cells remained to contribute to the fluorescence signal.

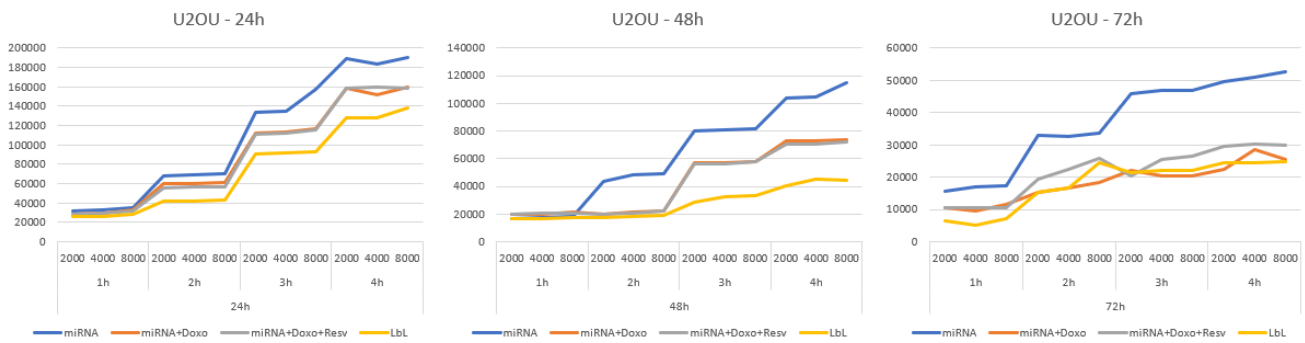


**Figure 60:** Fluorescence of PrestoBlue reagent analyzed at 1,2,3,4h on U2OS bidimensional cells at 2000, 4000 and 8000cells/well as densities, after 24h,48h,72h of incubation with any of the manufactured NPs.



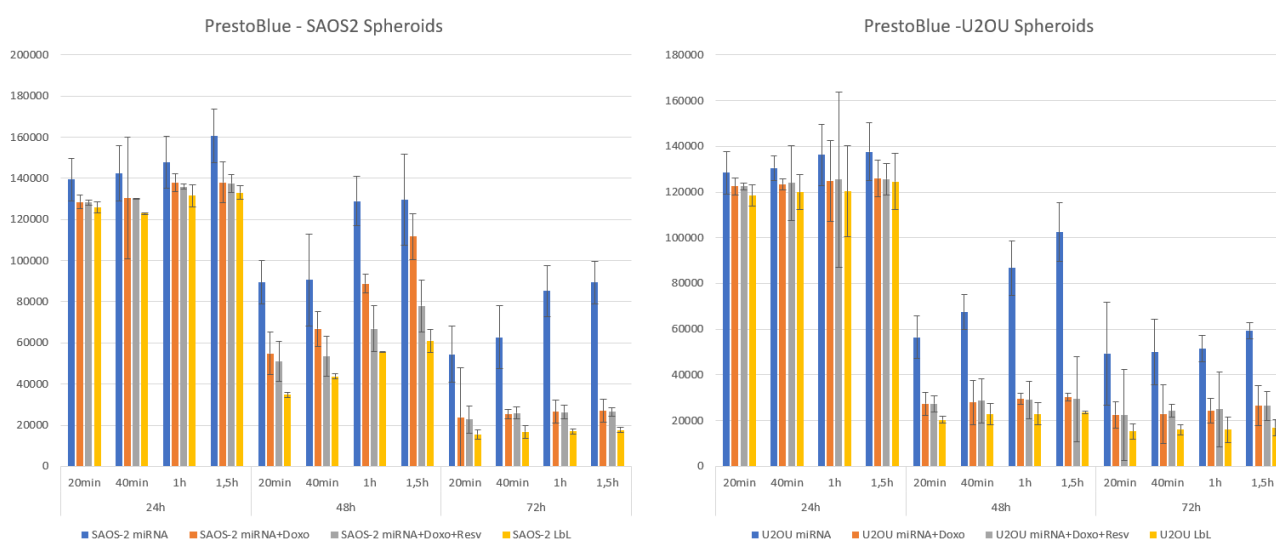
**Figure 61:** Fluorescence of PrestoBlue reagent analyzed at 1,2,3,4h on Saos-2 bidimensional cells at 2000, 4000 and 8000cells/well as densities, after 24h,48h,72h of incubation with any of the manufactured NPs.

## PrestoBlue assay on Sarcosphere model

Figure 62 showed the PrestoBlue assay evaluated on Sarcosphere model, in order to analyze the metabolic activity before and after the incubation with the different manufactured nanoparticles. In Figure 62 (a) metabolic activity, in terms of fluorescence of the PrestoBlue solution, of U2OS Sarcospheres was shown at four different time points (1h,2h,3h,4h), after 24h,48h and 72h of incubation with any of the manufactured nanoparticles, as well as for the SaoS-2 Sarcospheres in Figure 62 (b). Table 26 reported the fluorescence values of non-treated Sarcospheres, analyzing the assay at the different time points. Looking at the Figure 62, an overall common behavior was observed: the biggest values of fluorescence were found after 24h of incubation and they became smaller as the time of incubation increased. This consideration was particularly marked for U2OS cells where the fluorescence, from 24h incubation, greatly decreased to 48h and 72h where it seemed to stay approximately to the same value of 25000. An exception was the treatment with miR-NPs during which fluorescence values gradually decreased between the different time of incubation. After 24h, spheroids didn't show relevant changes in their metabolic activity, when incubated with any of the manufactured NPs and this consideration, at the initial stage, could be due to spheroid densification and a reduction in drug permeability<sup>[125]</sup>. However, both SaoS-2 and U2OS spheroids at 72h had essentially collapsed, with the exception of the spheroids treated with miR-NPs that seemed to have a less marked cytotoxic effects.

**Table 26:** Fluorescence of PrestoBlue reagent of non-treated U2OS and SaoS-2 sarcospheres at 20min, 40min, 1h and 1.5h.

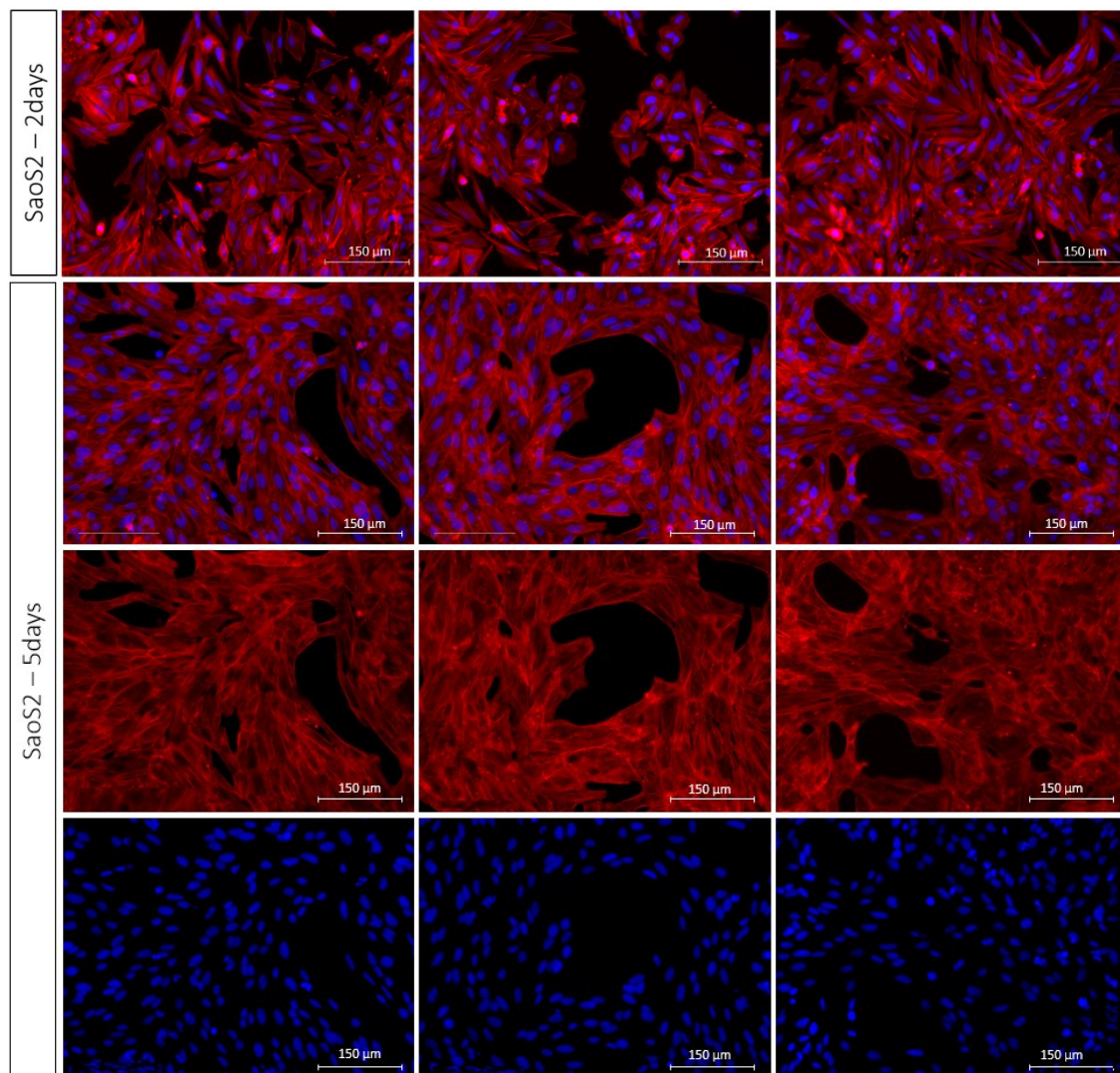
Cells	20 min	40 min	1h	1,5h
U2OS	187325	188542	195996	198536
SaoS-2	188244	188429	190421	191232



**Figure 62:** (a) Fluorescence of PrestoBlue reagent analyzed at 20min, 40min, 1h and 1.5h on SaoS-2 sarcospheres, after 24h,48h,72h of incubation with any of the manufactured NPs. (b) Fluorescence of PrestoBlue reagent analyzed at 20min, 40min, 1h and 1.5h on U2OS sarcospheres, after 24h,48h,72h of incubation with any of the manufactured NPs.

#### 5.5.4 Immunostaining

Figures 63, 64, 65 and 66 showed the immunostaining assay evaluated on both types cells, in order to discern the cytoskeletons and nucleus of treated and non-treated cells. Figure 63 showed the results of non-treated SaoS-2 cells at three different culture times (2,5,7 days), as well as for U2OS cells in Figure 64 . Figure 65 reported instead the results of the treated U2OS cells after 24h, 48h and 72h of incubation with any of the manufactured nanoparticles, as well as for the SaoS-2 cells in Figure 66. It was noticed that non treated cells were more elongated, uniformly occupying the space and growing as the culture time increased, while both treated SaoS-2 and U2OS cells became smaller and narrower, as the incubation time increased, getting then to the difficulty of discerning cytoskeleton from nucleus. Both treated cells types seemed to have similar particulate morphology, therefore finding it difficult to establish a morphological difference between them after the NPs treatments.



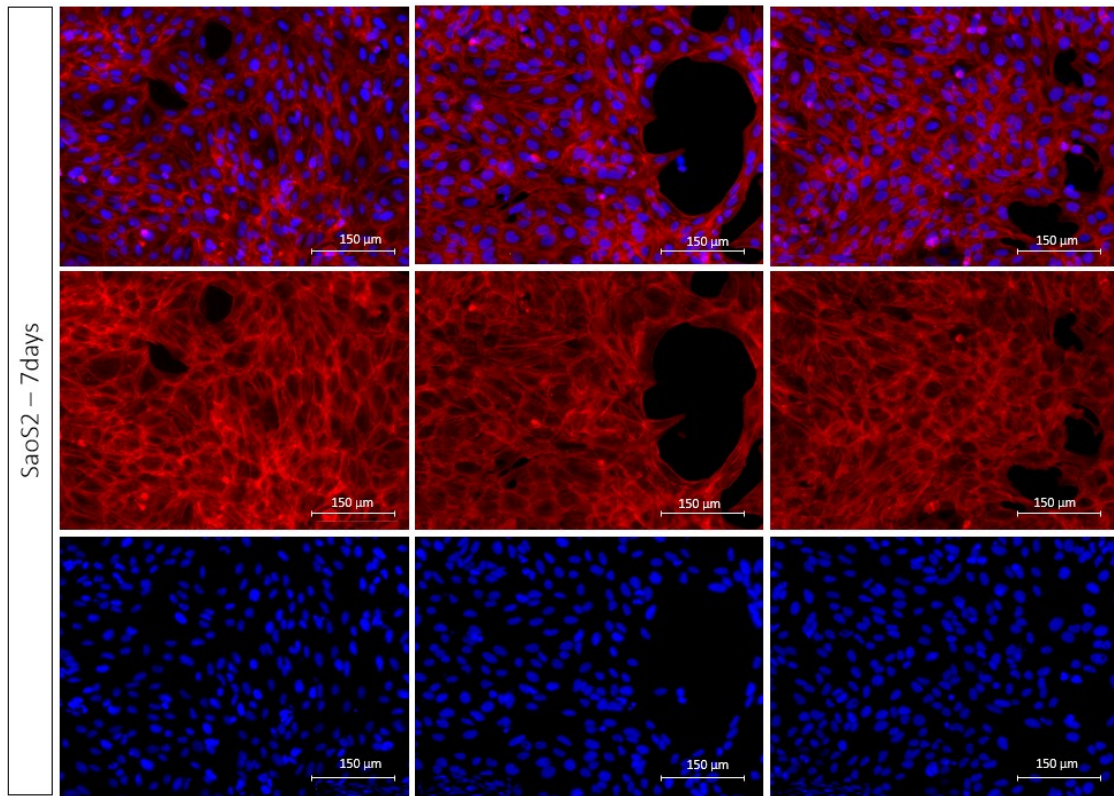
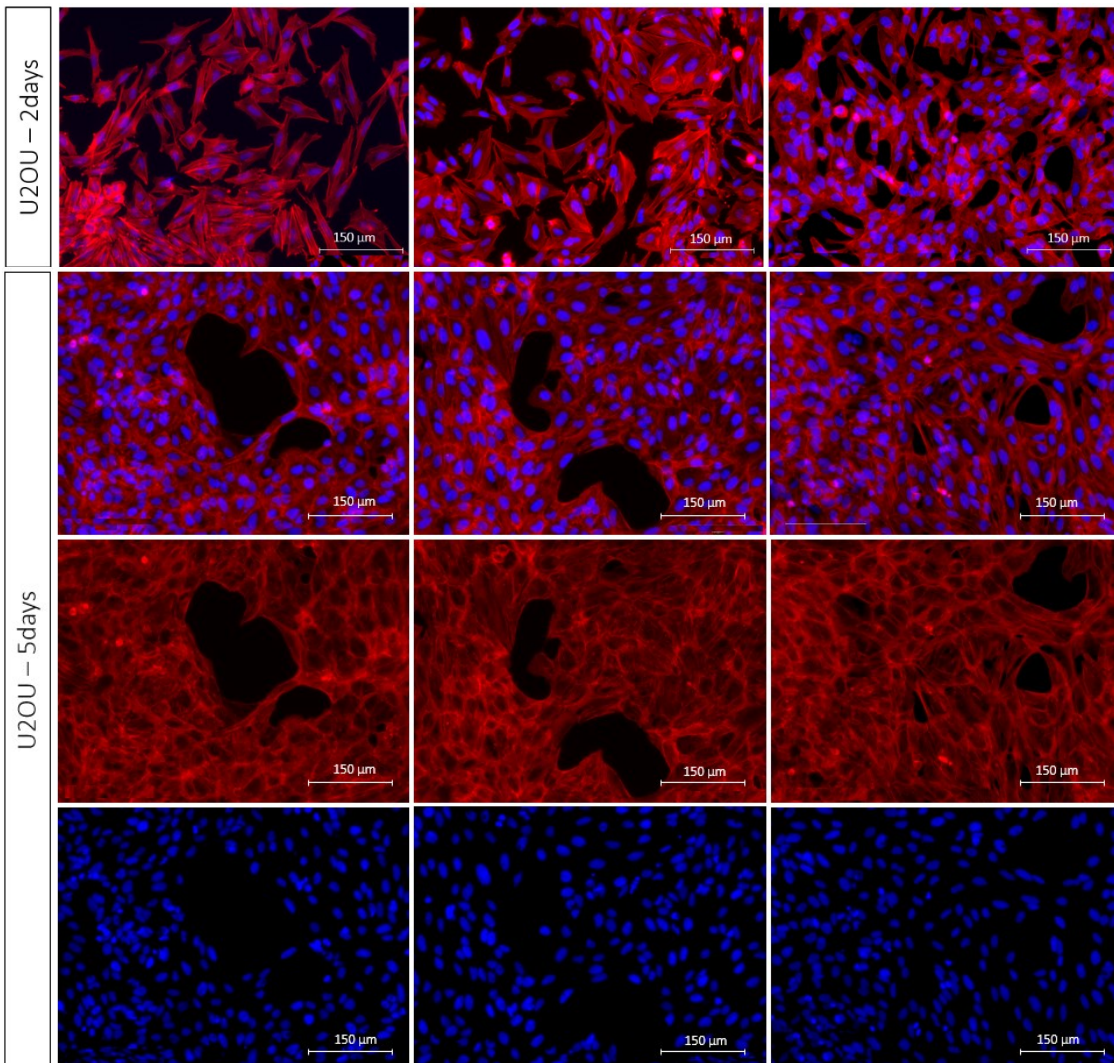


Figure 63: Immunostaining of non-treated *SaoS-2* bidimensional model at 2,5 and 7 days.



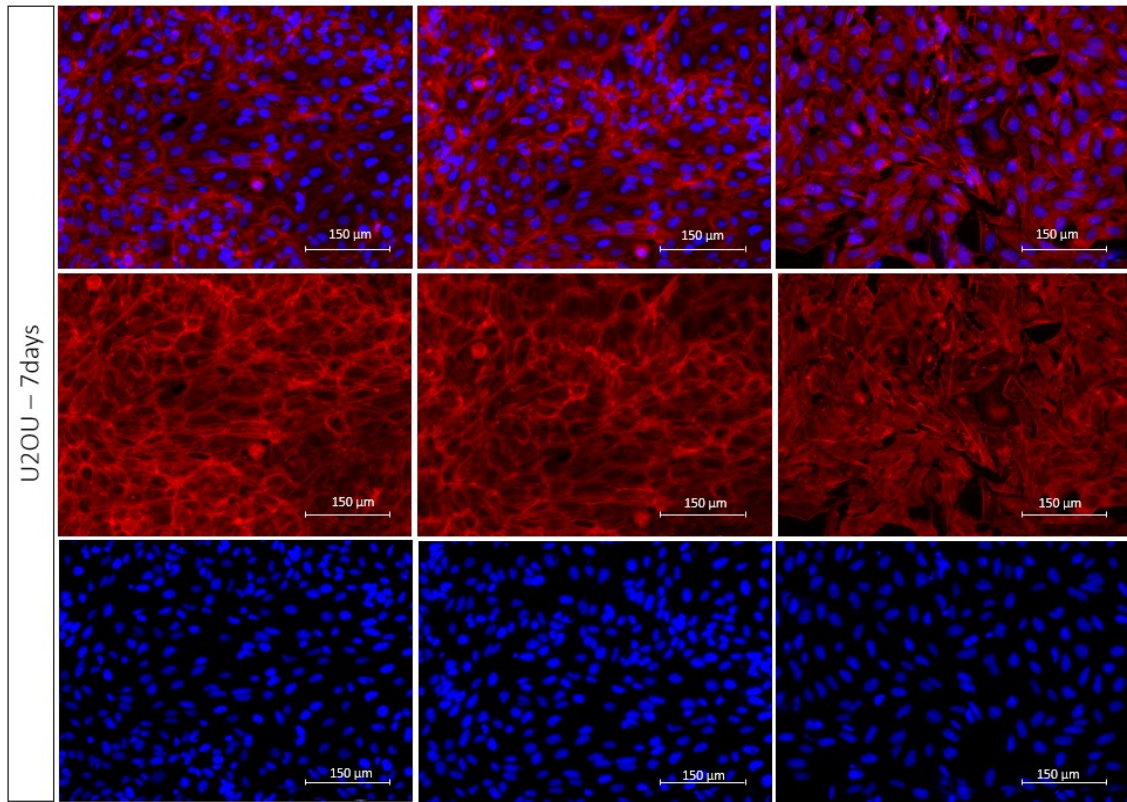
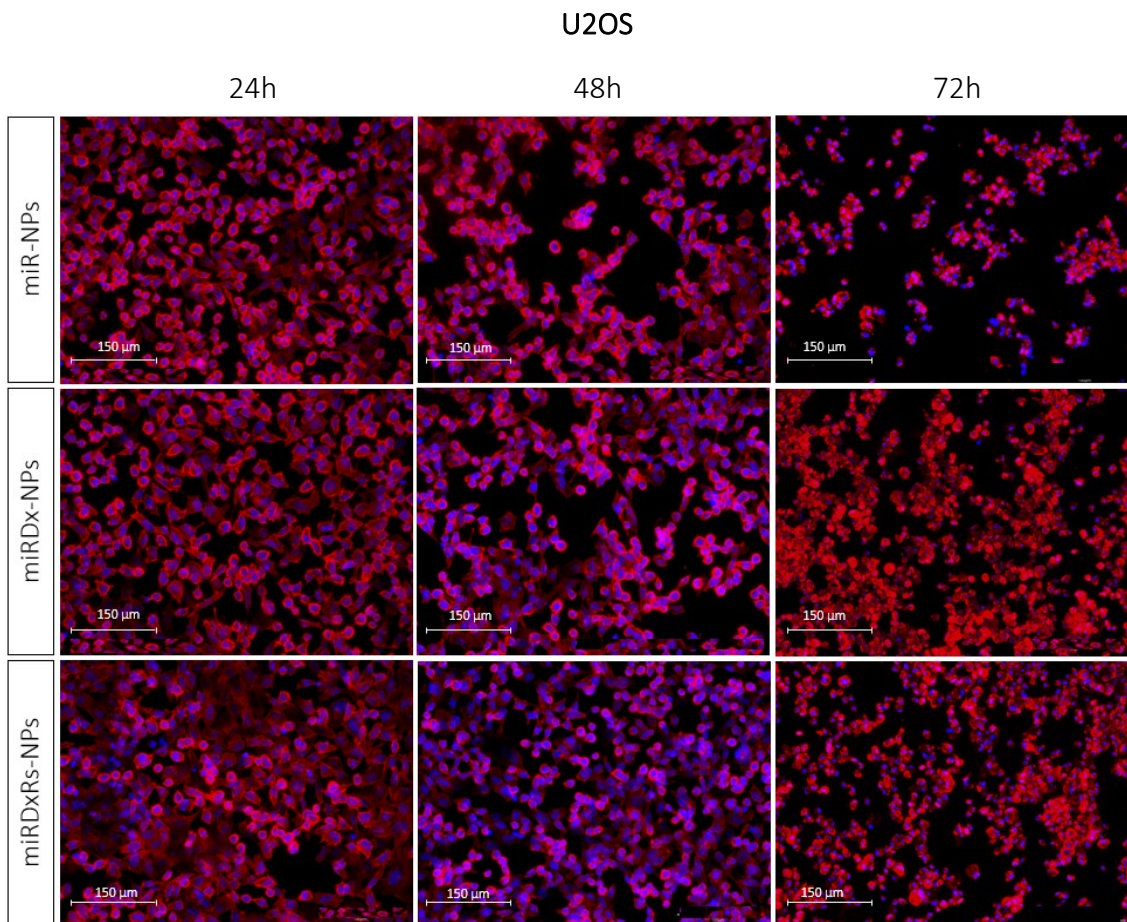
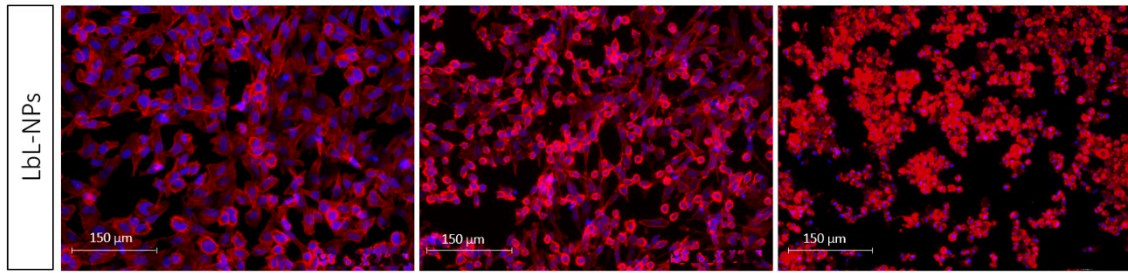
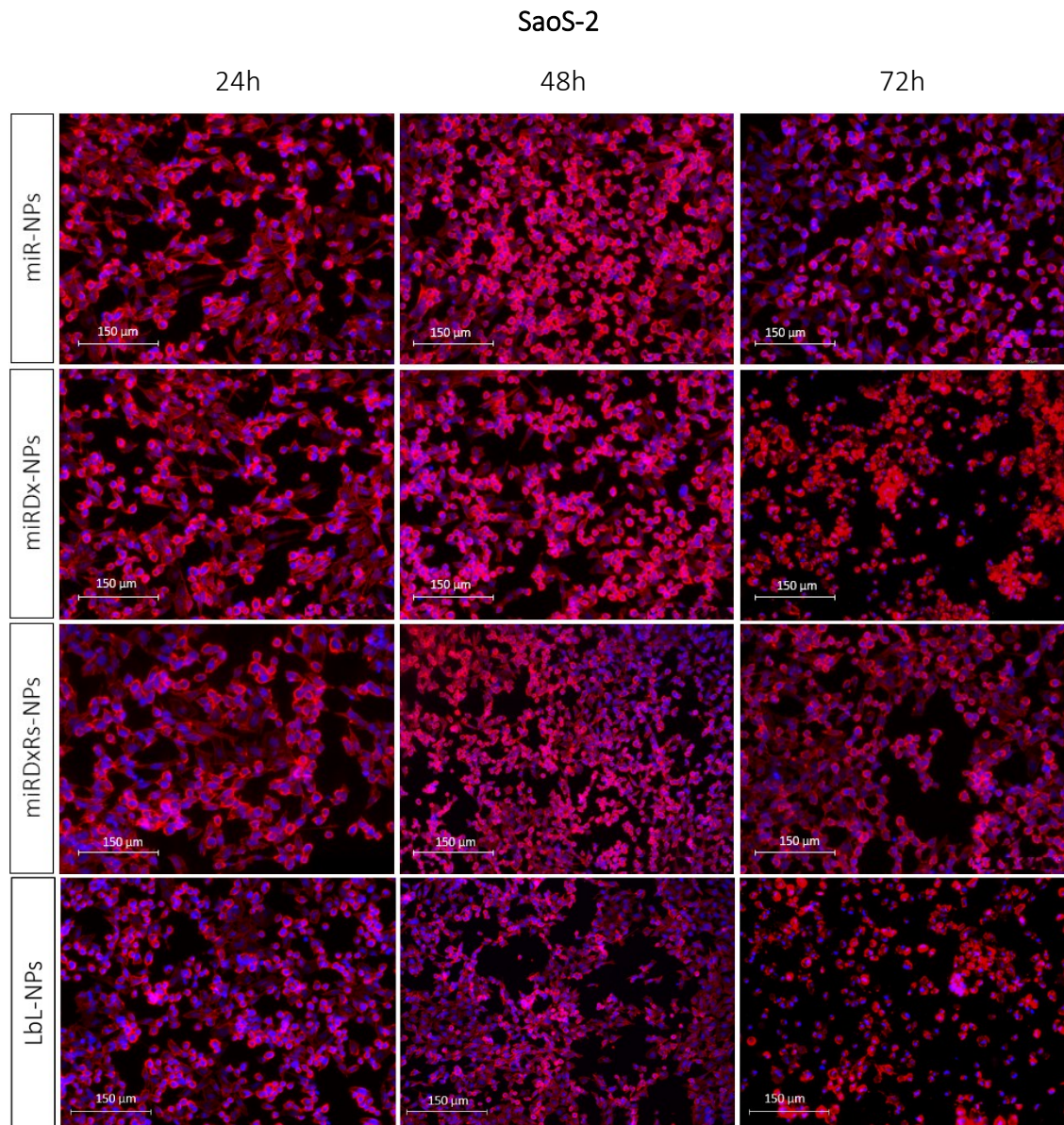


Figure 64: Immunostaining of non-treated U2OS bidimensional cells at 2,5 and 7 days





*Figure 65: Immunostaining of treated U2OS cells in bidimensional model, after 24, 48 and 72h of incubation with any of the manufactured nanoparticles.*



*Figure 66: Immunostaining of treated SaoS-2 cells in bidimensional model, after 24, 48 and 72h of incubation with any of the manufactured nanoparticles.*

## 6. Conclusions

In this thesis, it is reported an effective application of manufactured nanocarriers systems to simultaneously deliver tumor suppressive miRNA-34a, Doxorubicin and Resveratrol into an in vitro manufactured Osteosarcoma spheroids and bidimensional cell models. Chitosan and PLGA showed to be ideal materials in nanocarrier applications to combat Osteosarcoma, displaying suitable features ( excellent mechanical properties, biodegradability, biocompatibility...) in addition to having FDA and EMA approval for pharmaceutical applications.<sup>[107]</sup> Starting from miR-NPs (Chitosan-PLGA-miR34a NPs), these nanoparticles evidenced a suitable size and preferential charge for use in Osteosarcoma, as well as displaying the ability to encapsulate miRNAs efficiently, while preserving the spherical shapes and sizes. The resulting manufactured nanoparticles have shown interesting properties: miRDx and miRDxRs NPs showed slightly larger size than miR-NPs, probably due to the inserting of Doxo and Doxo plus Resv, respectively. Looking at TEM results, it was revealed a distinct morphological change, showing a different pattern core probably due to the internal presence of drugs. These two types of nanoparticles still evidenced a suitable size and preferential charge for use in Osteosarcoma, as well as displaying the ability to encapsulate the miRNA and Doxorubicin efficiently, regarding both types. In contrast, the encapsulation of Resveratrol by the miRDxRs-NPs was less efficient, in fact there was just a 10% of encapsulation rate. The last type of manufactured nanoparticles were the LbL-NPs, nanocoating the miRDxRs-NPs with a first layer of pectin successfully extracted from the cocoa biowaste during this work and a second layer of chitosan. LbL-NPs showed bigger size compared to the previous ones but still suitable in terms of size and charge for use in Osteosarcoma. TEM images confirmed the different core morphology comparing to the miR-NPs, in fact the LbL-NPs core looked like miRDx and miRDxRs NPs, probably due to the presence of drugs internally to the structure. In LbL-NPs TEM images it appeared the presence of the two forming layers around the nanoparticle as circular surface halo around the spherical structure. Zeta potential results, reported during the preparation phases of the LbL-NPs, confirmed the charge variation as expected, alternating positive to negative charge depending on the layer. The encapsulation efficiency of miRNA and Doxo was acceptable, although it encapsulated very little Doxo in relation to the amount that had been inserted, but this was nonetheless greater than Doxo encapsulated in the other manufactured NPs. Insufficient, again, was the encapsulation of Resveratrol. All the four NPs showed suitable sustained releases of miRNA and drugs, in fact they remained stable enough not experiencing an immediate burst release but releasing half of the amount gradually within around 3 days from incubation. Manufactured nanoparticles were tested both on two-dimensional cell models at three different cell densities and on monoculture Osteosarcoma spheroids successfully manufactured for both types of cells. The dimension of the manufactured spheroids was analyzed and it was noticed a common trend for both cell types of spheroids: the cells initially tended to cluster together to form the spheroid, gradually decreasing in

size because of their ability to interact and agglomerate, but then, at about 7 days, it began to grow again as the tumor cells began to proliferate and thus the size of the spheroid increased. Nanoparticles with Doxo and miRNA resulted to have a more pronounced cytotoxic activity with both U2OS cells and SaoS-2 in two-dimensional culture models as expected, due to the synergistic antitumor effects of miRNAs and conventional chemotherapy as Doxo<sup>[127]</sup>. Looking at the effects of the NPs on the spheroids, it cannot be appreciated the different NPs treatments but it was noticed the presence of necrotic core, bigger as the time of incubation increased, suggesting that the amount of dead cells increased. Evaluation of the metabolic activity of cells showed that LbL-NPs are more cytotoxic and interfering with the metabolic activity of both cell types, for both cell models tested: the metabolic fluorescence values were lower than those obtained with the other treatments and these values tended to decrease as incubation time increased. This suggests that nanoparticles with natural nanocoating materials achieved by layer-by-layer technique might be more efficient in carrying miR-34a, Doxo, and Resv internal to the core without excessive dispersion of them out of the target site<sup>[151]</sup>, and would also be able to carry more drugs due to their additional presence in the various layers. In contrast, miRDx and miRDxRs NPs showed similar behavior to each other towards cellular metabolic activity, however lower than those obtained with miR-NPs treatment, which was found to be the less cytotoxic and less interfering as treatment. This study also produced a viable and effective pectin extraction process that could be used on an industrial scale, helping to overcome food waste that is one of the biggest worldwide problems. In particular, the cheap and renewable resource from which we extracted pectin was cocoa biowaste which turned out to be an excellent source of pectin for our purposes. These experiments confirmed that using ultrasonic assisted extraction at higher temperatures produced higher yields. The best combination of input parameters was a temperature of 70°C, 90 min of time and 50g/ml of ratio, which gave the highest values of extracted analytical determinations: zeta potential value of -58.81mV, GA percentage of 41.8% and 22.6% of yield. The high value of GA confirmed the good quality of the extracted pectin<sup>[126]</sup> and the strong negative charge observed was necessary in order to use this pectin as a polyelectrolyte (polyanion) in the production of a nanocoating through layer-by-layer assembly. It was successfully used in conjunction with a positively charged substance (chitosan) to make a 2-layers coating nanoparticle.

## 7. Future insights

Future modifications and refinements can be considered for next insights and developments of this project. First, manufactured NPs could be further functionalized with surface ligands and proteins in order to specifically deliver them into OS cells without systemic dispersion, optimizing then targeting and internalization of the NPs. Another development could be testing different concentrations of the constituent NPs materials in order to achieve better encapsulation of Resveratrol thereby being able to test its antioxidant and antitumor efficacy by e.g. ROS assay. It could be necessary also to evaluate not only the antioxidant effect of the resveratrol but also of the pectin used as the first layer in the LbL-NPs. Another future insight could be the evaluation of the release of the encapsulated drugs at pHs more similar to physiological and tumor conditions, such as analysis of drugs releases in citrate buffer at pH 5.5, in order to understand how NPs behave in a more biomimetic tumor-site. Concerning the manufactured spheroids, an even more complex and biomimetic model could be obtained by making, for example, multiculture spheroids with different osteosarcoma and ECM cell types. Another important development could be the use of different concentrations of miR-34a, Doxo and Resv encapsulated in the NPs but also different concentration of NPs used to treat 2D cells and spheroids models. Furthermore, to appreciate significant changes in spheroids viability and activity It will be necessary to increase the NPs treating doses. Another insight worth exploring could be the internalization of NPs by flowcytometry and the evaluation of cells gene expression, before and after treatment with NPs, by using qRT-PCR in order to evaluate gene effects contributed by miR-34a.

## 8. References

- [1] Antonio J. Salgado, Olga P. Coutinho, et al. Bone Tissue Engineering: State of the Art and Future Trend. *Macromol. Biosci.* (2004) 4:743–765. doi: 10.1002/mabi.200400026
- [2] J. E. Aubin, F. Liau, “Principles of Bone Biology”, 1<sup>st</sup> edition, Academic, San Diego, CA 1996, p. 51.
- [3] P. Ducey, T. Schinke, G. Karsenty, *Science* (2000), 289, 1501.
- [4] E. J. Mackie, *Int. J. Cell Biochem. & Cell Biol.* (2003), 1301.
- [5] P. J. Nijweide, E. H. Burger, J. K. Nulend, A. Van der Plas, “Principles of Bone Biology”, 1<sup>st</sup> edition, Academic, San Diego, CA 1996, p. 115.
- [6] K. Vaananen, “Principles of Bone Biology”, 1<sup>st</sup> edition, Academic, San Diego, CA 1996, p. 103.
- [7] V. I. Sikavitsas, J. S. Temenoff, A. G. Mikos, *Biomaterials* 2001, 22, 2581.
- [8] J. S. Temenoff, L. Lu, A. G. Mikos, “Bone Engineering”, 1<sup>st</sup> edition, Em squared, Toronto 1999, p. 454.
- [9] Misaghi A, Goldin A, Awad M and Kulidjian A A 2018, *Osteosarcoma: a comprehensive review Sicot J.* 4 12, doi: 10.1051/sicotj/2017028
- [10] Mialou V, Philip T, Kalifa C, Perol D, Gentet J C, Marec-Berard P, Pacquement H, Chastagner P, Defaschelles A S and Hartmann O (2005) *Metastatic osteosarcoma at diagnosis: prognostic factors and long-term outcome.* doi: 10.1002/cncr.21263
- [11] J. Zhang, Y. Yan, C. Wang, S. Zhang, Z. Yu, W. Wang, *MicroRNAs in osteosarcoma.* doi: 10.1016/j.cca.2015.01.025
- [12] Guanyu Zhang, Yiran Li, Jiasheng Xu and Zhenfang Xiong, *Advances in the role of miRNAs in the occurrence and development of osteosarcoma.* doi: 10.1515/med-2020-0205
- [13] F. Pineiro, I. Badiola, A. Sanchez, *Nanocarriers for microRNA delivery in cancer medicine.* doi: 10.1016/j.biotechadv.2017.03.002
- [14] Dawidczyk CM, Russell LM, Searson PC. *Nanomedicines for cancer therapy: state-of-the-art and limitations to pre-clinical studies that hinder future developments.* *Front Chem* 2014;2:69. doi: 10.3389/fchem.2014.00069
- [15] K. Wu, B. Yu, D. Li, Y. Tian, Y. Liu, J. Jiang, *Recent Advances in Nanoplatforms for the Treatment of Osteosarcoma.* doi: 10.3389/fonc.2022.805978
- [16] S. Wang, H. Hu, X. Qing, Z. Zhang, Z. Shao, *Recent advances of drug delivery nanocarriers in osteosarcoma treatment,* doi: 10.7150/jca.36588
- [17] Doppalapudi S, Jain A, Domb AJ, Khan W. *Biodegradable polymers for targeted delivery of anti-cancer drugs.* *Expert Opin Drug Deliv.* 2016; 13: 891-909, doi: 10.1517/17425247.2016.1156671
- [18] Huang P et al. *Nano-, micro-, and macroscale drug delivery systems for cancer immunotherapy.* (2019) doi: 10.1016/j.actbio.2018.12.028
- [19] S Ram Prasad<sup>1</sup>, T S Sampath Kumar, A. Jayakrishnan, *Nanocarrier-based drug delivery systems for bone cancer therapy: a review.* doi:10.1088/1748-605X/abf7d5
- [20] Calzoni E, Cesaretti A, Polchi A, Di Michele A, Tancini B, Emiliani C. *Biocompatible Polymer Nanoparticles for Drug Delivery Applications in Cancer and Neurodegenerative Disorder Therapies.* *J Funct Biomater* 2019; 10, doi: 10.3390/jfb10010004
- [21] Suksiriworapong J, Taresco V, Ivanov DP, Styliari ID, Sakchaisri K, Junyaprasert VB, et al. *Synthesis and properties of a biodegradable polymer-drug conjugate: Methotrexate-poly(glycerol adipate).* *Colloids Surf B Biointerfaces* 2018; 167: 115-25, doi: 10.1016/j.colsurfb.2018.03.048
- [22] Das M, Mohant C and Sahoo S K 2009 *Ligand-based targeted therapy for cancer tissue.* *Opin. Drug Deliv.* 6 285–304, doi: 10.1517/17425240902780166
- [23] Misra R, Acharya S and Sahoo S K 2010 *Cancer nanotechnology: application of nanotechnology in cancer therapy* *Drug Discov. Today* 15 842–50,
- [24] Li Y, Lim S and Ooi C P 2012 *Fabrication of cisplatin-loaded poly (lactide-co-glycolide) composite microspheres for osteosarcoma treatment.* *Pharm. Res.* 29 756–69, doi: 10.1007/s11095-011-0600-9
- [25] Tan M L, Dunstan D E, Friedhuber A M, Choong P F and Dass C R 2010 *A nanoparticulate system that enhances the efficacy of the tumoricide D<sub>2</sub>13 when administered proximal to the lesion site.* *J. Control. Release* 144 196–202.
- [26] Azarmi S, Huang Y, Chen H, McQuarrie S, Abrams D, Roa W, Finlay W H, Miller G G and Lobenberg R 2006 *Optimization of a two-step desolvation method for preparing gelatin nanoparticles and cell uptake studies in 143B osteosarcoma cancer cells.* *J. Pharm.* 9 124–32,
- [27] Salerno M et al 2010 *Bone-targeted doxorubicin-loaded nanoparticles as a tool for the treatment of skeletal metastases.* *Curr. Cancer Drug Targets* 10 649–59, doi: 10.2174/156800910793605767
- [28] Li S, Xiong Y and Zhang X 2017 *Poloxamer surface modified trimethyl chitosan nanoparticles for the effective delivery of methotrexate in osteosarcoma.* *Biomed. Pharmacother.* 90 872–9, doi: 10.1016/j.biopha.2017.04.004
- [29] Sun K, Wang J, Zhang J, Hua M, Liu C and Chen T 2011 *Dextran-g-PEI nanoparticles as a carrier for co-delivery of adriamycin and plasmid into osteosarcoma cells.* *Int. J. Biol. Macromol.* 49 173–80, doi: 10.1016/j.ijbiomac.2011.04.007
- [30] Liu Y F, Liu R, Li X Y, Song Z and Zhao X H 2016 *Development of docetaxel and alendronate-loaded chitosan-conjugated poly(lactide-co-glycolide) nanoparticles: in vitro characterization in osteosarcoma cells.* *Trop. J. Pharm. Res.* 15 1353–60, doi: 10.4314/tjpr.v15i7.1
- [31] Gurny R et al. *Drug Development and Industrial Pharmacy.* 1981;7(1):1-25. doi: 10.3109/03639048109055684
- [32] S.W.L. Lee et al., *MicroRNA delivery through nanoparticles.* *Journal of Controlled Release* 313, 80-95, 2019, doi: 10.1016/j.jconrel.2019.10.007

- [33] J.S. Suk et al., PEGylation as a strategy for improving nanoparticle-based drug and gene delivery. *Advanced Drug Delivery Reviews* 99A, 28-51, 2016, doi: 10.1016/j.addr.2015.09.012
- [34] M. Mir et al., Recent applications of PLGA based nanostructures in drug delivery. *Colloids and Surfaces B: Biointerfaces* 159, 217-231, 2017, doi: 10.1016/j.colsurfb.2017.07.038
- [35] S. Malik et al., Next generation miRNA inhibition using short anti-seed PNAs encapsulated in PLGA nanoparticles. *Journal of Controlled Release* 327, 406-419, 2020, doi:10.1016/j.jconrel.2020.08.026
- [36] Shafabakhsh R, Yousefi B, Asemi Z, Nikfar B, Mansournia MA, Hallajzadeh J. Chitosan: A Compound for Drug Delivery System in Gastric Cancer-A Review. *Carbohydr Polym* (2020) 242:116403. doi: 10.1016/j.carbpol.2020.116403,
- [37] F. Tekie et al., Chitosan polyplex nanoparticle vector for miR-145 expression in MCF-7: Optimization by design of experiment. *International Journal of Biological Macromolecules* 81, 828-837, 2015, doi: 10.1016/j.ijbiomac.2015.09.014
- [38] Parhi P, Mohanty C and Sahoo S K 2012 Nanotechnology-based combinational drug delivery: an emerging approach for cancer therapy. *Drug Discovery Today* 17 1044–52, doi: 10.1016/j.drudis.2012.05.010,
- [39] Kemp J A, Shim M S, Heo C Y and Kwon Y J 2016 Combo nanomedicine: co-delivery of multi-modal therapeutics for efficient, targeted, and safe cancer therapy. *Adv. Drug Deliv. Rev.* 98 3–18, doi: 10.1016/j.addr.2015.10.019
- [40] Morton S W, Lee M J, Deng Z J, Dreaden E C, Siouev E, Shopsowitz K E, Shah N J, Yaffe M B and Hammond P T 2014 A nanoparticle-based combination chemotherapy delivery system for enhanced tumor killing by dynamic rewiring of signaling pathways. *Sci. Signal* 13, doi: 10.1126/scisignal.2005261
- [41] Shafei, A., El-Bakly, W., Sobhy, A., Wagdy, O., Reda, A., Aboelenin, O., et al. (2017). A review on the efficacy and toxicity of different doxorubicin nanoparticles for targeted therapy in metastatic breast cancer. *Biomed. Pharmacother.* 95, 1209–1218. doi: 10.1016/j.biopha.2017.09.059
- [42] Mattu, C., Brachi, G., Menichetti, L., Flori, A., Armanetti, P., Ranzato, E., et al. (2018). Alternating block copolymer-based nanoparticles as tools to modulate the loading of multiple chemotherapeutics and imaging probes. *Acta Biomater.* 80, 341–351. doi: 10.1016/j.actbio.2018.09.021
- [43] Kozhukharova, I., Zemelko, V., Kovaleva, Z., Alekseenko, L., Lyublinskaya, O., and Nikolsky, N. (2018). Therapeutic doses of doxorubicin induce premature senescence of human mesenchymal stem cells derived from menstrual blood, bone marrow and adipose tissue. *Int. J. Hematol.* 107, 286–296. doi: 10.1007/s12185-017-2346-6
- [44] Yu, D., Zhang, S., Feng, A., Xu, D., Zhu, Q., Mao, Y., et al. (2019). Methotrexate, doxorubicin, and cisplatin regimen is still the preferred option for osteosarcoma chemotherapy: a meta-analysis and clinical observation. *Medicine* 98:e15582. doi: 10.1097/md.00000000000015582
- [45] Baek, N., Seo, O. W., Kim, M., and Hulme, J. (2016). An SSA. Monitoring the effects of doxorubicin on 3D-spheroid tumor cells in real-time. *Onco Targets Ther.* 9:7207. doi: 10.2147/ott.s112566
- [46] Buondonno, I., Gazzano, E., Tavanti, E., Chegaev, K., Kopecka, J., Fanelli, M., et al. (2019). Endoplasmic reticulum-targeting doxorubicin: a new tool effective against doxorubicin-resistant osteosarcoma. *Cell Mol. Life Sci.* 76, 609–625. doi: 10.1007/s00018-018-2967-9
- [47] Prados, J., Melguizo, C., Ortiz, R., Velez, C., Alvarez, P. J., Arias, L. J., et al. (2012). Doxorubicin-loaded nanoparticles: new advances in breast cancer therapy. *Anti Cancer Agents Med. Chem.* 12, 1058–1070. doi: 10.2174/187152012803529646
- [48] Krishnamurthy, P., Brown, M., Agrawal, S., and Short, R. F. (2017). Acute pancreatitis as a complication of trans-arterial chemoembolization of hepatocellular cancer—case report and review of literature. *J. Gastrointest. Oncol.* 8:E26, <https://doi.org/10.21037/jgo.2017.01.15>
- [49] Tian H, Yu Z. Resveratrol induces apoptosis of leukemia cell line K562 by modulation of sphingosine kinase-1 pathway. *Int J Clin Exp Pathol.* 2015; 8(3):2755–62. PMID: 26045781
- [50] Taniguchi T, Iizumi Y, Watanabe M, Masuda M, Morita M, Aono Y, et al. Resveratrol directly targets DDX5 resulting in suppression of the mTORC1 pathway in prostate cancer. *Cell Death Dis.* 2016; 7:e2211. doi: 10.1038/cddis.2016.114 PMID: 27148684
- [51] Mitrut P, Burada F, Enescu A, Scorei R, Badea D, Genunche-Dumitrescu A, et al. The genotoxicity study of resveratrol in primary gastric adenocarcinoma cell cultures. *Rom J Morphol Embryo.* 2009; 50(3):429–33. PMID: 19690770
- [52] Frojdo S, Cozzone D, Vidal H, Pirola L. Resveratrol is a class IA phosphoinositide 3-kinase inhibitor. *Biochem J.* 2007; 406:511–8. doi: 10.1042/BJ20070236 PMID: 17550345
- [53] ihua Peng, Dianming Jiang, Resveratrol eliminates cancer stem cells of osteosarcoma by STAT3 pathway inhibition. 2018, doi:10.1371/journal.pone.0205918
- [54] Jian Zhang et al., MicroRNAs in osteosarcoma. *Clinica Chimica Acta* 444 (2015) 9–17, doi:10.1016/j.cca.2015.01.025.
- [55] Guanyu Zhang et al., Advances in the role of miRNAs in the occurrence and development of osteosarcoma. *Open Medicine* 2020; 15: 1003–1011, doi:10.1515/med-2020-0205
- [56] Le Chang et al., Review of microRNA in osteosarcoma and chondrosarcoma. *Med Oncol* (2015) 32:172, doi:10.1007/s12032-015-0613-z.
- [57] Valerie B. Sampson et al., MicroRNAs and potential targets in osteosarcoma: review. *Frontiers in Pediatrics* (2015) 3(69), doi:10.3389/fped.2015.00069
- [58] Sayles LC, Breese MR, Koehne AL, Leung SG, Lee AG, Liu HY, et al. Genome-informed targeted therapy for osteosarcoma. *Cancer Discovery.* 2019;9(1):46–63. doi: 10.1158/2159-8290.CD-17-1152.
- [59] Lyra-González I. MicroRNAs dysregulation in hepatocellular carcinoma: insights in genomic medicine. *World J Hepatol.* 2015;7(11):1530–40, doi: 10.4254/wjh.v7.i11.1530,
- [60] Sun Z, Liu Q, Hong H, Zhang H, Zhang T. MiR-19 promotes osteosarcoma progression by targeting SOCS6. *Biochem Biophys Res Commun.* 2018;495(1):1363–9, doi : 10.1016/j.bbrc.2017.10.002

- [61] Bottai G, Pasculli B, Calin GA, et al. Targeting the microRNA-regulating DNA damage/repair pathways in cancer. *Expert Opin Biol Ther* 2014;1–17, doi: 10.1517/14712598.2014.950650
- [62] Adams BD, Kasinski AL, Slack FJ. Aberrant regulation and function of MicroRNAs in cancer. *Curr Biol* 2014;24:R762–76, doi: 10.1016/j.cub.2014.06.043.
- [63] Nugent M. MicroRNA function and dysregulation in bone tumors: the evidence to date. *Cancer Manag Res* 2014;6:15–25, doi: 10.2147%2FCMAR.S53928.
- [64] Miao J, Wu S, Peng Z, et al. MicroRNAs in osteosarcoma: diagnostic and therapeutic aspects. *Tumour Biol* 2013;34:2093–8, doi: 10.1007/s13277-013-0940-7.
- [65] Novello C, Pazzaglia L, Conti A, Quattrini I, Pollino S, Perego P, et al. p53-dependent activation of microRNA-34a in response to etoposide-induced DNA damage in osteosarcoma cell lines not impaired by dominant negative p53 expression. *PLoS One*. 2014;9(12):e114757, doi: 10.1371/journal.pone.0114757
- [66] Ognjanovic S, Olivier M, Bergemann TL, et al. Sarcomas in TP53 germline mutation carriers: a review of the IARC TP53 database. *Cancer* 2012;118:1387–96, doi : 10.1002/cncr.26390
- [67] Osumi T, Miharu M, Fuchimoto Y, et al. The germline TP53 mutation c.722 C N T promotes bone and liver tumorigenesis at a young age. *Pediatr Blood Cancer* 2012;59:1332–3, doi: 10.1093/jnci/djv101.
- [68] Sakurai N, Iwamoto S, Miura Y, et al. Novel p53 splicing site mutation in Li-Fraumeni-like syndrome with osteosarcoma. *Pediatr Int* 2013;55:107–11.
- [69] He L, He X, Lim LP, de Stanchina E, Xuan Z, Liang Y, et al. A microRNA component of the p53 tumour suppressor network. *Nature* (2007) 447(7148):1130–4. doi:10.1038/nature05939
- [70] Raver-Shapira N, Marciano E, Meiri E, Spector Y, Rosenfeld N, Moskovits N, et al. Transcriptional activation of miR-34a contributes to p53-mediated apoptosis. *Mol Cell* (2007) 26(5):731–43. doi:10.1016/j.molcel.2007.05.017
- [71] He C, Xiong J, Xu X, Lu W, Liu L, Xiao D, et al. Functional elucidation of MiR-34 in osteosarcoma cells and primary tumor samples. *Biochem Biophys Res Commun* (2009) 388(1):35–40. doi:10.1016/j.bbrc.2009.07.101
- [72] He C, Xiong J, Xu X, et al. Functional elucidation of MiR-34 in osteosarcoma cells and primary tumor samples. *Biochem Biophys Res Commun* 2009;388:35–40, doi: 10.1016/j.bbrc.2009.07.101
- [73] Tian Y, Zhang YZ, Chen W. MicroRNA-199a-3p and microRNA-34a regulate apoptosis in human osteosarcoma cells. *Biosci Rep* 2014;34:281–6, doi: 10.1042%2FBRSR20140084
- [74] Wu X, Zhong D, Gao Q, et al. MicroRNA-34a inhibits human osteosarcoma proliferation by downregulating ether a go-go 1 expression. *Int J Med Sci* 2013;10:676–82, doi: 10.7150/ijms.5528
- [75] He L, et al. A microRNA component of the p53 tumour suppressor network. *Nature*. 2007;447(7148):1130–4, doi:10.1038/nature05939
- [76] Donato Cosco et al., Delivery of miR-34a by chitosan/PLGA nanoplexes for the anticancer treatment of multiple myeloma. *Scientific Reports* volume 5, Article number: 17579 (2015), doi:10.1038/srep17579
- [77] Lu B et al. Chitosan-Modified PLGA Nanoparticles for Control-Released Drug Delivery. *Polymers*. 2019;11(2):304, doi :10.3390/polym11020304
- [78] Shi Y, et al. Surface-modified PLGA nanoparticles with chitosan for oral delivery of tolbutamide. *Colloids and Surfaces B: Biointerfaces*. 2018;161:67-72, doi: 10.1016/j.colsurfb.2017.10.037
- [79] Peng X et al. Box-Behnken design based statistical modeling for the extraction and physiochemical properties of pectin from sunflower heads and the comparison with commercial low-methoxyl pectin. 2020. Available from: <https://doi.org/10.1038/s41598-020-60339-1>
- [80] Guandalini B.B.V et al. Sequential extraction of phenolics and pectin from mango peel assisted by ultrasound. 2019. Available from: <https://doi.org/10.1016/j.foodres.2018.12.011>
- [81] Hastuti B et al. Synthesis and characterization of pectin membrane as a matrix for curcumin sustained-release. 2020. Available from: <http://dx.doi.org/10.1088/1757-899X/833/1/012069>
- [82] Kastarov P et al. Polysaccharide-based Micro and Nanosized drug delivery systems for potential application in the Pediatric Dentistry. 2021. doi:10.3390/polym13193342
- [83] Iriondo-DeHond A et al. Applications of Compounds from Coffee Processing By-Products. 2020. doi:10.3390/biom10091219
- [84] Ezzati S et al. Pectin from sunflower by-product: Optimization of ultrasound assisted extraction, characterization, and functional analysis. 2020. doi :10.1016/j.ijbiomac.2020.09.205
- [85] Vasquez Z.S et al. Biotechnological approaches for coca waste management: A review. 2019. doi:10.1016/j.wasman.2019.04.030
- [86] Maric M et al. An overview of the traditional and innovative approaches for pectin extraction from plant food wastes and by-products: Ultrasound-, microwaves -, and enzyme assisted extraction. 2018. doi:10.1016/j.tifs.2018.03.022
- [87] Huang P et al. Nano-, micro-, and macroscale drug delivery systems for cancer immunotherapy. 2019. doi :10.1016/j.actbio.2018.12.028
- [88] Guzmána E et al. Layer-by-Layer polyelectrolyte assemblies for encapsulation and release of active compounds. 2017. doi:10.1016/j.cis.2017.04.009
- [89] Galia Tiram et al., Identification of Dormancy-Associated MicroRNAs for the Design of Osteosarcoma-Targeted Dendritic Polyglycerol Nanopolyplexes. *ACS Nano*. 2016, 10(2):2028-45. doi: 10.1021/acs.nano.5b06189.
- [90] Javier Munoz-Garcia et al., In vitro three-dimensional cell cultures for bone sarcomas. *J Bone Oncol*. 2021 Jul 6;30:100379. doi: 10.1016/j.jbo.2021.100379

- [91] NamHuk Baek et al., Real-time monitoring of cisplatin cytotoxicity on three-dimensional spheroid tumor cells. *Drug Des Devel Ther.* 2016; 10: 2155–2165. doi: 10.2147/DDDT.S108004
- [92] Holzapfel BM, Hutmacher DW, Nowlan B, Barbier V, Thibaudeau L, Theodoropoulos C, Hooper JD, Loessner D, Clements JA, Russell PJ, Pettit AR, Winkler IG, Levesque JP. Tissue engineered humanized bone supports human hematopoiesis in vivo. *Biomaterials.* 2015;61:103–14.
- [93] Charoen KM, Fallica B, Colson YL, Zaman MH, Grinstaff MW. Embedded multicellular spheroids as a biomimetic 3D cancer model for evaluating drug and drug-device combinations. *Biomaterials.* 2014;35(7):2264–71.
- [94] Hickman JA, Graeser R, de Hoogt R, Vidic S, Brito C, Gutekunst M, van der Kuip H. Three-dimensional models of cancer for pharmacology and cancer cell biology: capturing tumor complexity in vitro/ex vivo. *Biotechnol J.* 2014; 9(9):1115–28.
- [95] Fong ELS, Harrington DA, Farach-Carson MC, Yu H. Heralding a new paradigm in 3D tumor modeling. *Biomaterials.* 2016;108:197–213.
- [96] Salamanna F, Contartese D, Maglio M, Fini M. A systematic review on. In vitro 3D bone metastases models: a new horizon to recapitulate the native clinical scenario. *Oncotarget.* 2016;7(28):44803–20.
- [97] Gorgun C, Ozturk S, Gokalp S, Vatansever S, Gurhan SI, Urkmez AS. Synergistic role of three dimensional niche and hypoxia on conservation of cancer stem cell phenotype. *Int J Biol Macromol.* 2016;90:20–6.
- [98] Ghajar CM, Bissell MJ. Tumor engineering: the other face of tissue engineering. *Tissue Eng A.* 2010;16(7):2153–6.
- [99] Villasante A, Vunjak-Novakovic G. Tissue-engineered models of human tumors for cancer research. *Expert Opin Drug Discov.* 2015;10(3):257–687
- [100] Benien P, Swami A (2014) 3D tumor models: history, advances and future perspectives. *Future Oncol* 10:1311–1327. doi:10.2217/fon.13.274
- [101] Thoma CR, Zimmermann M, Agarkova I et al (2014) 3D cell culture systems modeling tumor growth determinants in cancer target discovery. *Adv Drug Deliv Rev* 69–70:29–41. doi:10.1016/j.addr.2014.03.001
- [102] Vinci M, Gowan S, Boxall F, Patterson L, Zimmermann M, Court W, Lomas C, Mendiola M, Hardisson D, Eccles SA. Advances in establishment and analysis of three-dimensional tumor spheroid-based functional assays for target validation and drug evaluation. *BMC Biol.* 2012;10:29.
- [103] Arai K, Sakamoto R, Kubota D, Kondo T. Proteomic approach toward molecular backgrounds of drug resistance of osteosarcoma cells in spheroid culture system. *Proteomics.* 2013;13(15):2351–60.
- [104] Baek N, Seo OW, Kim M, Hulme J, An SS. Monitoring the effects of doxorubicin on 3D-spheroid tumor cells in real-time. *Onco Targets Ther.* 2016;9:7207–18.
- [105] Gebhard C, Gabriel C, Walter I. Morphological and Immunohistochemical characterization of canine Osteosarcoma spheroid cell cultures. *Anat Histol Embryol.* 2016;45(3):219–30.
- [106] Rimann M, Laternser S, Gvozdenovic A, Muff R, Fuchs B, Kelm JM, Graf-Hausner U. An in vitro osteosarcoma 3D microtissue model for drug development. *J Biotechnol.* 2014;189:129–35.
- [107] Cosco D et al. Delivery of miR-34a by chitosan/PLGA nanoplexes for the anticancer treatment of multiple myeloma *Scientific Reports.* 2015;5(1), doi: 10.1038/srep17579
- [108] Cosco D et al. Physicochemical features and transfection properties of chitosan/poloxamer 188/poly(D,L-lactide-co-glycolide) nanoplexes. *International Journal of Nanomedicine.* 2014; 9: 2359–2372, doi: 10.2147/IJN.S58362
- [109] Dynamic Light Scattering: An Introduction in 30 Minutes [Internet]. Warwick.ac.uk. 2022 [cited 27 April 2022]. Available from: [https://warwick.ac.uk/fac/cross\\_fac/sciencecity/programmes/internal/themes/am2/booking/particlesize](https://warwick.ac.uk/fac/cross_fac/sciencecity/programmes/internal/themes/am2/booking/particlesize)
- [110] Selvamani V. *Characterization and Biology of Nanomaterials for Drug Delivery.* 2019;:425-444
- [111] Lee M et al. *Biomaterials.* 2005;26(14):2147-2156.
- [112] Transmission Electron Microscopy (TEM) [Internet]. Warwick.ac.uk. 2022 [cited 1 May 2022]. Available from: <https://warwick.ac.uk/fac/sci/physics/current/postgraduate/regs/mpagswarwick/ex5/techniques/structural/tem/>
- [113] Absorbance Measurements – the Quick Way to Determine Sample Concentration [Internet]. 2019 [cited 10 May 2022]. <https://handling-solutions.eppendorf.com/sample-handling/photometry/principles/detailview-principles/news/absorbance-measurements-the-quick-way-to-determine-sample-concentration/>
- [114] Top Tip Bio Academy. How To Interpret Nanodrop Results For RNA [Internet]. 2019 [cited 10 May 2022]. Available from: <https://www.youtube.com/watch?v=k7wxYt34A6Y>
- [115] Dranca, F., & Oroian, M. (2019). Ultrasound-assisted extraction of pectin from *Malus domestica* ‘Fälticeni’ apple pomace. *Processes*, 7(8), 488.
- [116] Luo, J., Xu, Y., & Fan, Y. (2019). Upgrading pectin production from apple pomace by acetic acid extraction. *Applied biochemistry and biotechnology*, 187(4), 1300-1311.
- [117] Kacurakova, M., Capek, P., Sasinkova, V., Wellner, N., & Ebringerova, A. (2000). FT-IR study of plant cell wall model compounds: pectic polysaccharides and hemicelluloses. *Carbohydrate polymers*, 43(2), 195-203.
- [118] Dranca, F., Vargha, M., & Oroian, M. (2020). Physicochemical properties of pectin from *Malus domestica* “Fälticeni” apple pomace as affected by non-conventional extraction techniques. *Food Hydrocolloids*, 100, 105383.
- [119] Luo, J., Xu, Y., & Fan, Y. (2019). Upgrading pectin production from apple pomace by acetic acid extraction. *Applied biochemistry and biotechnology*, 187(4), 1300-1311.
- [120] Acikgoz, C. (2011). Extraction and characterization of pectin obtained from quince fruits (*Cydonia vulgaris pers*) grown in Turkey. *Asian Journal of Chemistry*, 23(1), 149.
- [121] Rebecca Marie Dewhurst, Annachiara Scalzone, et al., Development of Natural-Based Bone Cement for a Controlled Doxorubicin-Drug Release. *Front Bioeng Biotechnol.* 2020 Jul 9;8:754. doi: 10.3389/fbioe.2020.00754

- [122] Hsu-Cheng Chiang et al., Edible Polyelectrolyte Complex Nanocoating for Protection of Perishable Produce. *ACS Food Sci. Technol.* 2021, 1, 495–499, doi: 10.1021/acfoodscitech.1c00097
- [123] S Usmani et al., The Formulation of Low Methoxyl Pectin-Based Polyelectrolyte Complexes for Colonic Coating of Probiotic Cells. *IOP Conf. Series: Earth and Environmental Science* 309 (2019) 012045, doi:10.1088/1755-1315/309/1/012045
- [124] Scaffold-based 3D cellular models mimicking the heterogeneity of osteosarcoma stem cell niche Giada Bassi\*, Silvia Panseri, Samuele Maria Dozio, Monica Sandri, *Nature Research* (2020) 10:22294 doi: 10.1038/s41598-020-79448-y
- [125] NamHuk Baek<sup>1</sup>, Ok Won Seo<sup>1</sup> et al. Monitoring the effects of doxorubicin on 3D-spheroid tumor cells in real-time. *OncoTargets and Therapy* 2016;9 7207–7218
- [126] Oliveira et al., Optimization of pectin extraction from banana peels with citric acid by using response surface methodology. *Food Chem.* 2016, 198, 113-118
- [127] Xiongwei Deng et al., Hyaluronic acid-chitosan nanoparticles for co-delivery of MiR-34a and doxorubicin in therapy against triple negative breast cancer. *Biomaterials* 35 (2014) 4333-4344, doi: 10.1016/j.biomaterials.2014.02.006
- [128] Lu B et al. Chitosan-Modified PLGA Nanoparticles for Control-Released Drug Delivery. *Polymers.* 2019;11(2):304, doi: 10.3390/polym11020304
- [129] Ai X et al. *Bioengineering & Translational Medicine.* 2020;6(1).
- [130] Amani A et al. *Iranian Journal of Pharmaceutical Research.* 2019;18.
- [131] Tahmasbi Rad A et al. *ACS Applied Materials & Interfaces.* 2019;11(11):10505-10519.
- [132] Grumezescu A et al. Neuronanomedicine: An Up-to-Date Overview. *Pharmaceutics.* 2019 Mar; 11(3): 101. Published online 2019 Feb 26. doi: 10.3390/pharmaceutics11030101
- [133] Stavits S et al. Nanoparticle Manufacturing – Heterogeneity through Processes to Products. *ACS Applied Nano Materials.* 2018;1(9):4358-4385.
- [134] Danaei M et al. Impact of Particle Size and Polydispersity Index on the Clinical Applications of Lipidic Nanocarrier Systems. *Pharmaceutics.* 2018;10(2):57, doi: 10.3390/pharmaceutics10020057
- [135] Dhakar R et al. Variables Influencing the Drug Entrapment Efficiency of Microspheres: A *Pharmaceutical Review.* 2010 136[142] Song T et al. A review of the role and mechanism of surfactants in the morphology control of metal nanoparticles. *Nanoscale.* 2021;13(7):3895-3910.
- [137] Role of Surfactants in Nanotechnology and Their Applications. *International Journal of Current Microbiology and Applied Sciences.* 2014;3(5):237-260.
- [138] Yan F et al. The effect of poloxamer 188 on nanoparticle morphology, size, cancer cell uptake, and cytotoxicity. *Nanomedicine,* 2010 Feb;6(1):170-8. doi: 10.1016/j.nano.2009.05.004
- [139] Nanoparticle analysis dynamic light scattering DLS [Internet]. Nanoparticleanalyzer.com. 2022 [cited 6 May 2022]. Available from: <https://nanoparticleanalyzer.com/nanoparticle-analysis-comparison-dls>. ph
- [140] Lucy E. Flint et al., Comparison of Osteosarcoma Aggregated Tumour Models with Human Tissue by Multimodal Mass Spectrometry Imaging. *Metabolites.* 2021 Jul 31;11(8):506. doi: 10.3390/metabo11080506
- [141] Ignacio E. León et al. In vitro and in vivo antitumor effects of the VO-chrysin complex on a new three-dimensional osteosarcoma spheroids model and a xenograft tumor in mice. *J Biol Inorg Chem.* 2016 Dec;21(8):1009-1020. doi: 10.1007/s00775-016-1397-0.
- [142] Yonggen Zou et al., miR-34a is downregulated in human osteosarcoma stem-like cells and promotes invasion, tumorigenic ability and self-renewal capacity. *Mol Med Rep.* 2017 Apr;15(4):1631-1637. doi: 10.3892/mmr.2017.6187
- [143] Kang Yan., Jie Gao., Tongtao Yang., Qiong Ma, Xiuchun Qiu, Qingyu Fan, Baoan Ma. MicroRNA-34a Inhibits the Proliferation and Metastasis of Osteosarcoma Cells Both In Vitro and In Vivo. *PLoS One.* 2012;7(3):e33778. doi: 10.1371/journal.pone.0033778
- [144] Xinyu Wu, Daixing Zhong, Quan Gao, Wenliang Zhai, Zhenqi Ding, Jin Wu- MicroRNA-34a Inhibits Human Osteosarcoma Proliferation by Downregulating Ether à go-go 1 Expression. *Int J Med Sci.* 2013;10(6):676-82. doi: 10.7150/ijms.5528
- [145] Angela De Luca, Daniele Bellavia et al., Multiple Effects of Resveratrol on Osteosarcoma Cell Lines. *Pharmaceutics* (Basel). 2022 Mar 11;15(3):342. doi: 10.3390/ph15030342
- [146] Ka Hong Wong et al., Natural Ingredient-Based Polymeric Nanoparticles for Cancer Treatment. *Molecules.* 2020 Aug 9;25(16):3620. doi: 10.3390/molecules25163620
- [147] Shiva Najjary et al., Combination Therapy with miR-34a and Doxorubicin Synergistically Induced Apoptosis in T-Cell Acute Lymphoblastic Leukemia Cell Line. *Med Oncol.* 2021 16;38(12):142. doi: 10.1007/s12032-021-01578-8
- [148] Yong Zhao<sup>1,2</sup>, Mei-Juan Tu et al., Combination therapy with bioengineered miR-34a prodrug and doxorubicin synergistically suppresses osteosarcoma growth. *Biochem Pharmacol.* 2015 15;98(4):602-13. doi: 10.1016/j.bcp.2015.10.015
- [149] Pichaya Thanindrarn et al., Establishment and Characterization of a Recurrent Osteosarcoma Cell Line: OSA 1777. *J Orthop Res.* 2020 Apr;38(4):902-910. doi: 10.1002/jor.24528
- [150] CHRISTOPH PAUTKE et al., Characterization of Osteosarcoma Cell Lines MG-63, SaoS-2 and U-2 OS in Comparison to Human Osteoblasts. *ANTICANCER RESEARCH* 24: 3743-3748 (2004).
- [151] Angela De Luca et al., Relevance of 3d culture systems to study osteosarcoma environment. *Journal of Experimental & Clinical Cancer Research* (2018) 37:2, doi: 10.1186/s13046-017-0663-5
- [152] Seyed Mohammad Taghi Gharibzahedi, Brennan Smith, Ya Guo, Pectin extraction from common fig skin by different methods: The physicochemical, rheological, functional, and structural evaluations. doi: 10.1016/j.ijbiomac.2019.06.040

## 9. Appendix

### 9.1 Full Statistical Results

#### 9.1.1 Galacturonic Acid Pectin

#### Response Surface Regression: GA (%) versus T (C); Time (min); Ratio (g/ml)

##### Coded Coefficients

Term	Coef	SE Coef	T-Value	P-Value	VIF
Constant	38,12	2,21	17,28	0,000	
T (C)	6,89	2,43	2,84	0,018	1,00
Time (min)	1,06	2,43	0,44	0,672	1,00
Ratio (g/ml)	5,81	2,43	2,39	0,038	1,00
T (C)*T (C)	-13,16	3,98	-3,31	0,008	1,01
Time (min)*Time (min)	-6,71	3,98	-1,69	0,123	1,01
Ratio (g/ml)*Ratio (g/ml)	-12,59	3,98	-3,16	0,010	1,01
T (C)*Time (min)	7,50	5,12	1,47	0,173	1,00
T (C)*Ratio (g/ml)	-1,47	5,12	-0,29	0,779	1,00
Time (min)*Ratio (g/ml)	-0,81	5,12	-0,16	0,877	1,00

##### Model Summary

S	R-sq	R-sq(adj)	R-sq(pred)
5,42545	78,89%	59,89%	0,00%

##### Analysis of Variance

Source	DF	Adj SS	Adj MS	F-Value	P-Value
Model	9	1099,87	122,208	4,15	0,018
Linear	3	411,83	137,275	4,66	0,027
T (C)	1	237,48	237,480	8,07	0,018
Time (min)	1	5,59	5,592	0,19	0,672
Ratio (g/ml)	1	168,75	168,754	5,73	0,038
Square	3	621,55	207,183	7,04	0,008
T (C)*T (C)	1	321,65	321,648	10,93	0,008
Time (min)*Time (min)	1	83,64	83,640	2,84	0,123
Ratio (g/ml)*Ratio (g/ml)	1	294,14	294,139	9,99	0,010
2-Way Interaction	3	66,50	22,166	0,75	0,545
T (C)*Time (min)	1	63,32	63,318	2,15	0,173
T (C)*Ratio (g/ml)	1	2,44	2,442	0,08	0,779
Time (min)*Ratio (g/ml)	1	0,74	0,737	0,03	0,877
Error	10	294,36	29,436		
Lack-of-Fit	5	218,87	43,774	2,90	0,134
Pure Error	5	75,48	15,097		
Total	19	1394,23			

##### Regression Equation in Uncoded Units

$$\begin{aligned}
 \text{GA (\%)} = & -245,5 + 5,72 \text{ T (C)} + 0,004 \text{ Time (min)} + 4,55 \text{ Ratio (g/ml)} - 0,0494 \text{ T (C)*T (C)} \\
 & - 0,00497 \text{ Time (min)*Time (min)} - 0,0472 \text{ Ratio (g/ml)*Ratio (g/ml)} \\
 & + 0,01250 \text{ T (C)*Time (min)} - 0,0055 \text{ T (C)*Ratio (g/ml)} \\
 & - 0,00135 \text{ Time (min)*Ratio (g/ml)}
 \end{aligned}$$

##### Fits and Diagnostics for Unusual Observations

Obs	GA (%)	Fit	Resid	Std Resid	
20	24,94	31,85	-6,91	-2,01	R

R Large residual

## 9.1.2 Yield Pectin

### Response Surface Regression: Yield (%) versus T (C); Time (min); Ratio (g/ml)

#### Coded Coefficients

Term	Coef	SE Coef	T-Value	P-Value	VIF
Constant	17,731	0,751	23,60	0,000	
T (C)	1,536	0,826	1,86	0,093	1,00
Time (min)	2,108	0,826	2,55	0,029	1,00
Ratio (g/ml)	-0,542	0,826	-0,66	0,526	1,00
T (C)*T (C)	-3,32	1,36	-2,45	0,034	1,01
Time (min)*Time (min)	-0,06	1,36	-0,04	0,967	1,01
Ratio (g/ml)*Ratio (g/ml)	1,80	1,36	1,32	0,215	1,01
T (C)*Time (min)	1,61	1,74	0,92	0,378	1,00
T (C)*Ratio (g/ml)	4,22	1,74	2,42	0,036	1,00
Time (min)*Ratio (g/ml)	-0,68	1,74	-0,39	0,704	1,00

#### Model Summary

S	R-sq	R-sq(adj)	R-sq(pred)
1,84733	71,84%	46,50%	0,00%

#### Analysis of Variance

Source	DF	Adj SS	Adj MS	F-Value	P-Value
Model	9	87,072	9,6746	2,83	0,060
Linear	3	35,486	11,8287	3,47	0,059
T (C)	1	11,797	11,7973	3,46	0,093
Time (min)	1	22,219	22,2190	6,51	0,029
Ratio (g/ml)	1	1,470	1,4698	0,43	0,526
Square	3	28,167	9,3891	2,75	0,098
T (C)*T (C)	1	20,452	20,4518	5,99	0,034
Time (min)*Time (min)	1	0,006	0,0062	0,00	0,967
Ratio (g/ml)*Ratio (g/ml)	1	5,987	5,9871	1,75	0,215
2-Way Interaction	3	23,418	7,8061	2,29	0,141
T (C)*Time (min)	1	2,903	2,9032	0,85	0,378
T (C)*Ratio (g/ml)	1	19,994	19,9944	5,86	0,036
Time (min)*Ratio (g/ml)	1	0,521	0,5205	0,15	0,704
Error	10	34,126	3,4126		
Lack-of-Fit	5	20,641	4,1283	1,53	0,326
Pure Error	5	13,485	2,6970		
Total	19	121,198			

#### Regression Equation in Uncoded Units

$$\begin{aligned}
 \text{Yield (\%)} = & 21,0 + 0,774 \text{ T (C)} - 0,052 \text{ Time (min)} - 1,444 \text{ Ratio (g/ml)} - 0,01244 \text{ T (C)*T (C)} \\
 & - 0,00004 \text{ Time (min)*Time (min)} + 0,00673 \text{ Ratio (g/ml)*Ratio (g/ml)} \\
 & + 0,00268 \text{ T (C)*Time (min)} + 0,01581 \text{ T (C)*Ratio (g/ml)} \\
 & - 0,00113 \text{ Time (min)*Ratio (g/ml)}
 \end{aligned}$$

### 9.1.3 Zeta potential Pectin

#### Response Surface Regression: Zeta potential (mV) versus T (C); Time (min); Ratio (g/ml)

##### Coded Coefficients

Term	Coef	SE Coef	T-Value	P-Value	VIF
Constant	-50,392	0,506	-99,58	0,000	
T (C)	-1,722	0,556	-3,09	0,011	1,00
Time (min)	1,368	0,556	2,46	0,034	1,00
Ratio (g/ml)	-0,449	0,556	-0,81	0,438	1,00
T (C)*T (C)	0,408	0,913	0,45	0,664	1,01
Time (min)*Time (min)	-0,615	0,913	-0,67	0,516	1,01
Ratio (g/ml)*Ratio (g/ml)	-1,223	0,913	-1,34	0,210	1,01
T (C)*Time (min)	2,38	1,17	2,03	0,070	1,00
T (C)*Ratio (g/ml)	-1,13	1,17	-0,96	0,359	1,00
Time (min)*Ratio (g/ml)	-9,95	1,17	-8,48	0,000	1,00

##### Model Summary

S	R-sq	R-sq(adj)	R-sq(pred)
1,24436	90,54%	82,04%	38,94%

##### Analysis of Variance

Source	DF	Adj SS	Adj MS	F-Value	P-Value
Model	9	148,281	16,476	10,64	0,000
Linear	3	25,196	8,399	5,42	0,018
T (C)	1	14,830	14,830	9,58	0,011
Time (min)	1	9,356	9,356	6,04	0,034
Ratio (g/ml)	1	1,009	1,009	0,65	0,438
Square	3	3,826	1,275	0,82	0,510
T (C)*T (C)	1	0,310	0,310	0,20	0,664
Time (min)*Time (min)	1	0,703	0,703	0,45	0,516
Ratio (g/ml)*Ratio (g/ml)	1	2,777	2,777	1,79	0,210
2-Way Interaction	3	119,259	39,753	25,67	0,000
T (C)*Time (min)	1	6,386	6,386	4,12	0,070
T (C)*Ratio (g/ml)	1	1,429	1,429	0,92	0,359
Time (min)*Ratio (g/ml)	1	111,444	111,444	71,97	0,000
Error	10	15,484	1,548		
Lack-of-Fit	5	11,795	2,359	3,20	0,114
Pure Error	5	3,689	0,738		
Total	19	163,765			

##### Regression Equation in Uncoded Units

$$\begin{aligned} \text{Zeta potential (mV)} = & -88,2 - 0,388 \text{ T (C)} + 0,524 \text{ Time (min)} + 1,713 \text{ Ratio (g/ml)} \\ & + 0,00153 \text{ T (C)*T (C)} - 0,000456 \text{ Time (min)*Time (min)} \\ & - 0,00459 \text{ Ratio (g/ml)*Ratio (g/ml)} + 0,00397 \text{ T (C)*Time (min)} \\ & - 0,00423 \text{ T (C)*Ratio (g/ml)} - 0,01659 \text{ Time (min)*Ratio (g/ml)} \end{aligned}$$

##### Fits and Diagnostics for Unusual Observations

Obs	Zeta potential (mV)	Fit	Resid	Std Resid	
8	-56,100	-54,682	-1,418	-2,01	R

R Large residual

### 9.1.4 Size miR34a-NPs

#### Response Surface Regression: Size (nm) versus Speed (rpm); Time (s)

##### Coded Coefficients

Term	Coef	SE Coef	T-Value	P-Value	VIF
Constant	221,8	39,5	5,62	0,001	
Speed (rpm)	-59,4	44,3	-1,34	0,222	1,03
Time (s)	-0,8	42,4	-0,02	0,986	1,05
Speed (rpm)*Speed (rpm)	10,9	70,8	0,15	0,882	1,07
Time (s)*Time (s)	131,0	63,7	2,06	0,079	1,05
Speed (rpm)*Time (s)	10,9	94,7	0,12	0,912	1,05

##### Model Summary

S	R-sq	R-sq(adj)	R-sq(pred)
82,7253	47,43%	9,88%	0,00%

##### Analysis of Variance

Source	DF	Adj SS	Adj MS	F-Value	P-Value
Model	5	43220,2	8644,0	1,26	0,375
Linear	2	12293,5	6146,7	0,90	0,450
Speed (rpm)	1	12292,2	12292,2	1,80	0,222
Time (s)	1	2,4	2,4	0,00	0,986
Square	2	29608,0	14804,0	2,16	0,186
Speed (rpm)*Speed (rpm)	1	162,2	162,2	0,02	0,882
Time (s)*Time (s)	1	28985,5	28985,5	4,24	0,079
2-Way Interaction	1	90,7	90,7	0,01	0,912
Speed (rpm)*Time (s)	1	90,7	90,7	0,01	0,912
Error	7	47904,3	6843,5		
Lack-of-Fit	3	38642,5	12880,8	5,56	0,065
Pure Error	4	9261,8	2315,5		
Total	12	91124,5			

##### Regression Equation in Uncoded Units

$$\begin{aligned} \text{Size (nm)} = & 682 - 0,0141 \text{ Speed (rpm)} - 5,32 \text{ Time (s)} \\ & + 0,000000 \text{ Speed (rpm)*Speed (rpm)} \\ & + 0,0325 \text{ Time (s)*Time (s)} + 0,000018 \text{ Speed (rpm)*Time (s)} \end{aligned}$$

##### Fits and Diagnostics for Unusual Observations

Obs	Size (nm)	Fit	Resid	Std Resid	
2	187,1	292,1	-105,0	-2,30	R
4	429,5	323,5	106,0	2,29	R

R Large residual

### 9.1.5 Zeta potencial miR34a-NPs

#### Response Surface Regression: Zeta Potential (mV) versus Speed (rpm); Time (s)

##### Coded Coefficients

Term	Coef	SE Coef	T-Value	P-Value	VIF
Constant	32,47	6,50	4,99	0,002	
Speed (rpm)	6,77	7,31	0,93	0,385	1,03
Time (s)	7,69	6,98	1,10	0,307	1,05
Speed (rpm)*Speed (rpm)	-11,2	11,7	-0,96	0,370	1,07
Time (s)*Time (s)	-6,9	10,5	-0,66	0,529	1,05
Speed (rpm)*Time (s)	-3,5	15,6	-0,22	0,830	1,05

##### Model Summary

S	R-sq	R-sq(adj)	R-sq(pred)
13,6307	33,49%	0,00%	0,00%

##### Analysis of Variance

Source	DF	Adj SS	Adj MS	F-Value	P-Value
Model	5	654,94	130,987	0,71	0,638
Linear	2	383,79	191,897	1,03	0,405
Speed (rpm)	1	159,57	159,574	0,86	0,385
Time (s)	1	225,53	225,531	1,21	0,307
Square	2	210,42	105,211	0,57	0,592
Speed (rpm)*Speed (rpm)	1	170,26	170,260	0,92	0,370
Time (s)*Time (s)	1	81,50	81,495	0,44	0,529
2-Way Interaction	1	9,18	9,184	0,05	0,830
Speed (rpm)*Time (s)	1	9,18	9,184	0,05	0,830
Error	7	1300,57	185,796		
Lack-of-Fit	3	1019,51	339,838	4,84	0,081
Pure Error	4	281,06	70,265		
Total	12	1955,51			

##### Regression Equation in Uncoded Units

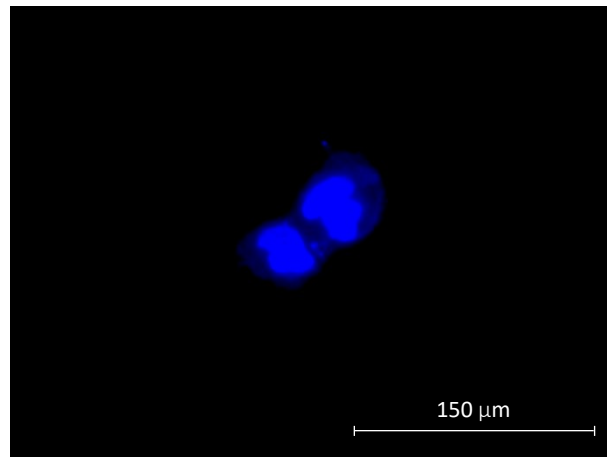
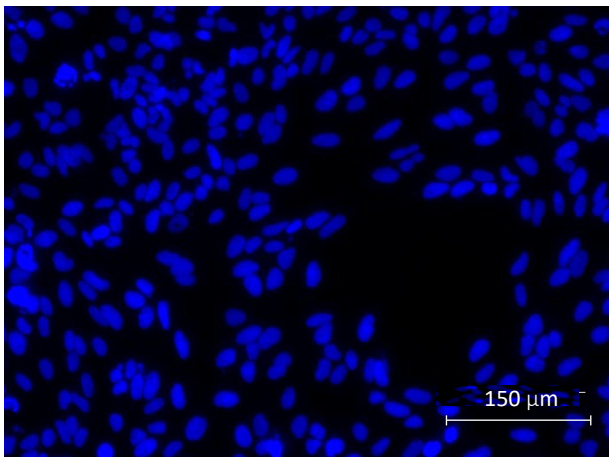
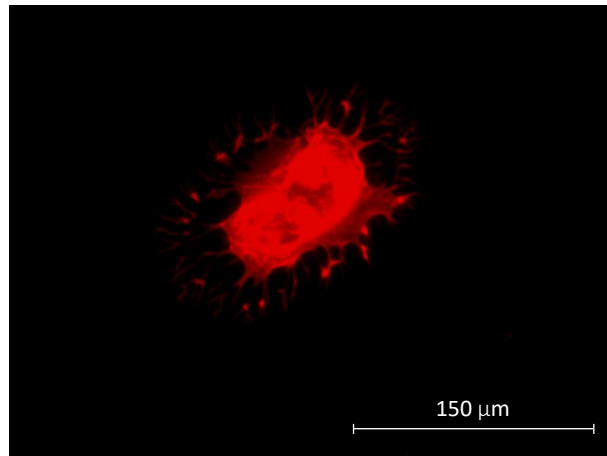
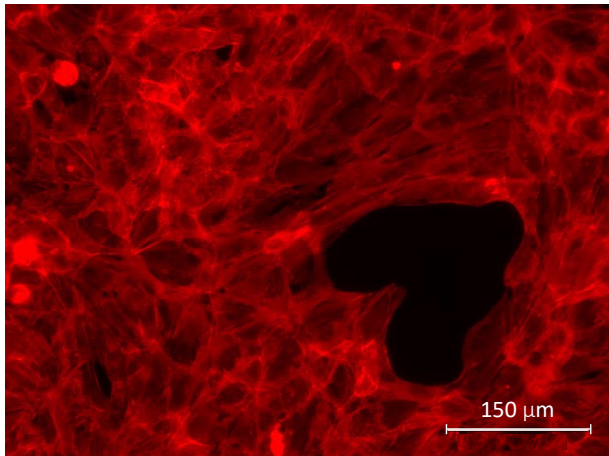
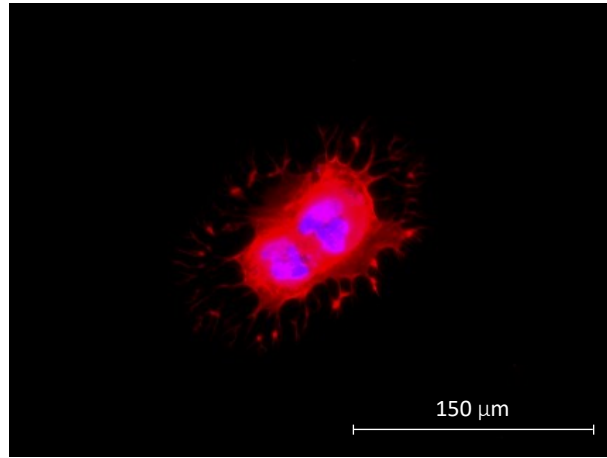
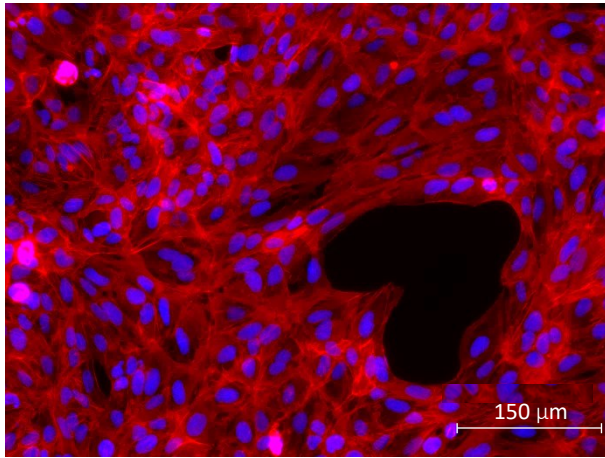
Zeta Potential (mV) = -99 + 0,00767 Speed (rpm) + 0,527 Time (s) - 0,000000 Speed (rpm)\*Speed (rpm) - 0,00172 Time (s)\*Time (s) - 0,000006 Speed (rpm)\*Time (s)

##### Fits and Diagnostics for Unusual Observations

Obs	Zeta Potential (mV)	Fit	Resid	Std Resid	R
8	42,90	28,10	14,80	2,19	R
11	12,60	32,96	-20,36	-2,07	R

R Large residual

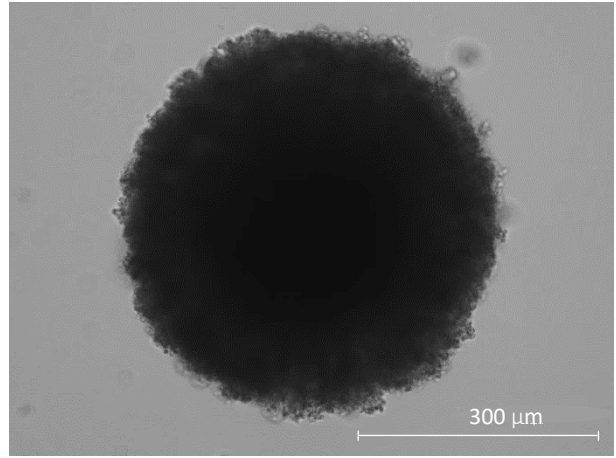
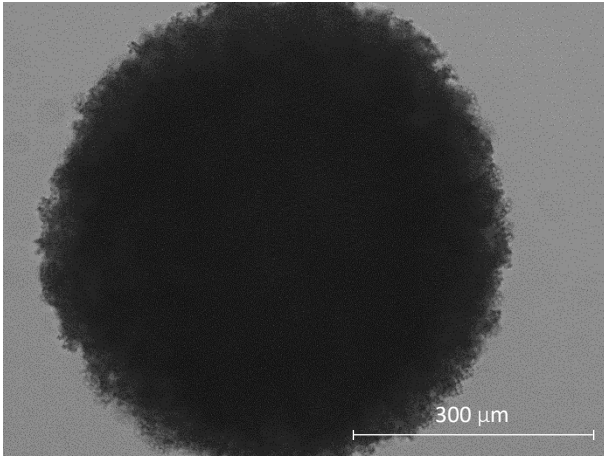
## 9.2 Supplementary Images



Non-treated U2OS cells showing a peculiar heart shape at 7days of culture. There are shown cytoskeletons in red and nucleus in blue.

Two U2OS cells interacting each other. It is shown the interaction between the two nucleus (blue) and cytoskeletons (red).

U2OS Sarcospheres



SaoS-2 Sarcospheres

